# Synthesis and characterization of functional monodispersed cobalt ferrite nanoparticles

Zakaria Mahhouti

# Thèse de Doctorat

***Mention : Physique***
***Spécialité : Physique de la matière condensée***

Présentée à ***l'Ecole Doctorale en Sciences Technologie et Santé (ED 585)*** **de**
**l'Université de Picardie Jules Verne**
***et***
***au Centre d'Etudes Doctorales en Sciences et Technologies de Rabat (CeDoC)***
**de l'Université Mohammed V de Rabat**

par


# Zakaria MAHHOUTI


Pour obtenir le grade de Docteur de l'Université de Picardie Jules Verne et de l'Université Mohammed V

## *Synthesis and Characterization of Functional Monodispersed Cobalt Ferrite Nanoparticles*

**Soutenue le 19/12/2019, après avis des rapporteurs, devant le jury d'examen :**

| | |
|---|---|
| **M. Abelilah BENYOUSSEF,** Professeur, Directeur du Centre Matériaux-Nanomatériaux, Fondation MAScIR, Membre résident de l'Académie Hassan II des Sciences et Techniques | **Président / Examinateur** |
| **M. El Kébir HLIL,** Professeur, Université Joseph-Fourier & Institut Néel | **Rapporteur** |
| **M. Daoud MEZZANE,** Professeur, Université Cadi Ayyad | **Rapporteur** |
| **M. Mimoun EL MARSSI,** Professeur, Université de Picardie Jules Verne | **Directeur de thèse** |
| **M. Abdallah EL KENZ,** Professeur, Université Mohammed V | **Directeur de thèse** |
| **M. Abdelilah LAHMAR,** Ingénieur de Recherches HDR, Université de Picardie Jules Verne | **Co-encadrant** |
| **M. Mohammed HAMEDOUN,** Professeur, Fondation MAScIR | **Invité/ Examinateur** |
| **M. Hassan EL MOUSSAOUI,** Docteur, Chercheur au Centre Matériaux-Nanomatériaux, Fondation MAScIR | **Invité** |

# Preamble

The work presented in this thesis was carried out at the laboratories :

- Laboratory of Condensed Matter Physics at the University of Picardie Jules Vernes.
- Laboratory of Condensed Matter and Interdisciplinary Sciences (LaMCScI) at the Faculty of Sciences (Mohammed V University).
- Materials and nanomaterials center at Moroccan Foundation for Advanced Science, Innovation and Research (MAScIR).

The financial, scientific and technical support devoted to the realization of this thesis was provided by :

- Ministry of Higher Education, Scientific Research, and Professional Training (Enssup) (Morocco) and the National Center for Scientific and Technological Research (CNRST) through the grant Number: PPR15.
- European H2020-MC-RISE-ENIGMA action (N°778072).
- MAScIR Foundation.

# Acknowledgments

This work was done in the framework of a co-supervision of a doctoral (Ph.D.) thesis under the supervision of the following professors :

- Mimoun EL MARSSI, Laboratory of Condensed Matter Physics at the University of Picardie Jules Vernes.
- Abdallah EL KENZ, Laboratory of Condensed Matter and Interdisciplinary Sciences (LaMCScI) at the Faculty of Sciences, Mohammed V University.
- Abdelilah LAHMAR, Laboratory of Condensed Matter Physics at the University of Picardie Jules Vernes.
- Abdelilah BENYOUSSEF, Materials and Nanomaterials Center at Moroccan Foundation for Advanced Science, Innovation and Research (MAScIR Foundation).
- Mohammed HAMEDOUN, Materials and Nanomaterials Center at Moroccan Foundation for Advanced Science, Innovation and Research (MAScIR Foundation).

I would first like to thank my supervisor Mr. **Abdallah EL KENZ**, Professor at the Faculty of Sciences, Mohammed V University, who accepted me to his laboratory and directed my research. I thank him very much for his advice, his availability and above all his personal qualities which favored the conditions and the quality of the work.

My deepest thanks go to my supervisor Mr. **Mimoun EL MARSSI**, Professor at UFR of Sciences and Director of the Laboratory of Condensed Matter Physics at the University of Picardie Jules Vernes, for welcoming me to the laboratory. I express my deep gratitude for his availability, his advice, and his great scientific culture of which he was kind enough to share with me during the years of my thesis.

My sincere gratitude goes to my co-supervisor Mr. **Abdelilah BENYOUSSEF**, Director of Materials and Nanomaterials Center at MAScIR Foundation and resident member of the Hassan II Academy of Science and Technology in Rabat, who has been since the beginning of my Master thesis an inspiring mentor and honest scientist. During these years, he has always been on my side helping me to grow by both encouraging and correcting me. I also would like to thank him for his immense guidance, precious help, encouragement, permanent availability, kindness, sympathy, and support. I have learned many things from him both professionally and personally.

I would like to thank my co-supervisor Mr. **Abdelilah LAHMAR**, a Research engineer at the Laboratory of Condensed Matter Physics at the University of Picardie Jules Vernes, for co-supervision of my research work. I thank him for his support and the time he has dedicated to my work. He is exceptional with great human and scientific qualities, I owe a lot to him for improving and finalizing this thesis.

I also warmly thank Mr. **Mohammed HAMEDOUN**, Professor and project manager at the Materials and Nanomaterials Center at the MAScIR Foundation for his support. This work could not have been accomplished without his respective contributions, the fantastic discussions we had, and his sense of humor. I express my deepest gratitude to him for his kindness, his attentive listening, his efficiency and his availability along this work.

My thanks also go to Mr. **Hassan EL MOUSSAOUI**, Postdoctoral Researcher and project manager at Materials and Nanomaterials Center at Mascir Foundation for giving me the benefit of his experience, I thank him for the valuable help that he has given me throughout these years of my thesis. Being able to benefit from his knowledge was a real chance for me. He was able to make himself available and communicate his enthusiasm when mine was down.

A special thanks goes to Professor **Mohammed ES-SOUNI** and his team from the Institute for Materials & Surface Technology (IMST), Kiel-University, who took care of the preparation of the AAO template used in this work.

I am very grateful to Mr. **El Kébir HLIL**, Professor, CNRS at the University of Joseph of Grenoble and Mr. **Daoud MEZZANE**, Professor at Cadi Ayyad University, for having accepted to be the reviewers of my thesis and for taking time to take a critical look at this manuscript. I also want to thank them for their insightful, valuable comments and suggestions that improved the quality of this work. I would also like to thank Mr. **Abdelilah BENYOUSSEF**, who chaired the jury of the defense.

I would also like to thank all the technical and scientific staff from the three laboratories with whom I had a lot of fun working with on the synthesis and characterization of my samples.

I would like to thank all members and colleagues in LPMC, as well as in MAScIR Foundation.

I present my special thanks to my friends in Morocco, France, and USA (Young G) who constantly help me not only in research but also in many aspects of my life during my Ph.D. study, though I can't list all of their names.

Last but not least, I want to thank my family who constantly supports my every pursuit, especially my mother and my sister. They support me in everything I do and have made me who I am. Without them I am nothing. Unfortunately, my father died a few years ago, and one of his dreams was to see me graduate. He was so proud of me and I'm grateful to his encouragement and his prayers. This thesis is dedicated to him.

# Table of Contents

# List of Tables

# List of Figures

# Introduction

Nowadays, nanotechnologies have covered a large number of technological fields whose common denominator is the nanometric size of structures. In fact, this is a major topic of research for both basic sciences and applications, relying heavily on the development of nanomaterials. Due to their original properties, nanomaterials allow innovations in various fields. Indeed, there is a wide range of potential uses of nanomaterials in different areas and for various physical, chemical, medical and biological applications. Their development also makes it possible to achieve a significant gain in productivity and to open new perspectives by access to innovative technology.

It should be noted that the high demand for "new technology" has prompted researchers to explore innovative approaches to the development of multifunctional materials. At the nanoscale, the physical properties (optical, electronic, magnetic etc.) of the particles are unique and have a particular interest. They are strongly dependent on quantum effects related to their reduced size. In fact, when the size of the material becomes nanometric sized particles, particular phenomena related to quantum confinement can take place. Recently, differences between the magnetic properties of bulk material and a nanomaterial show that size reduction involves profound changes in magnetic properties. Since nanoparticles have a very high surface area/core atom ratio, surface or interface effects lead to significant changes in average values of anisotropies and magnetic moments. On these effects, intrinsic characteristics such as magnetic transition temperatures (Curie temperature and Neel temperature) may strongly depend on the size and morphology of the nanoparticles. Thus, by controlling the size, shape, composition, and structure of the nanoparticles, we manage to control the magnetic characteristics of the material which is the main interest for many applications.

In this work, we are interested in nanomaterials based on spinel ferrites. They already have many fields of application, because of their original magnetic properties, their low cost of synthesis, compared to better known magnetic materials based on precious metals. The most common applications are magnetic recording media, spintronics, magnetically controlled drug delivery, sensors, and hyperthermia.

Magnetic nanoparticles with spinel structure $MFe_2O_4$ (M = Fe, Co, Mn, Zn, Ni ...) have been widely studied for their varied applications ranging from information storage to biomedical applications. Among these applications, some most recent ones based on the magnetic properties of nanoparticles are in full expansion, such as magnetic recording media or

hyperthermia, that require magnetic nanoparticles with controlled size and morphology as well as chemical composition.

In order to synthesize cobalt ferrite nanoparticles, several methods have been developed including microemulsion, sol-gel, microwave, and co-precipitation methods, but the thermal decomposition of metal complexes in the presence of ligand (as a capping agent) appears currently to be the most promising to ensure the control of nanoparticles size, shape, and composition. In addition, nanoparticles synthesized by this method are coated by an organic layer of ligands, which ensure their good colloidal stability in organic solvents. When I arrived at the MAScIR Foundation, this process was not developed yet in the laboratory, and it was, therefore, necessary first to appropriate such method and then develop a tailored synthesis protocol.

Nevertheless, the problem of developing high-quality magnetic nanoparticles is a real challenge. The literature survey showed that this type of material with both homogeneity in size and dispersion are rarely reported. In addition, there are several problems of reproducibility, especially when it comes to synthesis made by thermal decomposition of organometallic precursors in organic solvents. Regarding methods for the preparation of nanorods, they often have limitations. We chose to use an original method of synthesis of magnetic nanorods (one-dimensional). It makes it possible to produce a large number of nanorods without the problem of aggregation often encountered in other synthetic techniques.

The advanced study of the nanoparticles by the usual characterization techniques (XRD, EDS, Raman Spectroscopy, STEM, TGA, FT-IR ...) permitted to collect all the information needed to understand their physical properties as well as the organic layer surrounding them. We emphasis herein another advanced study takes place to study the influence of synthetic conditions, the influence of the organic layer, and the influence of size on the physical properties of the elaborated nanoparticles.

Another interesting approach is to use nanoporous organized materials to synthesize a regular network of nanorods. For many years now, nanoporous alumina membranes have taken great interest in the synthesis of nano-objects. These membranes have very vertical pores naturally and self-organized in a hexagonal network.

In this thesis, 1-3–type nanorods composites are chosen to be the connectivity scheme. Several methods and approaches have been proposed and discussed initially to make this kind of

nanocomposites. We have developed a new approach to transfer $CoFe_2O_4$ nanoparticles to nanorods by using the AAO template.

The main method (or idea) is to incorporate and solidify spherical magnetic particles of $CoFe_2O_4$ with size less than 20 nm in a synthesized porous alumina membrane. In such configuration, all the magnetic particles are oriented according to an external magnetic field and keep in this orientation even without a magnetic field after solidification of the matrix. The procedure consists of three preliminary steps. Firstly, mixing well-dispersed $CoFe_2O_4$ nanoparticles in a solvent (Hexane), allowing a change from the liquid state ($CoFe_2O_4$ nanoparticles surrounded by organic layer and dispersed in Hexane) to the solid state (Only $CoFe_2O_4$ Nanoparticles). Secondly, incorporation of $CoFe_2O_4$ nanoparticles into pores of the alumina membrane. Thirdly, a step of a heat treatment compatible with the magnetic nanoparticles is necessary in order to evaporate all the organic compounds. The insertion of nanoparticles has been done with the help of an external magnetic field.

This thesis is divided into five chapters. Firstly, ferrites nanoparticles and their crystal structure will be presented, as well as their magnetic properties. In the second chapter, a various synthesis method of ferrite nanoparticles will be discussed. The third chapter will present the characterization techniques that we have used to characterize the synthesized ferrite nanoparticles. Chapter four will be dedicated to the experimental details of the thermal decomposition method as well as the chemical and physical characterizations of the obtained $CoFe_2O_4$ nanoparticles. In chapter five, the elaboration of alumina membranes, characterization of AAO template, and the insertion of cobalt ferrite nanoparticles into alumina membrane pores will be discussed in details.

# 1 Magnetic nanoparticles

In this chapter, a brief state of knowledge about ferrite nanoparticles will be presented. After a reminder of their structure, the general basics about magnetism will be described.

## 1.1 Ferrites and their magnetic properties

### 1.1.1 Crystal structure of ferrites

Ferrites of general formula $MFe_2O_4$ ($M = Fe, Co, Mn, Ni, Zn \ldots$) crystallize in the spinel structure $AB_2O_4$. This crystal structure is based on a face-centered cubic structure (cfc) of oxygen anions ($O^{2-}$), whose tetrahedral sites Td (denoted A) and octahedrons sites Oh (denoted B) are partially occupied by the metal cations $M^{2+}$ and $Fe^{3+}$ (Figure 1.1). Only half of the octahedral sites and one-eighth of the tetrahedral sites are occupied.

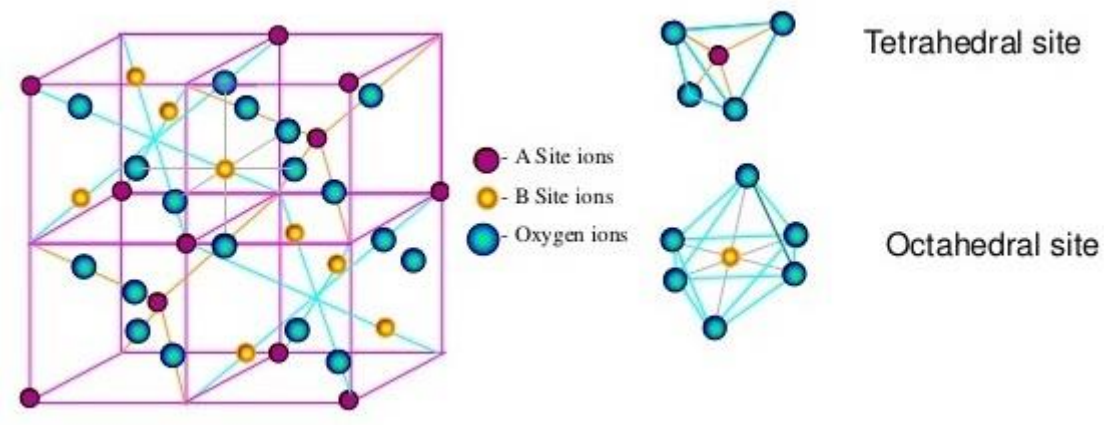


Figure 1. 1: Tetrahedral and octahedral sites in the crystal structure of spinel ferrite.

There are 3 types of spinels:

- Direct spinels: $[M^{2+}]_A[2Fe^{3+}]_BO_4$
- Inverse spinels: $[Fe^{3+}]_A[M^{2+}Fe^{3+}]_BO_4$
- Intermediate spinels: $[M^{2+}_{1-\theta}Fe^{3+}_{\theta}]_A[M^{2+}_{\theta}Fe^{3+}_{2-\theta}]_BO_4$ where $\theta$ represents the inversion rate.

The distribution of ions between A sites and B sites is determined by various parameters such as the ionic radius of the ions, the size of the interstices, the temperature and the stabilization due to the effect of crystalline field. The spinel structure of the bulk material depends on the metal cation $M^{2+}$ considered: most ferrites have inverse spinel structure except zinc ferrite

which crystallizes in direct spinel and manganese ferrite which adopts an intermediate structure (Table 1.1).

| Ferrites | Spinel | Lattice parameter | Density ($g/cm^3$) |
|---|---|---|---|
| $NiFe_2O_4$ | Inverse | 0.834 | 5.38 |
| $CuFe_2O_4$ | Inverse | 0.837 | 5.41 |
| $CoFe_2O_4$ | Inverse | 0.838 | 5.29 |
| $Fe_3O_4$ | Inverse | 0.839 | 5.24 |
| $ZnFe_2O_4$ | Direct | 0.844 | 4.80 |
| $MnFe_2O_4$ | Intermediate ($\theta$=0.2) | 0.850 | 5.00 |

Table 1. 1: Most common ferrites and their characteristics.

### 1.1.2 Magnetic properties of bulk spinel ferrites

In a bulk form of material, atoms behave like little magnets, characterized by their magnetic moment. When a magnetic field $H$ is applied, these elementary magnets orient themselves according to the field. Therefore, the material acquires a magnetization $M = \chi H$ (weak field) where$\chi$ is the magnetic susceptibility.

The magnetic moments can be oriented in different ways according to the magnetic behavior of the material (Table 1.2): diamagnetic, paramagnetic, ferromagnetic, ferrimagnetic or antiferromagnetic [1]. In the case of magnetic materials where the atoms do not interact with their neighbors, this kind of magnetism is called non-cooperative magnetism. Atoms have zero spontaneous macroscopic magnetization. There are two types of non-cooperative magnetism:

- Diamagnetism: atoms do not have a permanent magnetic moment and acquire a weak moment induced in the presence of a field. Their magnetization, induced by the field, is very weak and antiparallel to the applied field. The magnetic susceptibility is negative and it is about of $10^{-5}$, does not depend on the temperature.
- Paramagnetism: the atoms have a permanent magnetic moment, and align themselves parallel to the applied field. The magnetic susceptibility is inversely proportional to temperature $T$ (Curie's Law): $\chi = C/T$, where $C$ is the Curie constant. $\chi$ is positive and it is in the range of $[10^{-4}-10^{-5}]$.

| type | spin alignment | spin in simplified plot | examples |
|---|---|---|---|
| ferromagnetic | all spins align parallel to one another: spontaneous magnetization- $M = a + b$ |  | Fe, Co, Ni, Gd, Dy, $SmCo_5$, $Sm_2Co_{17}$, $Nd_2Fe_{14}B$ |
| ferrimagnetic | most spins parallel to one another, some spins antiparallel: spontaneous magnetization- $M = a - b > 0$ |  | magnetite ($Fe_3O_4$), yttrium iron garnet (YIG), $GdCo_5$ |
| antiferromagnetic | periodic parallel-antiparallel spin distribution: $M = a - b = 0$ | 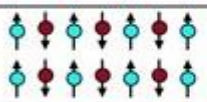 | chromium, FeMn, NiO |
| paramagnetic | spins tend to align parallel to an external magnetic field: $M = 0$ @ $H=0$, $M>0$ @ $H>0$ | 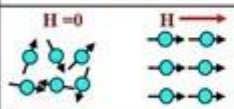  | oxygen, sodium, aluminum, calcium, uranium |
| diamagnetic | spins tend to align antiparallel to an external magnetic field $M = 0$ @ $H=0$, $M<0$ @ $H>0$ | 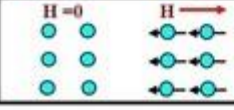  | superconductors, nitrogen, copper, silver, gold, water, organic compounds |

Table 1. 2: Different types of magnetic behavior

In the presence of interactions, the magnetic moments are spontaneously orientated in the absence of an externally applied field. There are three types of cooperative magnetic behaviors:

- Ferromagnetism: the positive exchange interactions favor the parallel alignment of the magnetic moments of neighboring atoms. The susceptibility, instead of becoming infinite at 0 K as in a paramagnetic, it becomes infinite at a characteristic temperature, called Curie temperature $T_C$ (Curie-Weiss Law). Below this temperature, the interactions dominate the thermal agitation and a spontaneous magnetization $M_S$ appears in the absence of applied field.
- Antiferromagnetism: below a critical temperature (Néel $T_N$ temperature) an ordered state of the magnetic moments appears. The moments are aligned antiparallel in two equal and opposite magnetization sub-lattices. Therefore, the total resultant magnetization is null. Above the temperature of Néel, the thermal agitation leads to a susceptibility similar to that of a paramagnetic one.
- Ferrimagnetism: antiferromagnetism in which the carriers of moments are not equivalent. There is no further compensation for the magnetization of the two sub-lattices. Below the Curie temperature $T_C$, a spontaneous magnetization appears. Above this temperature, the magnetic order is broken by the thermal agitation and the material gradually regains a paramagnetic behavior.

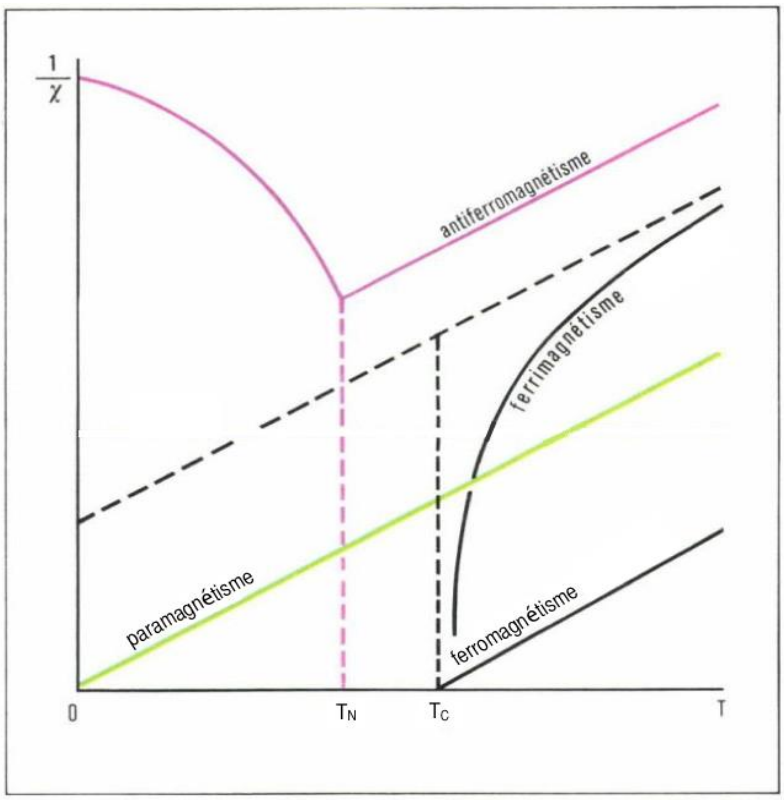


Figure 1. 2: Variation of inverse susceptibility as a function of the temperature for different magnetic behaviors [2].

In the case of a spinel structure, all the exchange interactions between neighboring cations are negative (antiferromagnetic coupling) but the interactions between Td-Oh cations are stronger than the Oh-Oh interactions [2]. If moment carriers are not equivalent, the material is ferrimagnetic.

### 1.1.3 Magnetic domains

In the case of a ferromagnetic material, despite the existence of spontaneous magnetization in the absence of a magnetic field, it does not have a permanent magnetic moment in the macroscopic scale. In fact, at the macroscopic level, the material is divided into several magnetic domains, called Weiss domains, each one has a spontaneous magnetization. From one domain to another, the direction of the moments is different. Therefore, the resulting macroscopic magnetic moment from the sample is null [2]. These domains are separated by the Bloch walls, in which the orientation of the moments passes gradually from a domain to another domain.

Under the action of an external magnetic field, the walls move, leading to a magnification of the domains having the same orientation as the applied field, and progressive disappearance of

the other domains. The variation of the magnetization according to the field is represented in Figure 1.3 (solid line): it is the curve of the first magnetization. Under high magnetic fields (in the order of 50 kOe, depending on the material), the magnetization tends to saturate and reaches a maximum level called saturation magnetization $M_S$. If the field is suppressed, the domains partially get back to their random orientations, and depending on the mobility of the walls, the moments of each domain remain partially aligned with the initial field [2], this gives an appearance of remanent magnetization $M_R$ and a hysteresis loop (Figure 1.3 (dashed lines)). If the temperature increases or a new magnetic field of opposite direction is applied, the remanent magnetization disappears. The coercive field $H_C$ corresponds to the applied field to reach zero magnetization.

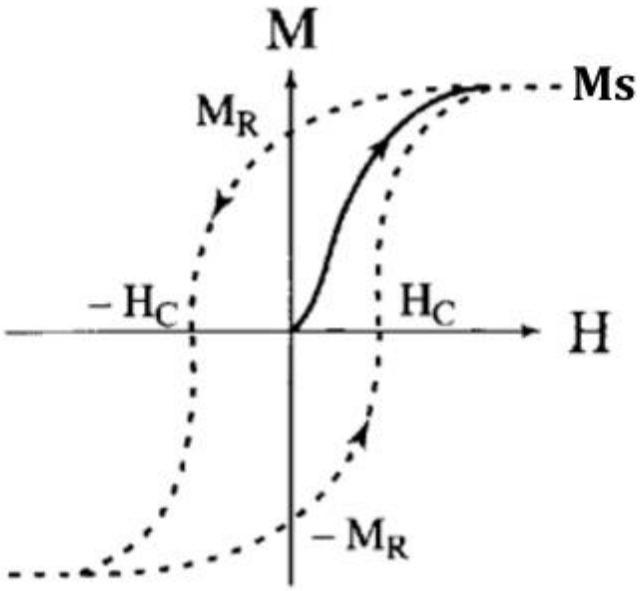


Figure 1. 3: First magnetization curve and hysteresis loop [2].

In a sample with few defects, the Bloch walls move easily so that the magnetization quickly reaches saturation magnetization and also demagnetizes quickly. The hysteresis loop is narrow and this type of material is referred to a soft material. On the contrary, if the sample has many defects which are obstacles to the displacement of the walls, the magnetization increases more slowly depending on the applied field. The hysteresis loop is wide and this type of material is called a hard material.

### 1.1.4 Magnetic anisotropy

In a ferromagnetic material, the magnetic order originates from the exchange energy defined by $J.\overrightarrow{S_A}.\overrightarrow{S_B}$ (with $J$ is the coupling constant and $\overrightarrow{S_A}$, $\overrightarrow{S_B}$ are the neighboring spins), favoring their alignment in the same direction [2]. However, there is another energy, the magnetocrystalline anisotropy energy, which tends to orient the spin direction in a preferred crystalline direction, called the easy axis of magnetization.

If we consider a crystal of cubic symmetry, the magnetocrystalline anisotropy energy $E_{crist}$ is given by the following formula:

$$E_{crist} = K_1(\alpha_1^2\alpha_2^2 + \alpha_2^2\alpha_3^2 + \alpha_3^2\alpha_1^2) + K_2\alpha_1^2\alpha_2^2\alpha_3^2 + \cdots \quad (1.1)$$

Where $K_i$ is the constants of crystalline anisotropy which depend on the type of material and the temperature, $\alpha_{1,2,3}$ are the cosines of the angles that the magnetization does with the three axis of the reference linked to the cube.

The thickness of the Bloch walls depends on the competition between the exchange energy and the magnetocrystalline anisotropy energy and is given by the ratio $\sqrt{J/K}$. When the particle size is smaller or equal to this thickness, a single-domain arrangement of the spins is energetically more favorable. Table 1.3 shows some magnetic properties of bulk materials.

| Ferrites | $T_C$ (K) | $M_S$ (emu/g) at 0 K | $M_S$ (emu/g) at 293 K | K (KJ/m$^3$) |
|---|---|---|---|---|
| $ZnFe_2O_4$ | 713 | - | 0 | 0 |
| $CuFe_2O_4$ | 728 | 29 | 25 | -6 |
| $NiFe_2O_4$ | 858 | 56 | 50 | -6.7 |
| $CoFe_2O_4$ | 793 | 94 | 81 | 220 |
| $Fe_3O_4$ | 858 | 98 | 92 | -11 |
| $MnFe_2O_4$ | 573 | 111 | 80 | -4 |

Table 1. 3: Most common ferrites and their magnetic characteristics of the massive material

## 1.2 Magnetic nanoparticles

In the case of magnetic nanoparticles, the size of particles is small enough that each particle is a magnetic monodomain (there are no Bloch walls as are in the case for multidomain systems). The critical diameter $d_C$ from which the particle can be considered as a magnetic monodomain is defined by [3]:

$$d_C = \frac{36\sqrt{AK_{eff}}}{\mu_0 M_S^2} \quad (1.2)$$

Where $A$ is the exchange constant, $K_{eff}$ is the constant of effective magnetic anisotropy, $\mu_0$ is the vacuum permeability and $M_S$ is the saturation magnetization. $d_C$ is in the order of 10-100 nm.

A monodomain particle carries a permanent magnetic moment, which is the sum of magnetic moments of all atoms that constitute it. An atom corresponds to about 1 $\mu B$, which gives for a nanoparticle between 1000 and 10000 $\mu B$. When structuring in a magnetic monodomain, the reduction of the total number of atoms on the nanometric scale leads to the increase of the contribution of the surface atoms which do not have the same environment as in volume. The surface effects will play on the magnetic properties of the material [4][5][6]. In fact, in addition to volume spins as in the massive material, the nanoparticles have surface spins, thus creating additional interactions.

### 1.2.1 Magnetic anisotropy of nanoparticles

For a monodomain particle, the effective magnetic anisotropy is the resultant of magnetocrystalline anisotropy energies, shape and surface [7].

- Magnetocrystalline anisotropy

For monodomain particles with uniaxial anisotropy, the magnetocrystalline anisotropy energy is written [8]:

$$E_u = K_u V sin^2\theta \quad (1.3)$$

Where $K_u$ represents the constant of uniaxial effective anisotropy, $V$ is the volume of the particle, and $\theta$ is the angle between magnetization and symmetry axis. This expression describes two minimum energies ($\theta = 0\ and\ \pi$) separated by $K_u V$ energy barrier.

- Shape anisotropy

In addition to the magnetocrystalline anisotropy, shape anisotropy can be induced in the case of non-spherical monodomain particles. The discontinuity of the magnetization on the surface of the particles leads to the creation of a demagnetizing field. In the case of an ellipsoidal particle [9] the shape anisotropy energy is:

$$E_f = \frac{1}{2}\mu_0 V(N_x M_x^2 + N_y M_y^2 + N_z M_z^2) \quad (1.4)$$

where $\mu_0$ is the vacuum permeability, $V$ is the volume of particle, $M_{x,y,z}$ are the components of the magnetization and $N_{x,y,z}$ are the demagnetizing field factors related to the x, y, and z axis of the ellipsoid. The demagnetizing field factors verify the equality $N_x + N_y + N_z = 1$. For a spherical monodomain particle, the shape anisotropy energy is null.

- Surface anisotropy

For a monodomain particle, the anisotropy energy also depends on the surface interactions. When the size of the particles decreases, the magnetic surface contributions can become more important than the core of particles themselves [8]. The energy of surface anisotropy will then be dominant compared to the energies of magnetocrystalline anisotropy and shape anisotropy. For a spherical particle of diameter d, the constant of effective magnetic anisotropy $K_{eff}$ follows the following empirical law [10]:

$$K_{eff} = K_v + \frac{S}{V}K_S = K_v + \frac{6}{d}K_S \quad (1.5)$$

Where $K_v$ represents the volume anisotropy constant, $V$ is the volume of the particle, $S$ is the surface of the particle, and $K_S$ is the surface anisotropy constant. The anisotropic energy of a particle $E_a$ is defined by:

$$E_a = K_{eff} V \quad (1.6)$$

The effective anisotropy is therefore sensitive to particle size variation via the second term of equation (1.5).

Nanoparticles are rarely independent, other contributions to the effective anisotropy may be added, such as dipolar interactions between nanoparticles or with the solution dispersion [11]. In the rest of this manuscript, the size of particles being rather small, we will consider that the effective anisotropy is uniaxial. In addition, the particles being dispersed in colloidal solution, they are in the dilute regime and the dipolar interactions are negligible. The constant of anisotropy will be noted $K_\alpha$.

### 1.2.2 Static magnetic properties

The magnetic behavior of nanoparticles depends on the temperature and their anisotropy energy:

- If $K_B T \gg E_\alpha$ particles have superparamagnetic behavior and follow the model of Langevin.
- If $K_B T \ll E_\alpha$ particles are in a blocked state and follow the Stoner Wohlfarth model.

#### 1.2.2.1 Langevin model

If the thermal energy is sufficient to overcome the anisotropy energy ($K_B T > E_\alpha$), the magnetization is not blocked and the particle has a superparamagnetic behavior. In this case and for nanoparticles monodisperse in size, the magnetization curve $M = f(H)$ follows the Langevin model:

$$M = m_S \emptyset \mathcal{L}(\xi) \text{ et } \xi = \frac{\mu_0 \mu H}{K_B T} \tag{1.7}$$

Where $\mathcal{L}(\xi) = cotan(\xi) - \frac{1}{\xi}$ is the Langevin function, $m_S$ is the specific magnetization of the material, $\emptyset$ is the volume fraction, $\mu$ is the magnetic moment of the particle, $\mu_0$ is the vacuum permeability ($\mu_0 = 4\pi 10^{-7}$), $H$ is the applied magnetic field, $K_B$ is the Boltzmann constant and $T$ is the temperature.

Langevin function describes the orientation of the magnetic moments and $\xi$ the ratio between the magnetic energy $\mu_0 \mu H$ and the thermal energy $K_B T$. When the magnetic field increases, the magnetization increases until it reaches a maximum corresponding to $m_S \emptyset$ which called saturation magnetization $M_S$. The magnetization curve as a function of the applied magnetic field is reversible (Figure 1.4).

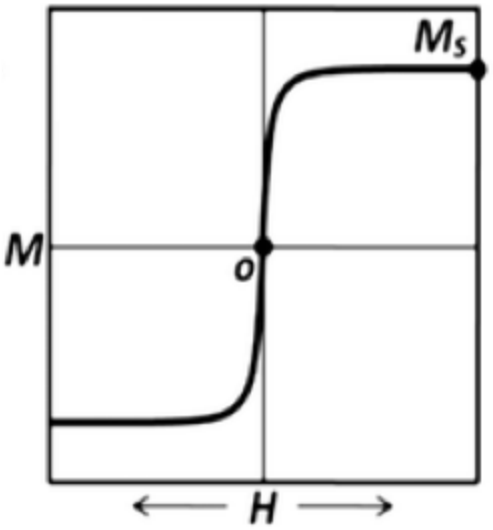


Figure 1. 4: Theoretical magnetization curve of superparamagnetic nanoparticles [3].

The curve of the magnetization as a function of applied magnetic field gives much information. The low-field and high-field approximations of the Langevin model allow estimating the value of the magnetic moment of the particles, as well as their magnetic size.

At low field $\xi \approx 0$et$\mathcal{L} = \xi/3$ which gives in Langevin model:

$$M = m_s \emptyset \frac{\mu_0 \mu H}{3K_B T} = \chi H \tag{1.8}$$

Where $\chi$ is the magnetic susceptibility. Noting that from $\chi$, we can estimate the magnetic moment of particles at low field.

$$\mu = \frac{3K_B T}{m_s \emptyset \mu_0} \tag{1.9}$$

On the other hand, at high field$\xi \gg 1$et$\mathcal{L} = 1 - 1/\xi$ which gives in Langevin model:

$$M = m_s \emptyset - m_s \emptyset \frac{3K_B T}{\mu_0 \mu H} \tag{1.10}$$

Whether $M = a - \frac{b}{H}$

The magnetic moment at high field is:

$$\mu = \frac{m_s \emptyset K_B T}{\mu_0 b} \tag{1.11}$$

In both cases, the magnetic size of the particles is given by:

$$\mu = m_S V_P \tag{1.12}$$

Where $V_P$ is particle volume, we can estimate the size at low field and high field. The magnetic diameter of the nanoparticles is given by:

$$d = \sqrt[3]{\frac{6\mu}{m_S \pi}} \tag{1.13}$$

If the samples are monodisperse, these two sizes will be identical, but in reality, they are not, and the two diameters do not coincide. At the low field, we see the large nanoparticles which couple better to the field, whereas at the high field the large particles are already oriented, and we see mainly the orientation of the small ones. A finer analysis assuming a lognormal distribution $P(d)$ which allows to adjust the data for a Langevin law and estimate the characteristic parameters $d_0$ and $\sigma$ of the distribution:

$$P(d) = \frac{1}{d\sigma\sqrt{2\pi}} \exp\left(-\frac{ln^2\left(\frac{d}{d_0}\right)}{2\sigma^2}\right) \tag{1.14}$$

Where $\sigma$ the polydispersity of the sample and $\ln(d_0)$ is the average value of $\ln(d)$ [12].

#### 1.2.2.2 Stoner-Wohlfarth model

If the thermal energy is not enough to overcome the anisotropy energy ($K_B T \ll E_\alpha$), the nanoparticles are in the blocked state (Figure 1.5). The magnetization then depends on the history of the material and shows a hysteresis loop as a function of the applied field. The system is then characterized by remanent magnetization not null $M_R$ at zero applied field, and a non-zero coercive field $H_C$, which is the necessary applied field to cancel the magnetization.

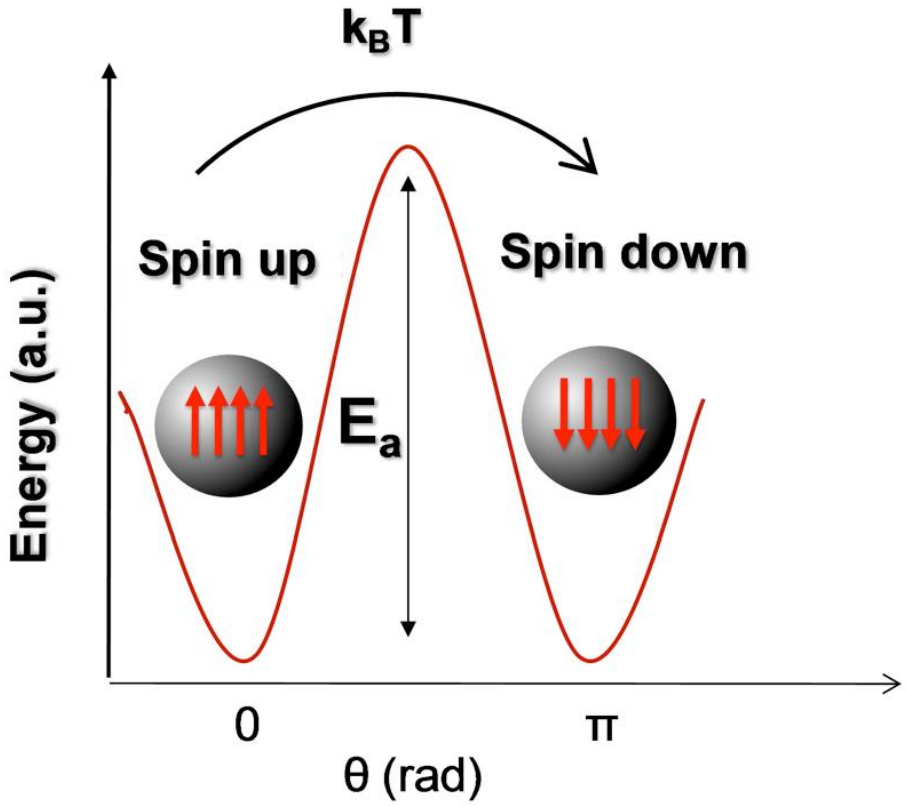


Figure 1. 5: Representation of the energy barrier (or activation energy) $E_\alpha$ that the nanoparticle needs to pass from a spin "up" to a spin "down" [13].

At 0 K, there is no thermal energy and the energy of the system becomes the sum of two different and competitive terms:

- Anisotropy energy $E_\alpha = K_\alpha sin^2\theta$ which tends to align the moment along the easy axis of magnetization
- Zeeman energy $E_z = \mu_0 M_S H cos(\phi - \theta)$ which tends to align the moment according to the applied magnetic field

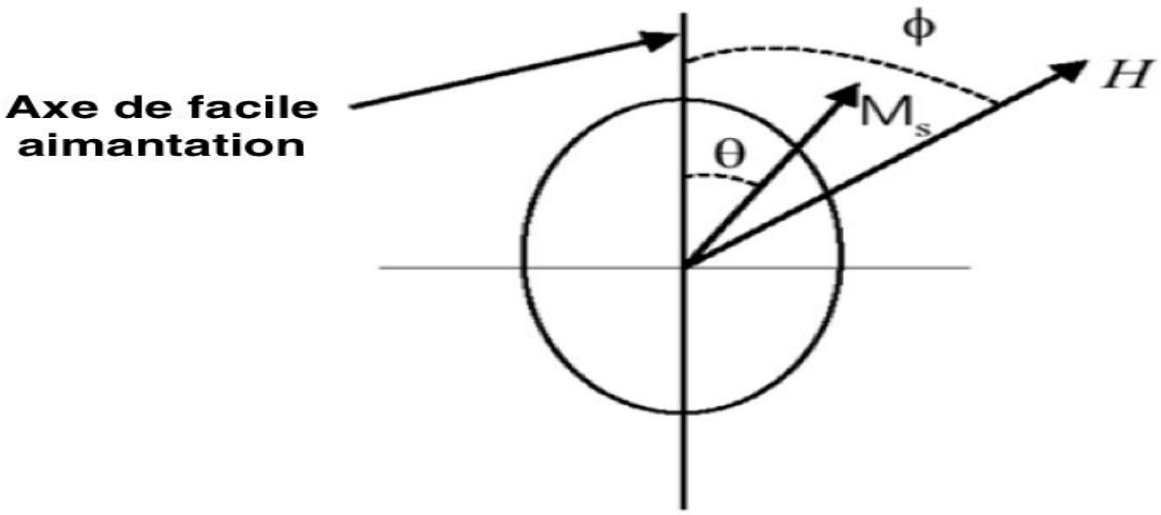


Figure 1. 6: Illustration of the variables used for the anisotropy and Zeeman energies. The applied magnetic field $H$ makes an angle $\phi$ with the easy axis of magnetization, and the angle $\theta$ with the magnetic moment [8].

The competition between the two energies $E_\alpha$ and $E_z$ is the origin of the hysteresis loop. The shape of the loop depends on the angle $\phi$ between the easy axis of magnetization and the applied magnetic field. Figure 1.7 shows that in the case where the magnetic field is parallel ($\phi = 0$) or antiparallel ($\phi = 180°$) to the easy axis of magnetization, the hysteresis loop is rectangular.

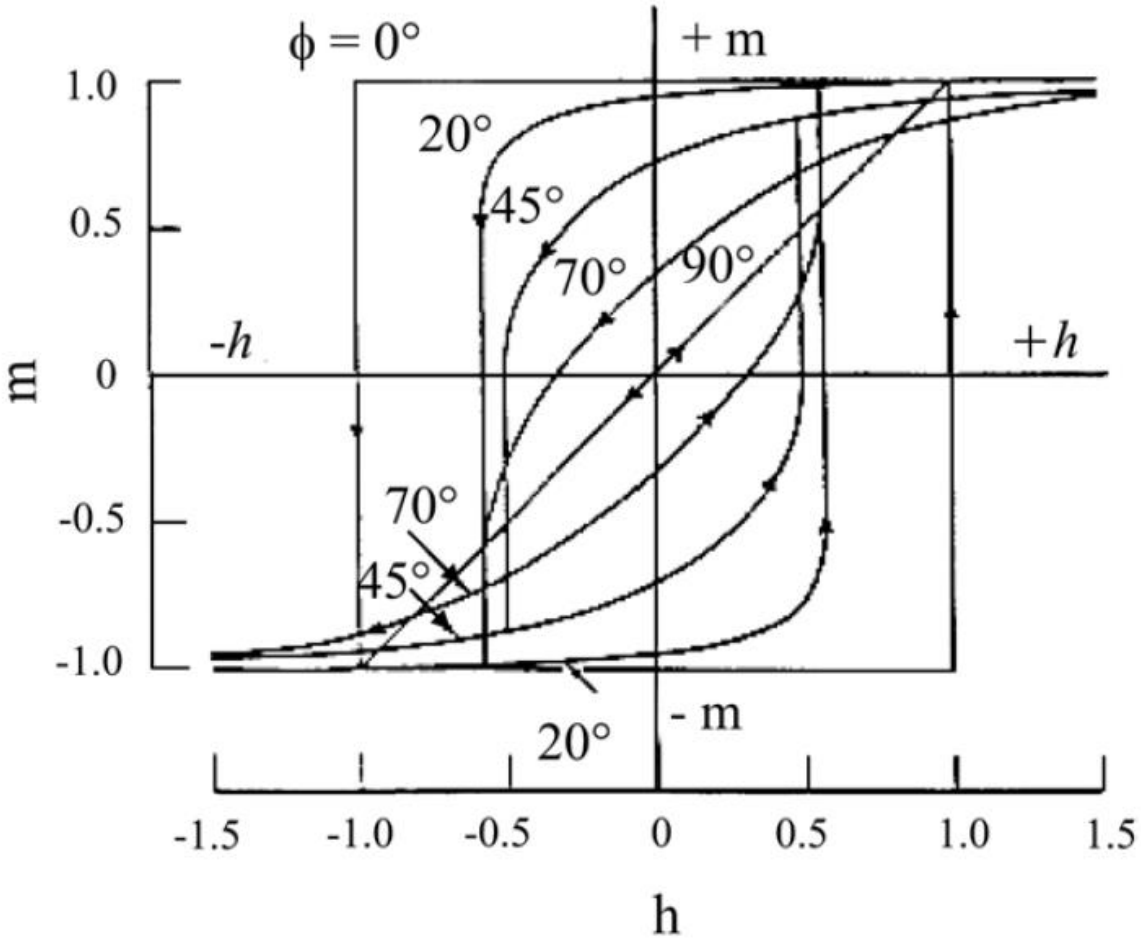


Figure 1. 7: Theoretical hysteresis loop of a monodomain particle for different angles $\phi$ between the anisotropy axis and the applied magnetic field. With $m = \frac{M}{M_S}$ ($M_S$ is the saturation magnetization) and $h = \frac{H}{H_C}$ ($H_C$ is the coercive field) [8].

The axis of anisotropy is randomly oriented towards the magnetic field $H$. It is necessary to average on all the orientations, and we obtain according to the model of Stoner-Wohlfarth [14]:

$$H_C \approx \frac{K_\alpha}{\mu_0 M_S} \tag{1.15}$$

Each material is therefore characterized by the anisotropy constant $K_\alpha$ which is related to the anisotropy energy. Hard magnetic material is characterized by a high anisotropy constant $K_\alpha$ and a large hysteresis loop. In this case, there is a permanent magnetic moment, which is an interest for many applications such as information storage [3]. On the other hand, soft magnetic material has a low anisotropy constant $K_\alpha$ and a narrow hysteresis loop. There is a reversible

magnetization, which is important in medical imaging or in drug delivery [15][16]. It is interesting to control this anisotropy constant and therefore the anisotropy energy.

### 1.2.3 Dynamic magnetic properties

In the case of the static magnetic properties of nanoparticles, the response time $\tau$ of nanoparticles was not taken into account:

- At $T = 300\ K$, particles follow the Langevin model and $\tau \ll t_{exp}$
- At $T = 0\ K$, particles follow the Stoner-Wohlfarth model and $\tau \gg t_{exp}$

Where $t_{exp}$ is the experimental measurement time (10-100 s). In reality, $\tau$ is never null or infinite, and its value governs the magnetic properties of particles when we are interested in dynamics for $\tau \approx t_{exp}$.

The solution in which the particles are dispersed has an influence on the dynamic magnetic properties. The particles synthesized in the laboratory are stabilized colloidally in a carrier liquid (ferrofluid). The carrier liquid may be aqueous or organic depending on the nature of the molecules present on the surface of nanoparticles [17]. The magnetic moment of nanoparticles dispersed in a solvent has two modes of rotation (Figure 1.8): an external rotation (Brownian relaxation) and an internal rotation (Néel relaxation). The dominant mode is the one whose average time between two reversals of the magnetic moment along the easy axis of magnetization is shortest.

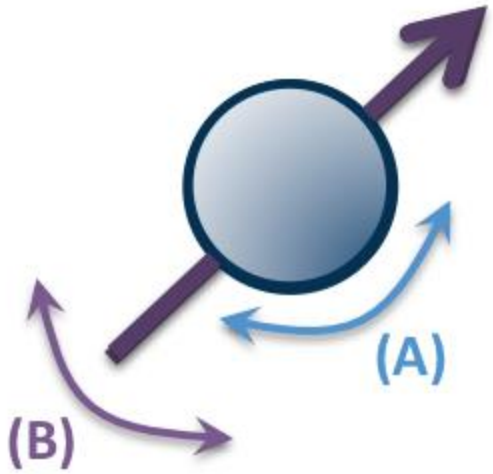


Figure 1. 8: Illustration of the two modes of rotation of magnetic moment: (A) external rotation (Brown) and (B) internal rotation (Néel).

Brown relaxation time $\tau_B$ is given by:

$$\tau_B = \frac{3\eta V}{K_B T} \tag{1.16}$$

Where $\eta$ is the solvent viscosity, $V$ is the particle volume, $K_B$ is the Boltzmann constant and $T$ is the temperature.

Néel relaxation $\tau_N$ is given by the following formula:

$$\tau_N = \tau_0 \exp(\frac{E_\alpha}{K_B T}) \tag{1.17}$$

Where $\tau_0 = 10^{-9} - 10^{-10}\ s$ is the test time, $E_\alpha$ is the anisotropy energy, $K_B$ is the Boltzmann constant and $T$ is the temperature.

Figure 1.9 shows the evolution of Néel relaxation time $\tau_N$ and Brown relaxation time $\tau_B$ of $CoFe_2O_4$ and $\gamma Fe_2O_3$ nanoparticles as a function of their size [18].

At room temperature in a liquid, the viscosity $\eta$ is low, $\tau_B \ll \tau_N$ regardless of $E_\alpha$. Nanoparticles have an external rotation (Brownian relaxation). The ferrofluid adopts a superparamagnetic behavior whatever the nature of the nanoparticles dispersed in this fluid: the magnetization curve which represents the magnetization as a function of the applied magnetic field ($M = f(H)$ is a reversible curve which does not present a hysteresis loop, the same curve is obtained as shown in Figure 1.5. When the field is cut, the magnetization vanishes and the system does not conserve remanent magnetization at a null applied field.

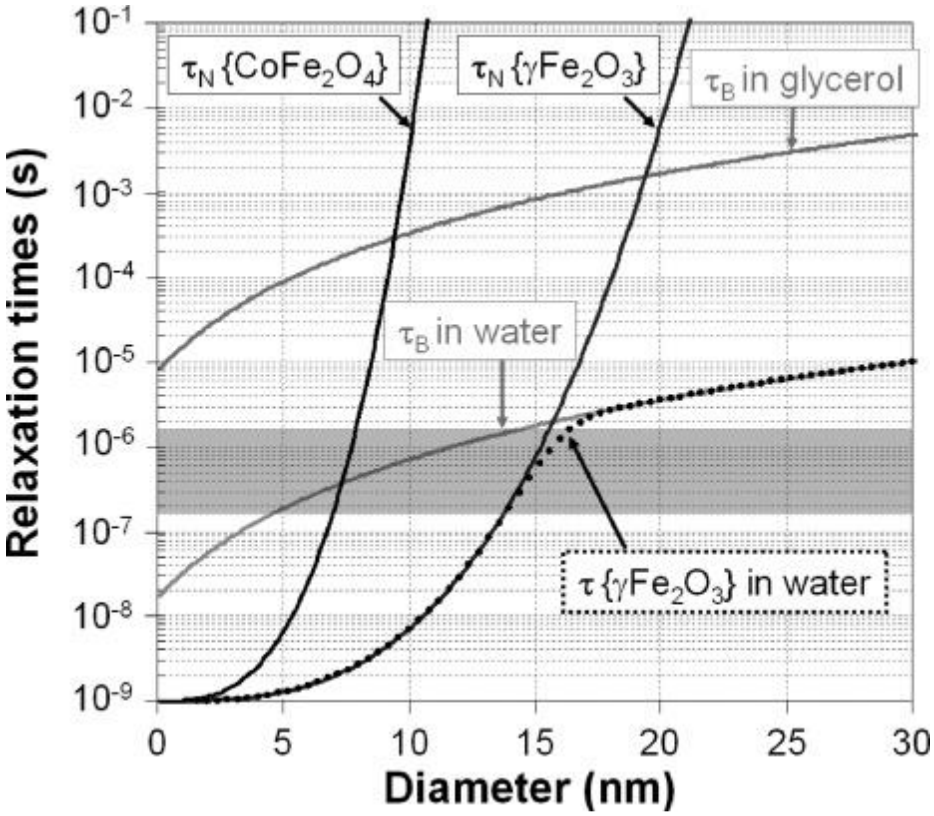


Figure 1. 9: Characteristic times (Néel relaxation time $\tau_N$ and Brown relaxation time $\tau_B$) of nanoparticles $CoFe_2O_4$ and $\gamma Fe_2O_3$ in different solvents as a function of their size [18].

When the system is frozen at low temperature (the carrier liquid is stiffened), there is no more Brownian relaxation because $\eta \to \infty$ therefore $\tau_B \to \infty$. The only rotation of the magnetic moment possible is an internal rotation (Néel relaxation).

- When the measurement time $\tau_m$ is greater than $\tau_N$, the particles are in the equilibrium state and have a superparamagnetic behavior. The magnetization curve is reversible (Figure1.4).
- When the measurement time $\tau_m$ is smaller than $\tau_N$, the particles are in the blocked state. The magnetization curve has a hysteresis loop (Figure 1.3) with a remanent magnetization $M_r$ and coercive field ($H_C$).

The transition from the blocked state to the equilibrium state occurs at the blocking temperature $T_B$ when $\tau_m$ is equal to $\tau_N$. In order to estimate this temperature, magnetization measurements according to the Zero Field Cooled and Field Cooled protocols are performed (Figure 1.10).

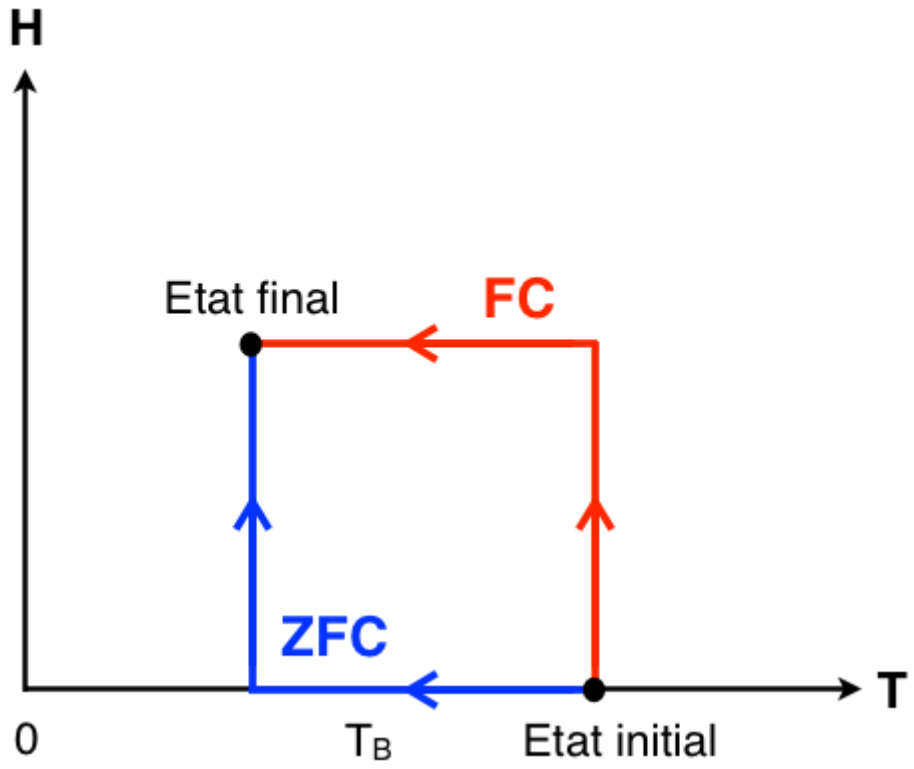


Figure 1. 10: Zero Field Cooled (ZFC) and Field Cooled (FC) protocols.

ZFC (Zero Field Cooled):

- The system is cooled under zero field. The particles are frozen and are in the blocked state.
- A weak magnetic field (100 Oe) is applied and the sample is magnetized very slowly because the relaxation time is very large. The gradual increase of the temperature makes it possible to unblock the magnetic moment, but the system is always blocked.
- The magnetization curve has a maximum corresponding to the blocking temperature. The system then transits from the blocked state to the equilibrium state.
- When the temperature is raised above $T_B$, the thermal fluctuations which tend to oppose the orientation induced by the applied field are increased. The magnetization decreases as expected in the Langevin model. The system is in an equilibrium state.

FC (Field Cooled):

- A weak magnetic field (100 Oe) is applied, then the system is cooled to the desired temperature under the applied field.

- The magnetization remains approximately constant as long as the system is blocked. The FC and ZFC curves meet when the system reaches the equilibrium stat at $T_B$ (Figure 1.11).

In fact, because of the particle size polydispersity, there is a $T_B$ distribution and an average of $T_B$ is experimentally measured.

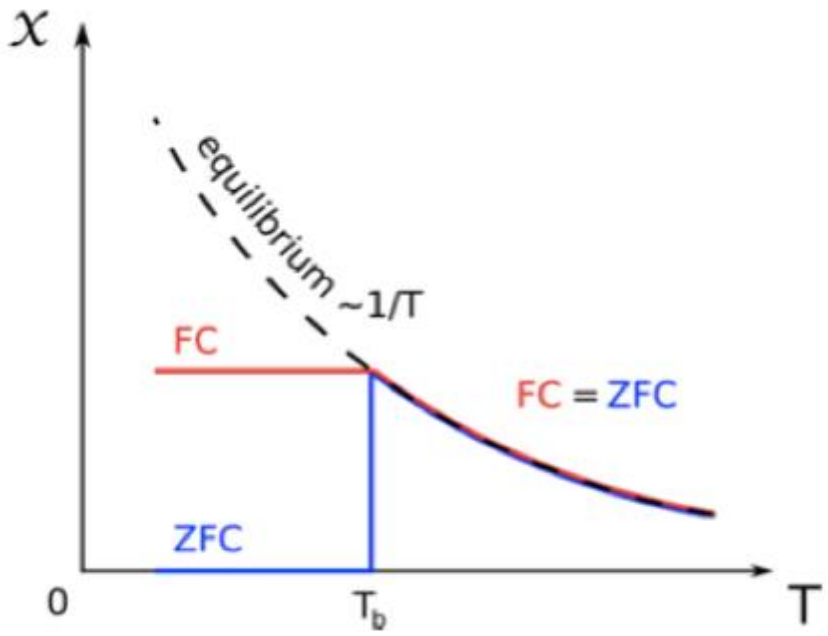


Figure 1. 11: Theoretical plot of susceptibility as a function of temperature for a Zero Field Cooled and Field Cooled protocols.

# 2 Synthesis of ferrite nanoparticles

## 2.1 Introduction

As we have seen in the first Chapter, the magnetic properties of nanoparticles are highly dependent on magnetocrystalline, shape and surface anisotropy energies. To adapt magnetic properties of nanoparticles for many applications such as magnetoelectric composites useful for sensor applications, it is, therefore necessary to modify the nature of the material, the shape and the size of nanoparticles.

Magnetic ferrite nanoparticles can be synthesized by either top-down (physical synthesis) or bottom-up (chemical or biological synthesis) methods. Figure 2.1 shows that chemical methods are the most published route to produce magnetic nanoparticles. In the following, the most popular chemical synthesis methods to produce magnetic nanoparticles will be introduced.

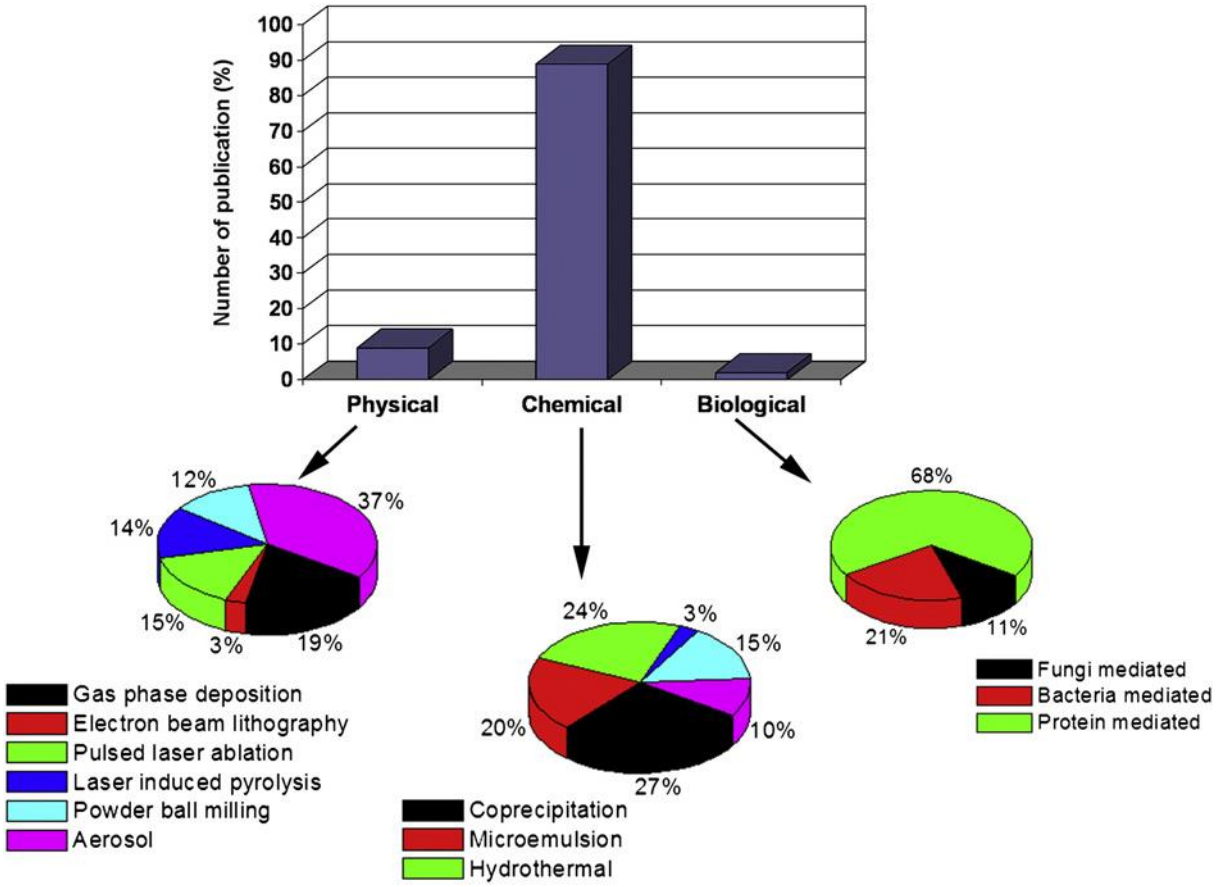


Figure 2. 1: A comparison of the three most published routes to synthesize magnetic nanoparticles.

To synthesis ferrite nanoparticles, many synthesis methods are described in the literature. The most common methods are Sol-Gel method [19], co-precipitation [20][21], hydrothermal synthesis [22][23], microfluidic [24], and thermal decomposition method [25][26].

In this chapter, we have chosen to describe these methods by presenting articles that show the influence of synthesis on the structural and magnetic properties of nanoparticles.

## 2.2 Sol-Gel method

Historically, this technique has been used since the second half of the twentieth century, it is increasingly used for the synthesis of nanoscale powders. The principle of this method is to develop a solid from a solution called "sol" (suspension of colloidal particles in a liquid) to a solid state called "gel", which is a semi-rigid solid, where the solvent is trapped in the solid material, which can be colloidal (concentrated or polymeric sol). The advantages of this method are the simplicity, speed, and chemical purity of the obtained materials. We describe in the following, our developed sol-gel process which applied to the elaboration of nanoparticles based on cobalt ferrite doped with nickel, where the precursors are mainly nitrates [19].

The steps of this process consist first in dissolving the precursors $Co(NO_3)_2$,$6H_2O$, $Ni(NO_3)_2$, $6H_2O$) and ($Fe(NO_3)_3$, $9H_2O$) in an organic solvent (Ethanol) in stoichiometric proportions and stir at room temperature for 10 min. In parallel, an amount of citric acid is dissolved in ethanol at a ratio of (1:1) for 10 min stirring, then, the two solutions are mixed gradually. After that, the reaction mixture is subjected to a treatment delivered by waves ultrasonic at 60 °C for 1 h. The solution is kept for 2 hours before to be dried at 100 °C to remove some organic materials. One part of the obtained powder was calcined for 6 h at 300 °C and the second part at 400°C for the same duration [19].

The powders were characterized by transmission electron microscopy to check the crystallite size and the morphology of $Co_{0.7}Ni_{0.3}Fe_2O_4$ nanoparticles. Figure 2.2 shows the distribution of $Co_{0.7}Ni_{0.3}Fe_2O_4$ nanoparticles calcined at 300 and at 400 C and their morphologies. It is noted that the nanoparticles are generally isometric and agglomerated.

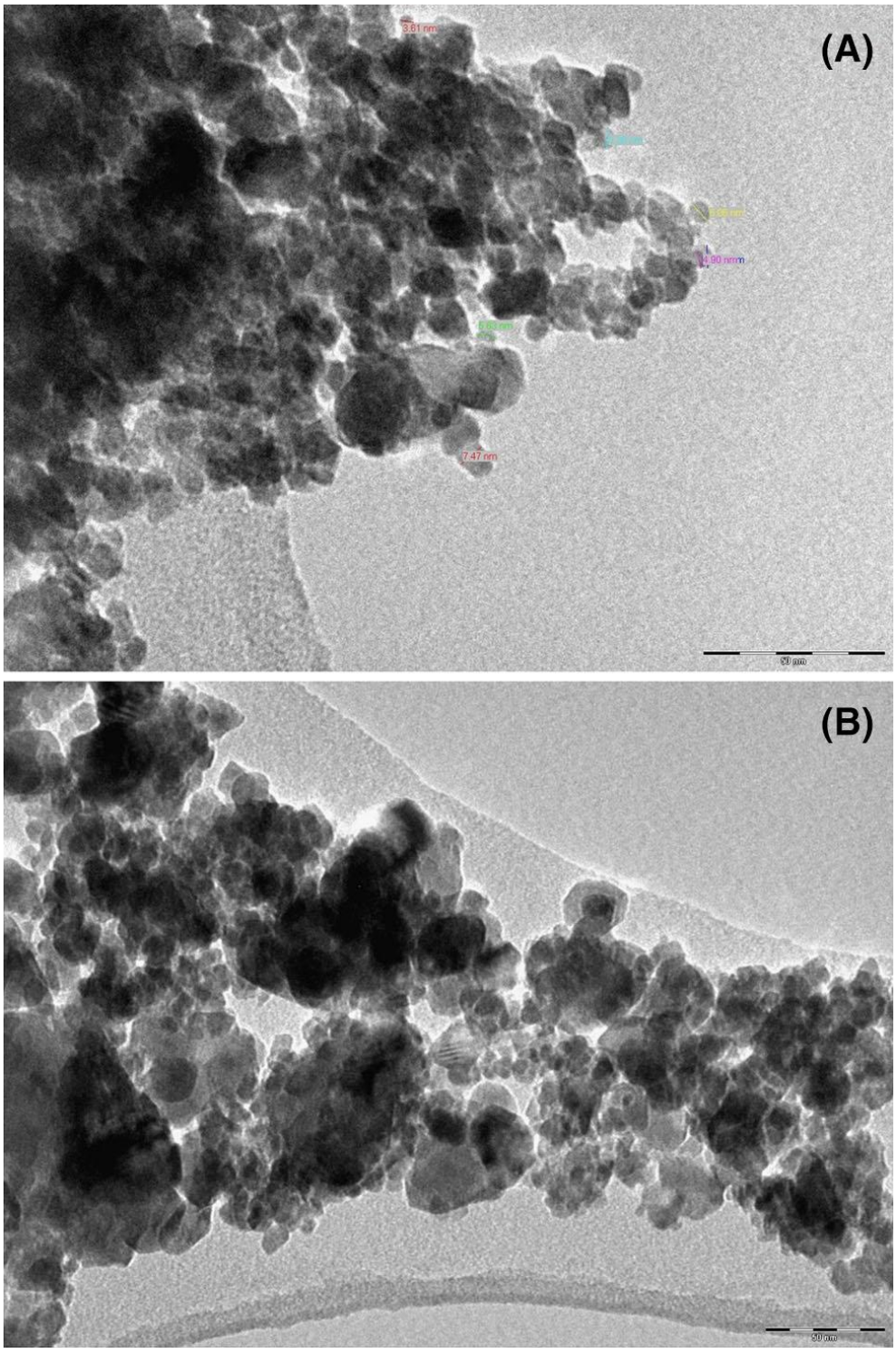


Figure 2. 2 : TEM images of $Co_{0.7}Ni_{0.3}Fe_2O_4$ nanoparticles calcined (a) at 300 °C and (b) $Co_{0.7}Ni_{0.3}Fe_2O_4$ nanoparticles calcined at 400 °C [19].

It interesting to mention that one of the major interests of the "sol-gel" process is the possibility of producing a wide range of gels doped by different types of dopants such as metallic particles, ions or magnetic nanoparticles (the subject of the present work) constituting however, the solid

phase of ferrofluid [27]. The insertion of specific dopants within the sol-gel method allows the creation of specific materials, opening the way for many applications.

- Advantages of the sol-gel method

This method has several advantages, the most interesting ones are:

* Low process temperature
* Composition of the final material controllable at the molecular level
* Excellent homogeneity
* The ease of production of complex systems

- Disadvantages of the sol-gel method

* Long process time
* Irregular particle sizes and shapes
* High precursor prices

## 2.3 Co-precipitation

The co-precipitation developed by Massart in the 1980's [28] is a method of synthesis by soft chemistry. It consists of an alkaline co-precipitation of $M^{2+}$ and $Fe^{3+}$ ions solubilized initially in acid solution to avoid the precipitation of hydroxides amorphous. This method allows to obtain various ferrite nanoparticles such as maghemite ($\gamma - Fe_2O_3$) [28], cobalt ferrite ($CoFe_2O_4$) [20], manganese ferrite ($MnFe_2O_4$) [29], or mixed ferrite [30][31]. The size of the obtained nanoparticles depends on the experimental conditions such as the base used for the co-precipitation, pH used for the precipitation, adjusted quantity (base in the acid mixture or vice versa). This synthesis method allows obtaining nanoparticles, which are macro ions and stabilized in aqueous solution by electrostatic repulsions. The ferrofluid is stable at pH=7, which is interesting for biological applications [32]. One of the disadvantages of this synthesis method is that the obtained nanoparticles do not have a regular shape and they are polydisperse in size as shown in Figure 2.3. To reduce this polydispersity, a sort in size process has been proposed [33].

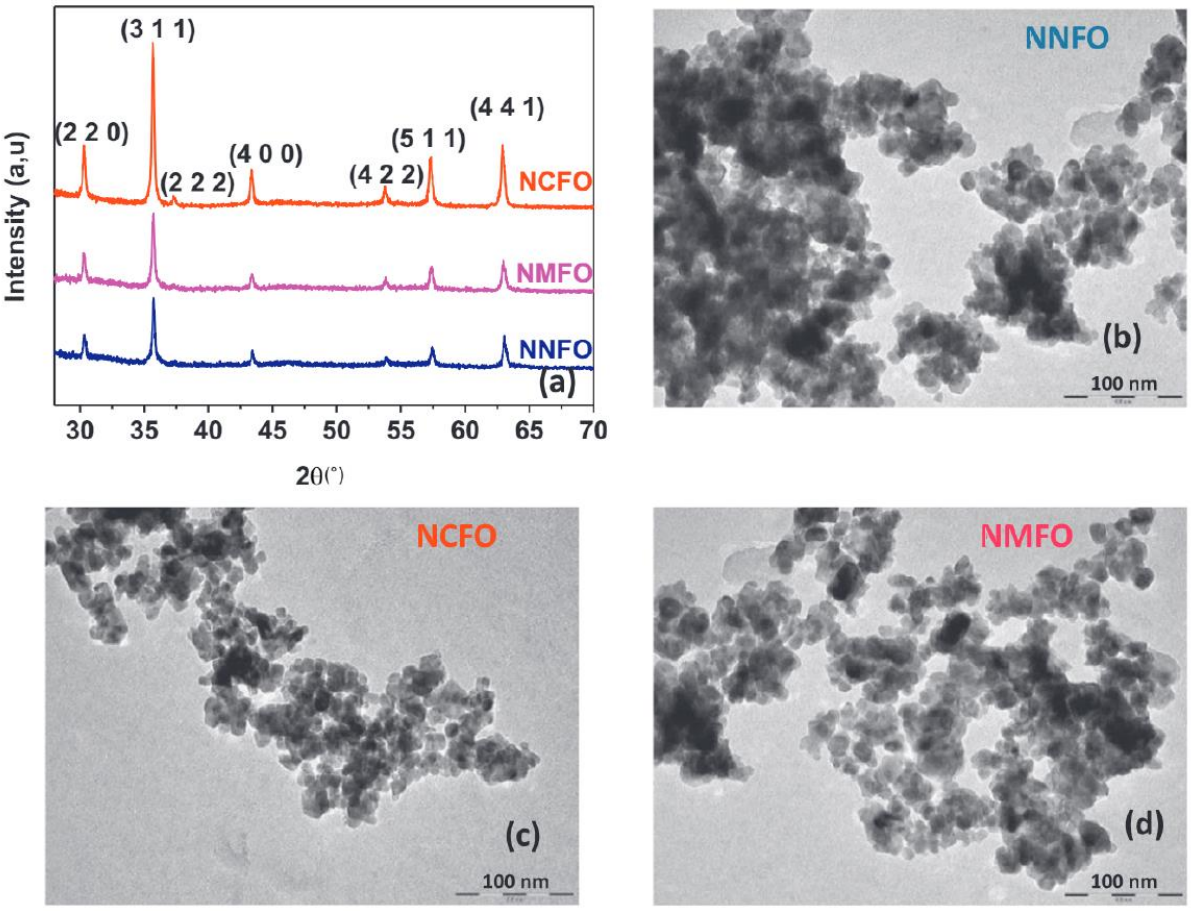


Figure 2. 3: TEM images of ferrites nanoparticles obtained by the co-precipitation method [31].

### 2.3.1 Particle size

The modification of certain synthesis parameters makes it possible to modify the size, the morphology or the crystallinity of the particles, and therefore on their magnetic properties.

Pereira et al. [34] have shown that the use of new bases such as Isopropanolamine (MIPA) and Diisopropanolamine (DIPA) during the co-precipitation synthesis has resulted in smaller $MnFe_2O_4$ ferrite particles with enhanced magnetic properties (see Table 2.1).

Indeed, for$Fe_3O_4$ particles, the constant of effective magnetic anisotropy $K_{eff}$ is increasingly high while the particle size decreases, when replacing the sodium hydroxide with Isopropanolamine and then with Diisopropanolamine. When the size is divided by two, the anisotropy constant is multiplied by two. For cobalt ferrite, for equivalent sizes obtained with isopropanolamine and diisopropanolamine, there is a factor of two for the anisotropy constants. The synthesized ferrite particles have high anisotropy constants for very small sizes (between 4.2 and 6.3 nm). Isopropanolamine and diisopropanolamine play a dual role in co-precipitation

as a base and complexing agent. They limit the growth of the particles which increases their specific surface area and modifies their magnetic properties.

| Nanomaterial | $d_{TEM}$(nm) | $\sigma_{TEM}$ | $T_B$(K) | $M_S\left(\frac{\text{emu}}{\text{g}}\right)$ at 300 K | $10^3 K_{eff}$ $(\frac{J}{m^3})$ |
|---|---|---|---|---|---|
| Fe_NaOH | 8.6 | 0.2 | 96.0 | 58.0 | 116 |
| Fe_MIPA | 6.3 | 0.2 | 70.0 | 64.8 | 181 |
| Fe_DIPA | 4.9 | 0.3 | 43.5 | 60.4 | 250 |
| Co_NaOH | 18.6 | 0.1 | 286.4 | 48.8 | 29.7 |
| Co_MIPA | 4.8 | 0.2 | 149.2 | 46.0 | 878 |
| Co_DIPA | 4.2 | 0.3 | 89.4 | 30.6 | 1810 |

Table 2. 1: Magnetic properties of $MnFe_2O_4$ nanoparticles synthesized with different bases [34].

Bee et al. [35] have also demonstrated that it is possible to reduce the size of the nanoparticles obtained by performing the co-precipitation in the presence of complexing agents. The maghemite particles were synthesized in the presence of sodium citrate [35], and cobalt ferrite particles in the presence of tartrate [21]. The addition of complexing agents before the addition of the base in the metal ion mixture makes it possible to limit the growth of the nanoparticles and to vary their mean diameter. Depending on the percentage of complexing agent added, it is possible to modulate the average size of the synthesized particles. When the proportion of complexing agent at the beginning of synthesis increases ($R$ is defined as the molar ratio between the amount of complexing agent and the total amount of metal ions), the particle size decreases (see Figure 2.4).

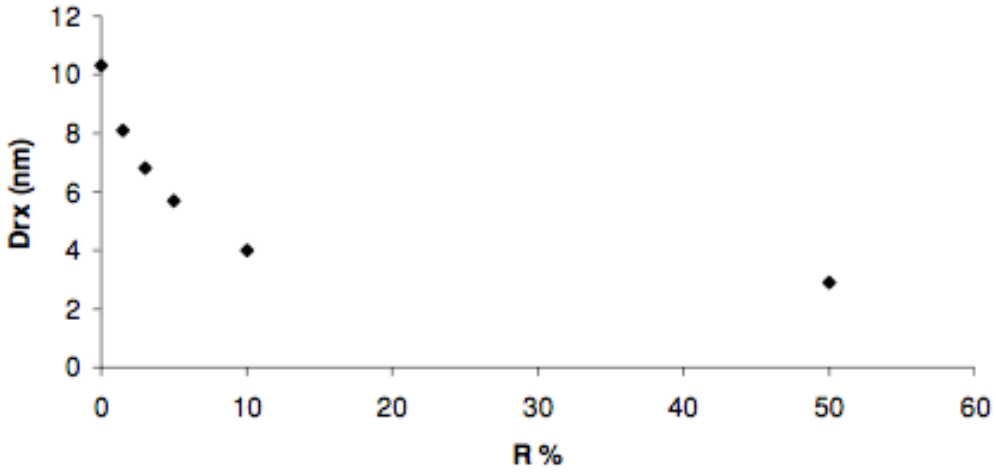

Figure 2. 4: Evolution of the diameter of cobalt ferrite nanoparticles as a function of the amount of complexing agent added [21].

### 2.3.2 Chemical composition of particles

In order to modify the magnetic properties of the synthesized particles, one of the methods used by Biswal et al. [36] is to play on the proportions of $Fe^{2+}$ and $Co^{2+}$ in $Co_{1-x}Fe(II)_xFe(III)_2O_4$ particles. They have shown that when the concentration of $Co^{2+}$ increases, the saturation magnetization of the particles increases until reaching a maximum of 90 $(\frac{emu}{g})$ for $x = 0.75$ (see Figure 2.5). A further increase in the concentration of $Co^{2+}$ ions decreases the magnetization. Similar results were observed for the coercive field, indicating that the incorporation of $Co^{2+}$cations in a $Fe-O$ matrix significantly improved the magnetic anisotropy of nanoparticles, with a maximum for particles of formula $Co_{0.25}Fe(II)_{0.75}Fe(III)_2O_4$.

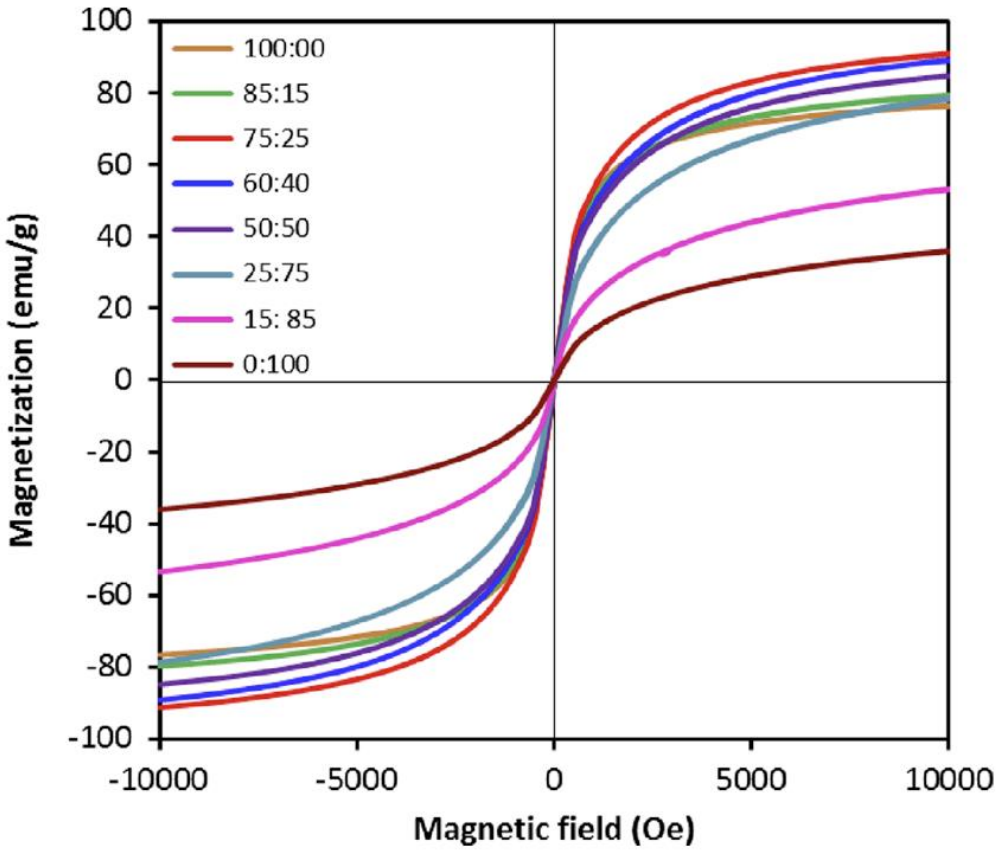


Figure 2. 5: Magnetization curves at 300 $K$ of $Co_{1-x}Fe(II)_xFe(III)_2O_4$ nanoparticles with different molar ratios of $Fe^{2+}$ and $Co^{2+}$ [36].

## 2.4 Hydrothermal method

Hydrothermal synthesis is an additional step in co-precipitation synthesis, which consists of an autoclave treatment inside a Teflon container that can withstand high temperatures.

Daou et al. [22] were the first to add a hydrothermal treatment at $250\ °C$ after a co-precipitation at $70\ °C$ of $Fe^{2+}$ and $Fe^{3+}$. They obtained magnetite particles of about 39 nm when the hydrothermal treatment lasted 24 hours (Figure 2.6 (A)). These large alkaline particles have a higher saturation magnetization than untreated particles (Figure 2.6 (B)).

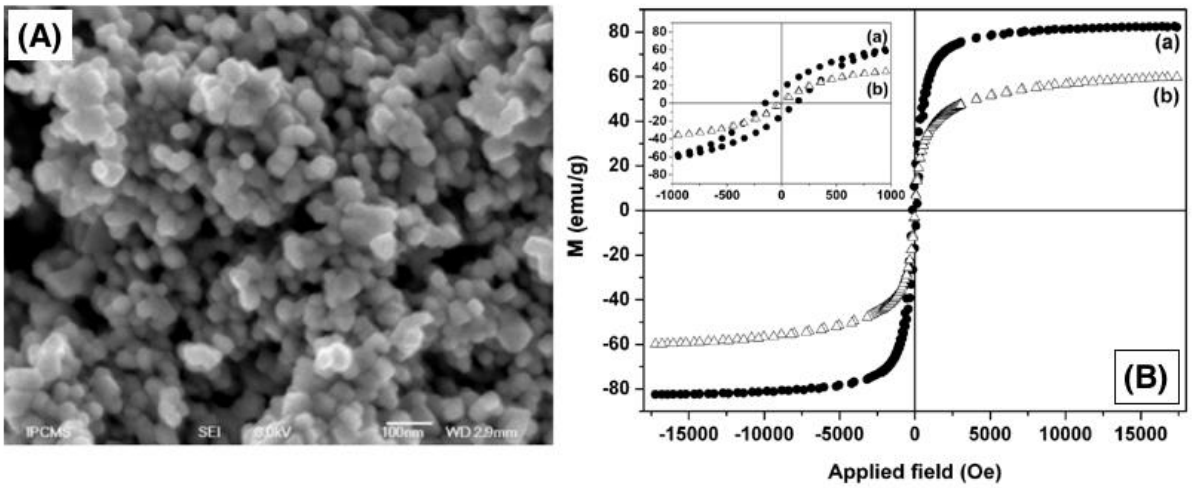


Figure 2. 6 : (A) Scanning electron microscopy image of nanoparticles of magnetite after 24h hydrothermal treatment. (B) Magnetization curves at room temperature of magnetite nanoparticles (a) before and (b) after hydrothermal treatment [22].

### 2.4.1 Influence of pH

One of the parameters allowing to play on the size of the particles in hydrothermal synthesis is the pH of the solution in autoclave. Nanoparticles of maghemite with sizes between 10 and 100 nm have been obtained by Horner et al. [23] (Figure 2.7).

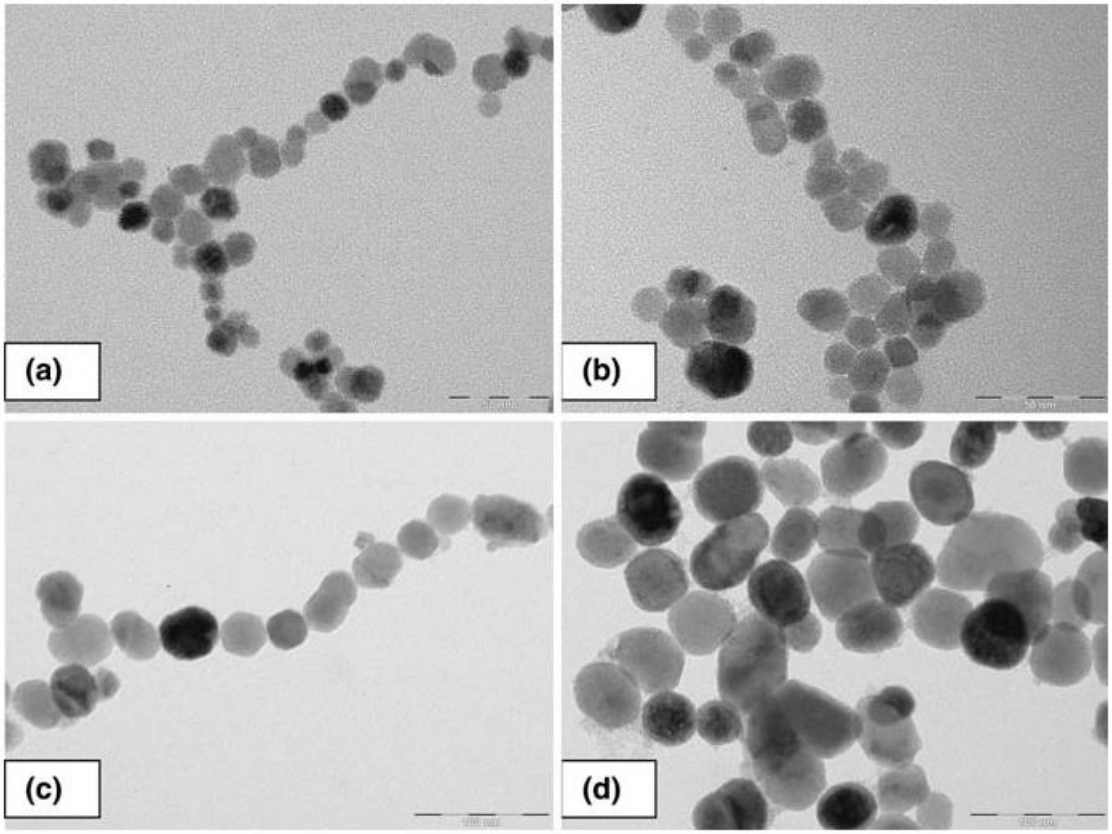


Figure 2. 7 : TEM images of nanoparticles of maghemite obtained after a hydrothermal treatment at $200\ °C$ with: (a) t = 2h, pH = 12 (soluble particles)); (b) t = 2h, pH = 12 (insoluble fraction); (c) t = 24h, pH = 12; (d) t = 2h, pH = 14, with t the incubation time in autoclave [22].

Table 2.2 shows that the particle size increases with pH. Alkalization of the $Fe^{2+}$ and $Fe^{3+}$ mixture at a higher pH tends to increase the number of the particles in the solution, which then results in the formation of larger particles during Ostwald ripening process.

| Time (h) | pH = 9.6 | pH = 12 | pH = 14 |
|---|---|---|---|
| 2 | - | 13 nm / 22 nm | 52 nm |
| 24 | 27 nm | 55 nm | 30 nm / 110 nm |

Table 2. 2: Average sizes (from the TEM pictures) obtained in different experimental conditions at T = 200 °C [23].

### 2.4.2 Duration of hydrothermal treatment

In addition to magnetite and maghemite, cobalt ferrite nanoparticles have been synthesized by hydrothermal synthesis [37][38]. Another parameter for controlling the average particle diameter is the duration of the hydrothermal treatment.

Cabuil et al. [39] synthesized cobalt ferrite nanoparticles with different hydrothermal heating times (see Figure 2.7). The longer the treatment in the autoclave is, the more the particles enlarge by Ostwald ripening and are also more spherical and better crystallized.

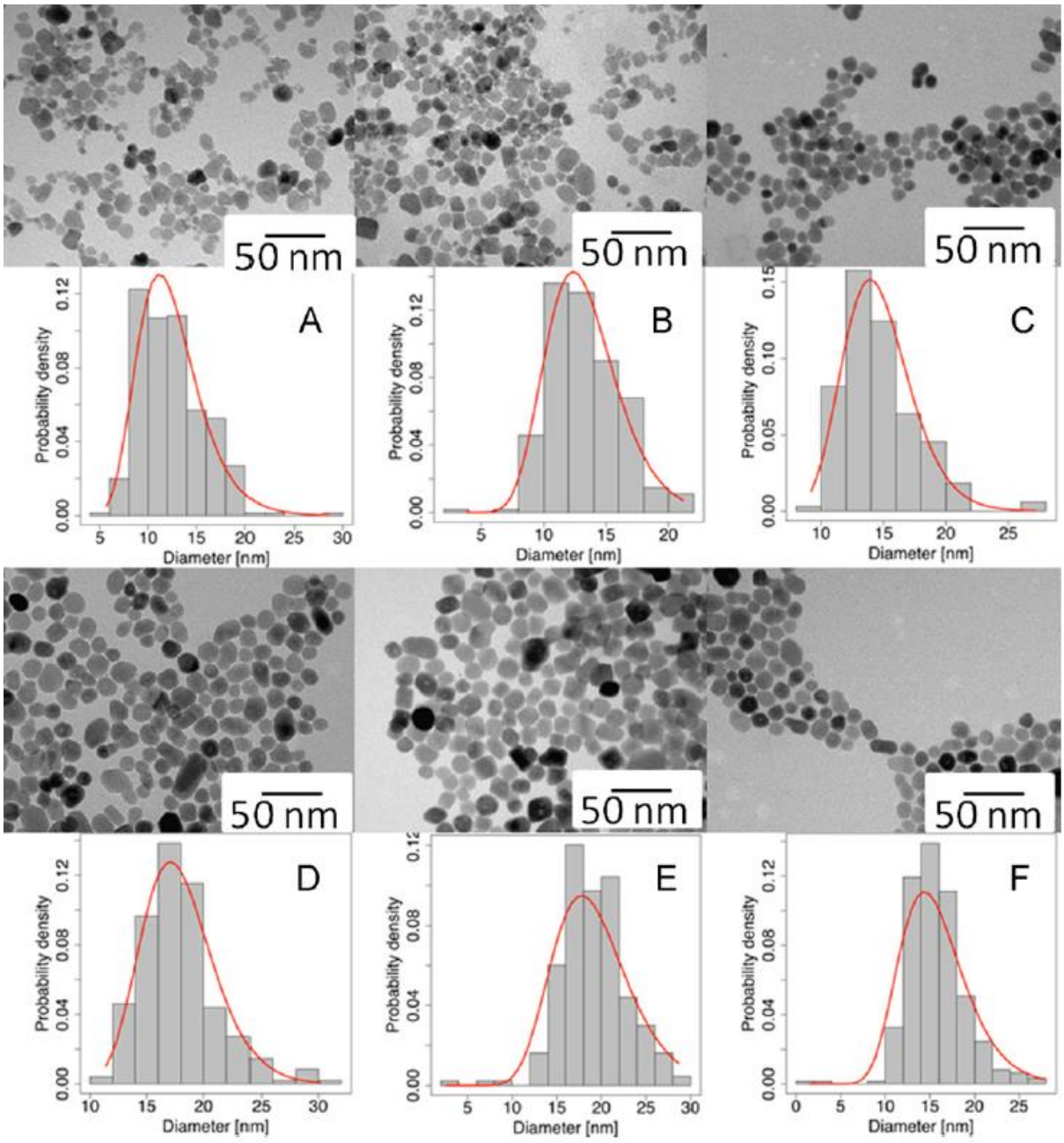


Figure 2. 8: TEM pictures and corresponding histograms. (A): classical heating at 100 °C for 1 h; (B): hydrothermal treatment at 100 °C for 1 h; (C): hydrothermal treatment at 200 °C for 1 h; (D): hydrothermal treatment at 200 °C for 24 h; (E): hydrothermal treatment at 200 °C for 120 h and (F): hydrothermal treatment at 200 °C for 24 h in the presence of citrate ions (5%).

## 2.5 Thermal decomposition method

Thermal decomposition method is a process of decomposing complexes at the reflux temperature of the solvent [40]. These complexes may be acetylacetonate [41], stearate [42] or oleate [43]. The solvents used are varied (benzyl ether, phenyl ether, octadecene ...) but they all have a high boiling point (Table 2.3) [42].

| **Solvents** | **Boiling point (°C)** |
|---|---|
| Benzyl ether | 298 |
| Phenyl ether | 259 |
| Octadecene | 318 |
| Hexadecanol | 344 |
| Eicosene | 330 |
| Docosene | 365 |

Table 2. 3: Boiling temperatures of various solvents used in the thermal decomposition method [42].

Experimental results concerning the control of particles size can be interpreted in the framework of the nucleation and growth mechanisms proposed by LaMer et al [44]. The desired narrow size distribution is achieved by separating the nucleation from the growth steps of particles. By precisely controlling supersaturation, a large number of germs are created at the same time, and these grow in second time without forming of new germs. Due to the simultaneous nucleation of all particles, their growth is identical and monodisperse particles in size and shape are obtained. The precursor can be dissolved at room temperature, and heated to its decomposition temperature, which releases the ions or metals; or added directly to the hot-injection solution which induces abrupt decomposition and rapid release of ions or metals. The synthesis is done in the presence of ligands (oleic acid for example) which cover the surface of particles and ensures their colloidal stability in the apolar solvents.

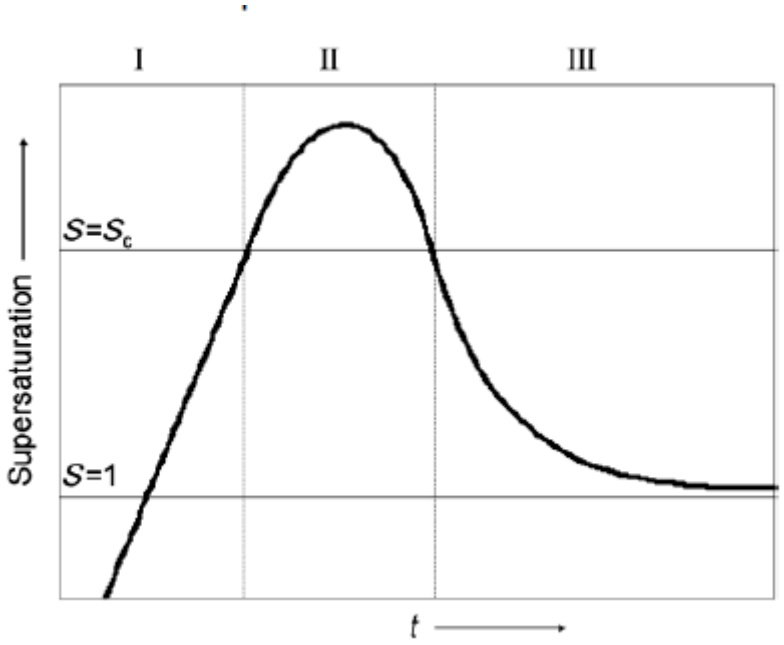


Figure 2. 9: Schematic representation of the concentration of molecularly dissolved sulfur before and after nucleation as a function of time [44].

During thermal decomposition synthesis of acetylacetonate complexes, the complexes are heated to a certain temperature at which precursors decompose, which greatly increase the concentration of $Fe^{3+}\ and\ M^{2+}$ $(M = Fe, Co, Mn, Ni, Zn \ldots)$ in the solution, inducing the homogenous nucleation of the germs (Figure 2.9, Phase I). However, these are too small to be stable, and they dissolve quickly. By continuing to increase the supersaturation, a critical threshold is reached, beyond which stable germs are formed, which causes a concentration drop of $Fe^{3+}\ and\ M^{2+}$ in the solution (Figure 2.9, phase II). When the supersaturation goes back below this critical threshold, the nucleation stops and the decomposed precursors serve to increase the size of nanoparticles (growth step), a phenomenon that continues as long as the solution remains supersaturated. (Figure 2.9, phase III).

Noting this method makes it possible to obtain monodisperse ferrite particles $MFe_2O_4$ $(M = Fe, Co, Mn, Ni, Zn \ldots)$, because the nucleation and growth steps are decorrelated [45]. Indeed, in the case of acetylacetonate complexes, they begin to decompose from $200\ °C$ creating germs that will condense at a higher temperature. The disadvantage of this synthesis is that a large number of precursors are reduced during the nucleation step, and only a small amount of precursors will be available for the growth step (Figure 2.10(a)). Thus, the particles synthesized by this method have a limited size of 12 nm.

To increase this size limit, Muscas et al. [45] worked under controlled atmosphere. The authors observed that decreasing the amount of oxygen in the reaction environment reduced the reactivity of the precursors, so the nucleation is slower. However, this is not yet complete when the growth stage begins, and two particle sizes are synthesized (Figure 2.10(b)). By increasing the synthesis time, a final stage of Ostwald ripening makes it possible to decompose the smallest particles so that they condense on larger ones.

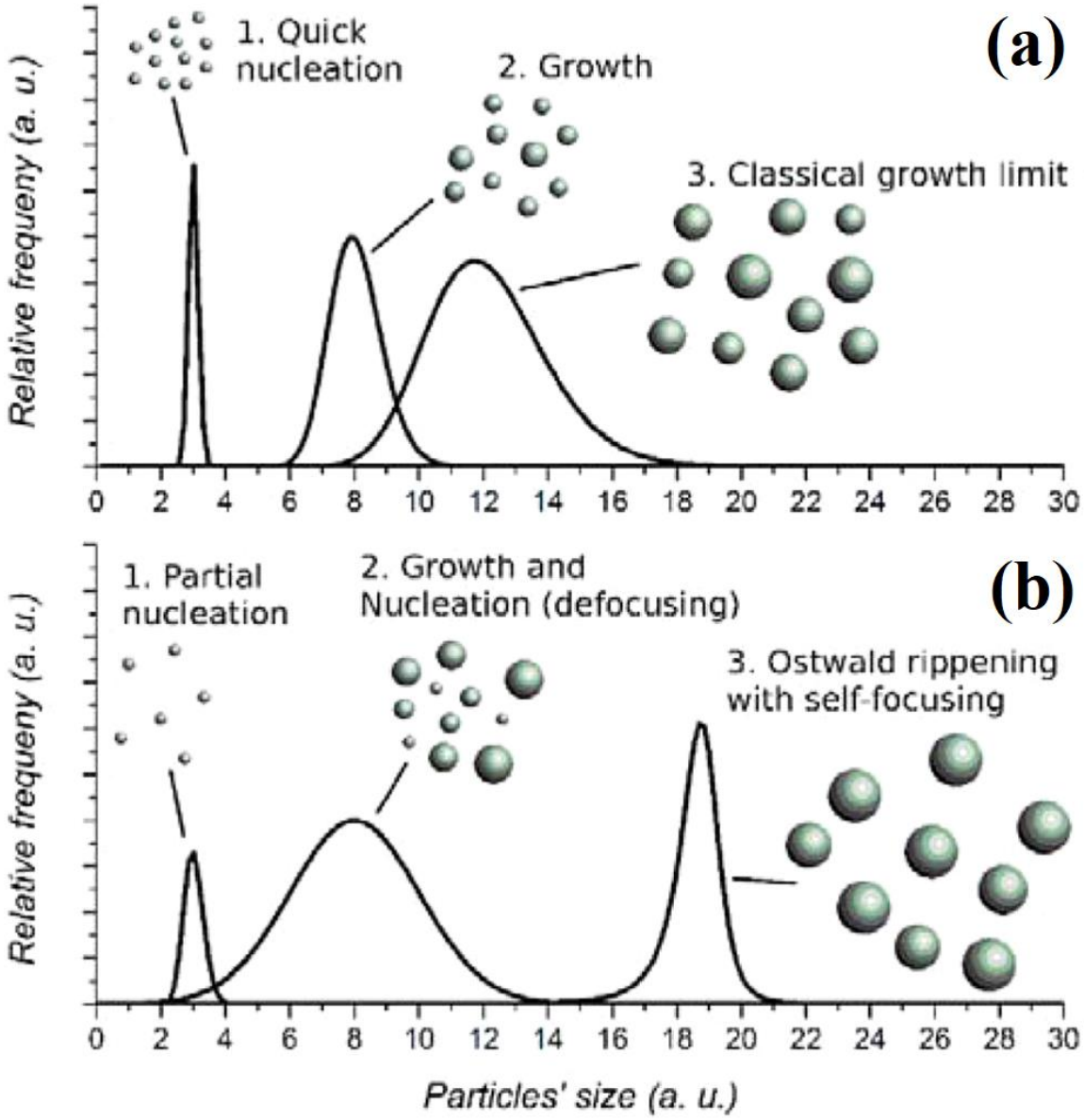


Figure 2. 10: Different steps of thermal decomposition method (a) classical synthesis and (b) under a controlled atmosphere [45].

Another process to increase particle size is sprout growth [46]. The principle of this method is to grow a second layer of $MFe_2O_4$ on previously synthesized ferrite nanoparticles (Figure 2.10). In such a case, the particles obtained can reach a size of 20 nm.

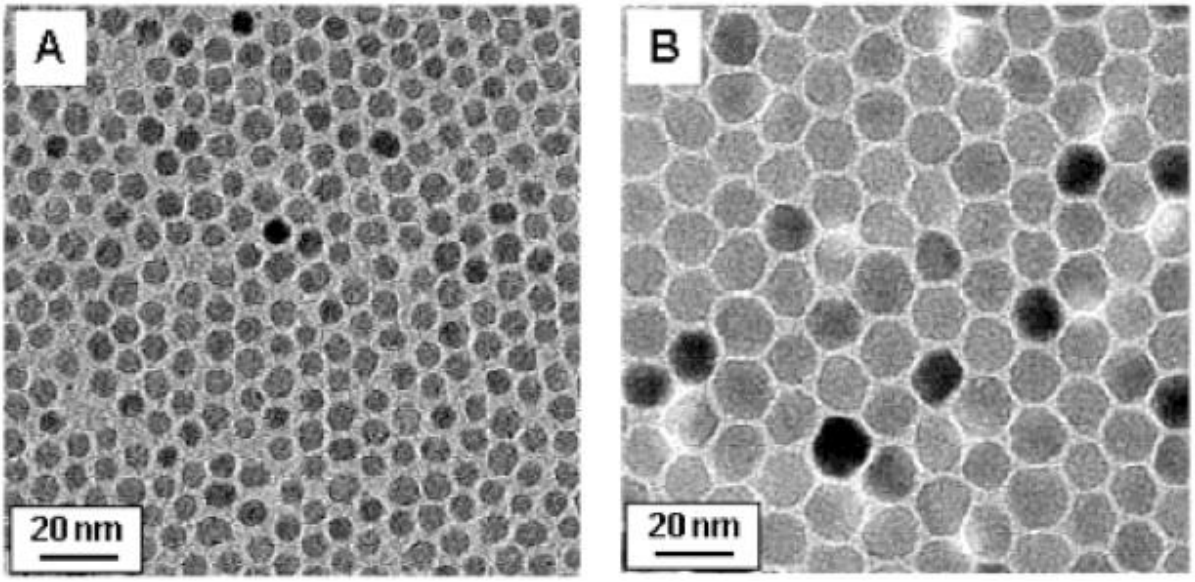

Figure 2. 11: TEM images of $Fe_3O_4$nanoparticles of 6 nm (A) and 12 nm (B) [46].

### 2.5.1 Particle morphology

Thermal decomposition method also makes it possible to obtain nanoparticles with a controlled morphology [26] (Figure 2.12). It is well known that the morphology of nanoparticles can be controlled by the nucleation and growth processes which are in turn strongly influenced by the synthesis conditions, such as the concentration of reagents, solvents or reaction time and temperature [47].

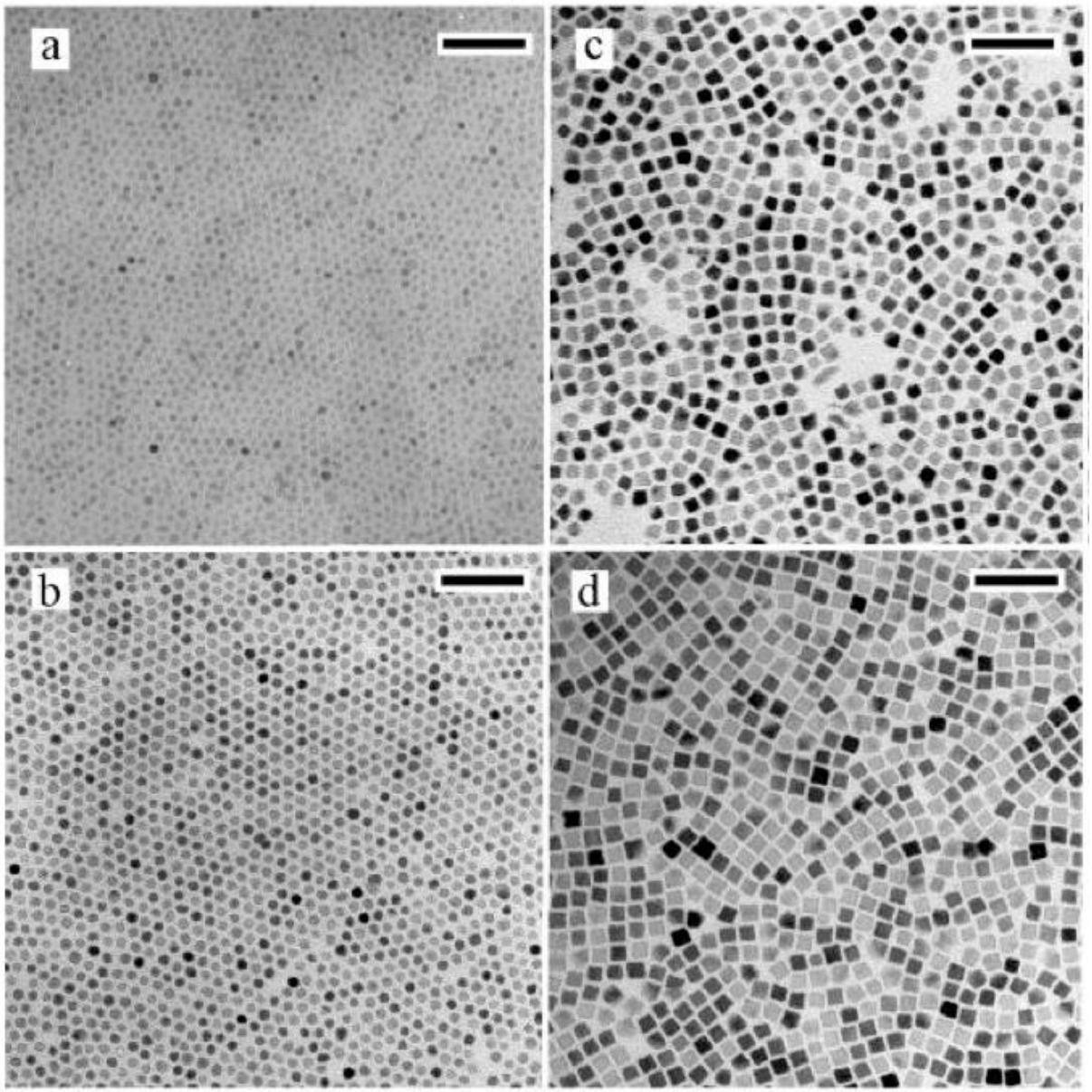


Figure 2. 12: TEM images of spherical and cubic $CoFe_2O_4$ nanoparticles of (a) 5.2 nm and (b) 7.9 nm, (c) 9.1 nm and (d) 10.9 nm [26]. Scale bar : 50 nm.

The morphology and size of the particles have an influence on their magnetic properties (Figure 2.13). Saturation and remanent magnetizations increase as particle size increases, without difference between cubic and spherical particles. The increase of the coercive field is not linear with the size and presents a maximum for particles of 10 nm. In addition, nanocubes have a lower coercive field than nanospheres.

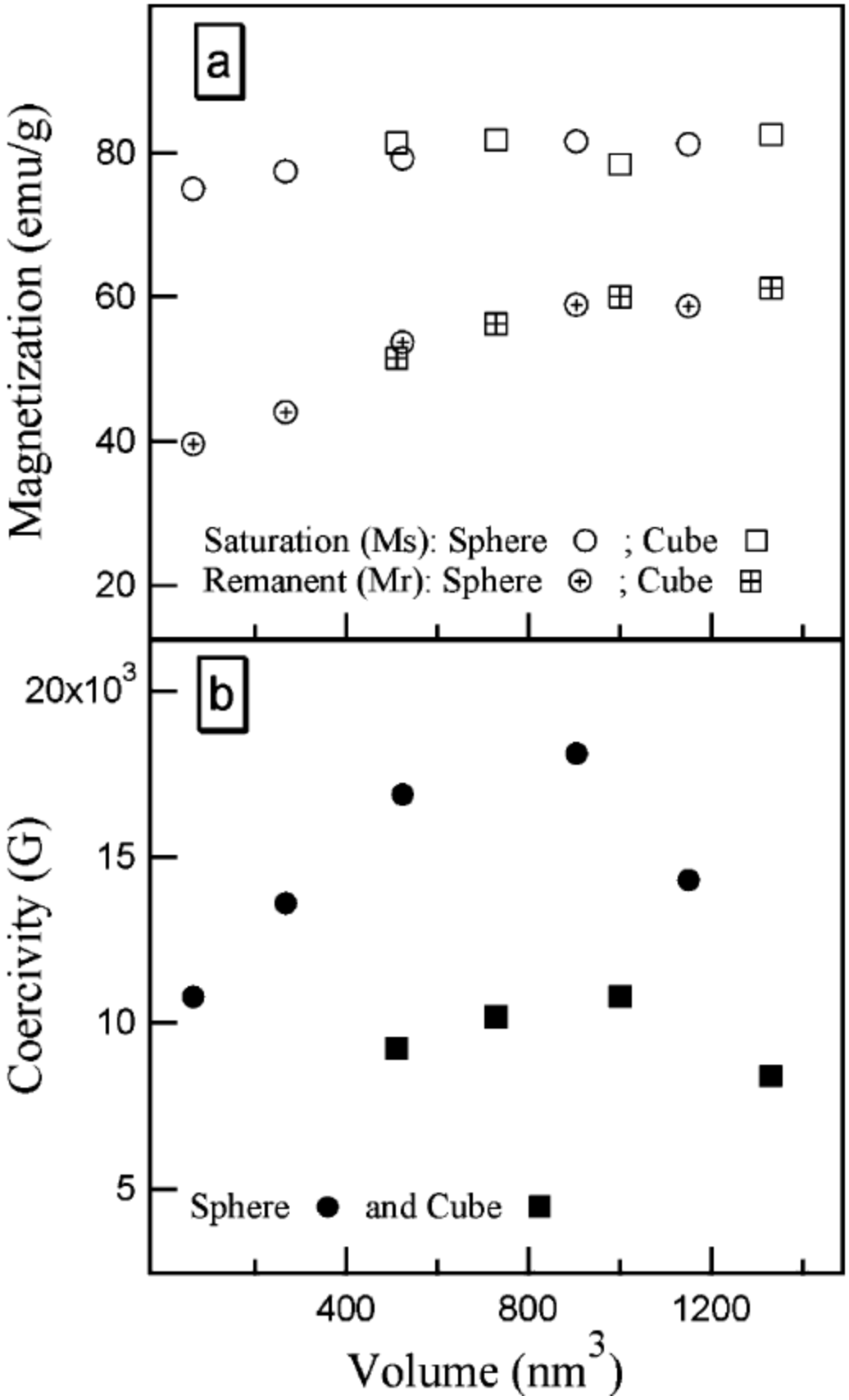


Figure 2. 13: (a) Saturation and remanent magnetization, and (b) coercive field as a function of volume for both cubic and spherical nanoparticles [26].

## 2.6 Conclusion

The advantages and disadvantages of the four synthesis methods mentioned above are briefly summarized in Table 2.4. As we can depict from the table, the Co-precipitation method is the simplest technique and it allows to control composition. However, in terms of the size and morphology control of nanoparticles, thermal decomposition seems to be the best method developed so far. Though, microemulsions method can also be used to synthesize monodisperse nanoparticles with specific morphologies. Nevertheless, this method requires a large amount of solvent. Finally, hydrothermal synthesis remains a relatively unexplored method for the synthesis of magnetic nanoparticles, although it allows elaborating materials with excellent crystallinity.

| Synthesis methods | Synthesis conditions | T(°C) | Reaction time | Solvent | Size (nm) | Size distribution | Morphology control |
|---|---|---|---|---|---|---|---|
| Sol-Gel | Very easy | 20-80 | Minutes | Water and Ethanol | <40 | Relatively narrow | Medium |
| Co-precipitation | Very easy | 20-90 | Minutes | Water | <20 | Relatively narrow | Medium |
| Hydrothermal | Simple at high pressure | 220 | Hours and Days | Water and Ethanol | <20 | Narrow | Very good |
| Thermal decomposition | Complicated | 200-320 | Hours and Days | Organic | <10 | Very narrow | excellent |

Table 2. 4: Comparison of the main characteristics of the most used ferrite synthesis methods [7].

It should be mentioned that ferrite nanoparticles with spinel structure have a very interesting magnetic properties, especially a strong saturation magnetization. However, they are very sensitive to agglomeration.

The objective of the next chapter is to develop a method to synthesis monocrystalline and monodisperse $CoFe_2O_4$ nanoparticles with control of size, morphology, and monodispersity. For that, the sensitivity to oxidation should be lower and the nanoparticles should exhibit a magnetic behavior at room temperature close to that of the bulk. In addition, few methods have

been used in the literature to develop monocrystalline and monodisperse $CoFe_2O_4$ nanoparticles with sizes less than 30 nm.

In the present work, we have used a method based on “thermal decomposition” for the synthesis of nanoparticles of cobalt ferrite. This method was proposed by Song et al [26] to elaborate Spinel Cobalt Ferrite Nanocrystals.

Noting that our choice to use this method is justified by the fact that this technique is simple and inexpensive. In addition, with this method, it is possible to generate crystallite sizes of interest for magnetic, catalytic and electronic applications. Further, it requires a single chemical reaction and there is no need for subsequent crystallization annealing. Furthermore, the solvent used is benzyl ether, known by its low-toxicity and usually used as a food and cosmetic additive.

# 3 Characterization techniques

In recent years, the invention of powerful analytical tools like Scanning Transmission Electron Microscope (STEM) has made the study of nanoparticles more versatile and interesting. In addition, there are other characterization techniques that we have used to characterize the ferrite nanoparticles and will be discussed below:

## 3.1 X-Ray Diffraction (XRD)

X-ray diffraction is the basic technique of the characterization of materials; it allows the determination of phase and purity of a crystalline material, by using the capacity of the material to deflect the X-ray beam. X-ray diffraction allows accessing to many information contained in a very arrangement of atoms within a crystallized material. The type of geometric arrangement, the unit cell parameter, and the size of the nanoparticles.

The principle of this technique consists of projecting an X-ray beam onto a crystal lattice constituted by the atomic planes. This beam is diffracted by the sample at a specific angle, following the Bragg law [48].

$$\lambda_x = 2d \sin\theta$$

Where $d$ is the distance between two cristal planes, $\lambda_x$ is the wavelength of the incident beam (X-ray) and $\theta$ is the diffraction angle.

The variation of the angle $\theta$ makes it possible to obtain a diagram consisting of reflections whose positions and heights depending on the crystal structure and the nature of the compound under study. The study of the width of the reflections of the diagram allows measuring the average size of the crystallites as well as the rate of distortion of the material, whereas the position of these reflections allows measuring the inter-plane distance, which is the unit cell parameter of the sample.

In this study, structural analysis were performed on a Bruker D8 Discover diffractometer (Nanotechnology Platform, MAScIR Foundation. Figure 3. 1) under CuKα1 radiation (λ=1.5406 Å) at room temperature, scanning angle $2\theta$ ranging from 10° to 100° with a step of 0.1°. The objective of this analysis is the determination of the phases present in the samples, verification of the absence of secondary phases, the calculation of the unit cell parameter as well as the determination of the particle size.


Figure 3. 1: Bruker AXSX-ray diffraction system

### 3.1.1 Determination of unit cell parameter.

The studied materials adopt a cubic symmetry relating to the structure of the spinel type. The unit cell parameter can be determined using the Bragg formula and that of the inter-reticular distance as a function of the unit cell parameter.

$$d_{hkl} = \frac{1}{\sqrt{\frac{h^2}{a^2} + \frac{k^2}{b^2} + \frac{l^2}{c^2}}}$$

$$2d_{hkl} \sin \theta_{hkl} = \lambda$$

Where:

- $d_{hkl}$: the inter-reticular distance of the planes hkl
- h, k, and l: the Miller indices of the lattice planes
- a, b, and c: unit-cell dimensions of the crystal
- $\lambda$: is the wavelength of the X-ray beam, in our case the wavelength used is that of copper ($\lambda$ = 1.5407 A°)
- $\theta_{hkl}$ or $\theta$ is the diffraction angle

Then, the unit cell parameter can be deduced by the following formula:

$$a = \frac{\lambda\sqrt{h^2 + k^2 + l^2}}{2\,(\sin\theta)^2}$$

### 3.1.2 Determination of crystallite size.

Another application of X-Ray diffraction is in the determination of crystallite size. This can be done by evaluating the broadness of the peak using the Scherrer equation:

$$D = \frac{0.9\lambda}{\beta cos(\theta)}$$

Where $D$ is the particle diameter, 0.9 is Scherrer constant, $\lambda$ is the wavelength, $\theta$ is the angle of diffraction and $\beta$ is the Full width at half maximum (FWHM) of a reflection.

## 3.2 Raman spectroscopy

The Raman scattering is discovered by C.V Raman and K.S. Krishnan (in 1928) in India, and G. Landsberg and L. Mandelstam in the Soviet Union. They have detected another scattering than Rayleigh scattering when they illuminate a liquid or a solid. This scattering is inelastic, with a frequency different from the excitation light, unlike the Rayleigh scattering, which is an elastic diffusion without frequency change. This inelastic scattering is called Raman scattering.

To study Raman scattering during this thesis, a Raman spectrometer (Figure 3. 2, Jobin Yvon T64000) equipped with a monochromator, and two premonchromers were used. A high-resolution CCD camera cooled with nitrogen is integrated into the system. For the excitation, we use a gas laser (Krypton) with a variable wavelength (457nm, 488nm, 514nm, 568nm, 647nm).

This spectrometer belongs to the laboratory of physics and condensed matter at Picardie Jules Verne University.

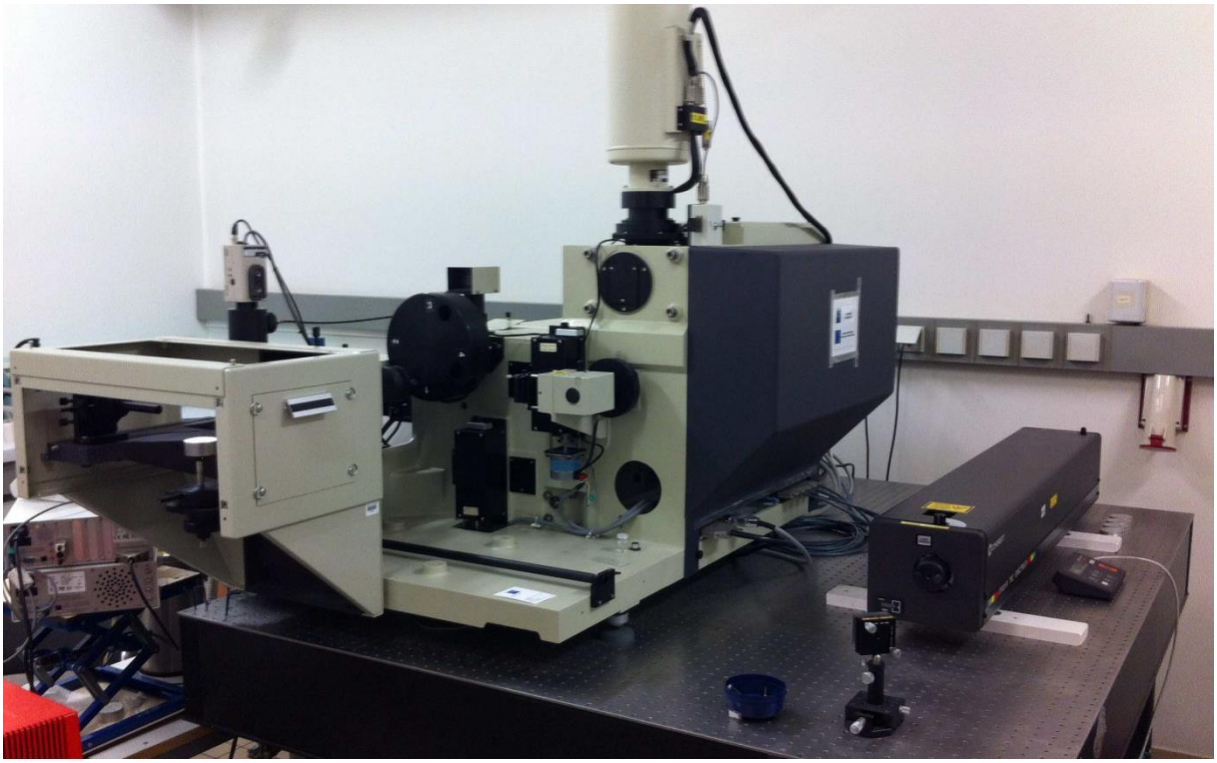

Figure 3. 2: Raman Spectrometer T64000

Raman spectroscopy is based on the study of phonons (the quantization of the vibrations of a crystal structure). Each of these vibrations is characterized by a frequency ω and a wave vector $\vec{q}$ unique. Their energy E and pulse P are expressed by the following relations:

$$E = \hbar(\vec{q}, j)$$

$\vec{P} = \hbar q$ Vibration waves are either longitudinal waves or transverse waves. The number of vibrations (mode) in a crystal corresponds to 3N, with N the number of atoms in the elementary crystal lattice. Three modes always correspond to the acoustic modes and the remaining 3N-3 modes correspond to optical modes.

Raman Spectroscopy is a powerful tool for the characterization of thin films and powders due to its high sensitivity to many lattice effects such as structural transition and lattice distortion. Ferrite crystallizes in cubic spinel structures belonging to the space group Fd-3m ($O_h^7$ No. 227). Group theory predicts the following phonon modes for the spinel structure

$$A_{1g}(R) + E_g(R) + T_{1g}(R) + 3T_{2g}(R) + 2A_{2u} + 2E_u + 4F_{1u}(IR) + 2F_{2u}$$

Out of these phonon modes, five are Raman active ($A_{1g} + E_g + 3T_{2g}$) and four infrared active modes ($4F_{1u}$).

## 3.3 ThermoGravimetric Analysis (TGA)

Thermogravimetric analysis is one of the methods of thermal analysis that has been developed to study the changes of material under heating effect. It consists in measuring the change in the mass of a sample when it is subjected to a temperature variation under a controlled atmosphere. This variation can be a loss of mass in the event of vapor emission or a mass gain as in the case of oxidation. This method allows us to evaluate the amount of hydroxide residues or organic matter still present in the samples as well as the temperature of their evaporation. This allows us to set the optimal calcination temperature for samples who need to be calcined.

The analyses were performed on a TGA Q500 V6.7 build 203 device at Mascir Foundation laboratory. All samples were analyzed under the following conditions:

- The mass used is between 10 and 30 mg
- The analysis atmosphere is an inert atmosphere
- The heating rate is 10°C/min
- The temperature range is between 25-600°C

## 3.4 Fourier Transform – Infrared Spectroscopy (FT-IR)

Fourier Transform Infrared Spectroscopy is based on the absorption of infrared radiation by the analyzed material. It allows through the detection of the characteristic vibrations of the chemical bonds, to perform the analysis of the chemical functions present in the sample.

When the wavelength (energy) provided by the light beam is close to the vibrational energy of the molecule, the molecule will absorb the radiation and there will be a decrease in the reflected or transmitted intensity. Therefore, a material with given chemical composition and structure will correspond to a set of characteristic absorption bands which allows identifying the material [49].


Figure 3. 3: FT-IR SPECTROMETER

The analysis is carried out at the laboratory of Mascir Foundation, using ABB Bomem FTLA2000 on KBr-dispersed sample pellets (Figure 3. 3), in order to avoid saturation of the signal, the studied powders are diluted in anhydrous KBr, transparent to infra-red radiation, in the form of pellets consisting of 150 mg of KBr and 5 mg of sample. The spectra are recorded between 400 and 4000 $cm^{-1}$ and processed using the Win-IR software.

### 3.5 Dynamic Light Scattering (DLS)

Dynamic light scattering (DLS) measurements were performed with a Malvern Instrument Zeta Zetasizer equipped with a He-Ne laser (λ= 633 nm, max 5mW) and operated at a scattering angle of 173°. All measurements were realized using a value of material RI=2.4.2 and dispersant RI=1.330. In all analyses, 1mL of particle suspensions was placed in a DTS1070 polystyrene cuvette.

### 3.6 Scanning electron microscopy (SEM)

The scanning electron microscope SEM is a device that can quickly provide information about the morphology and chemical composition of a solid material. The SEM is coupled to an Energy Dispersive Spectrometry (EDS) microanalysis system.

The surface of the sample is scanned by an accelerated electron beam at voltages generally between 10 and 30 kV, which will interact with the material (primary radiation). From these electronic interactions, many secondary radiations will be exploited with the help of appropriate detectors:

- Secondary electron emission

- Emission of backscattered electrons (without loss of energy)
- X-ray emission, etc.

The electrons (secondary and backscattered) are collected by specific detectors, with the help of synchronizing the detection (intensity) to the scanning of the incident beam. This gives an image of the surface whose contrast is a function of the type of electrons selected via the detector, of chosen acceleration voltage, and of the nature of atoms present in the sample.

Images are obtained with:

- A topographic contrast (related to the rate of electrons measured and their access to the detector) in which the tips and inclined surfaces appear brighter than the flat surfaces.
- A chemical contrast linked to the diffusion factor of the atom and therefore to its atomic number Z. In this mode of images, the more an atom is heavy, the greater the number of backscattered electrons and the more the area of the image is brilliant.

Following the interactions of the primary electron beam with the atoms of the analyzed material, photons are created (de-energizing phenomenon). The collection of these photons by a specific detector coupled to the SEM allows completing the imaging part by chemical analysis (EDS). Indeed, the energy of these photons is characteristic of the atoms that emitted them, hence the possibility of carrying out the elementary analyzes that can be qualitative (identification of the elements present in the material) or quantitative (atomic percentage and/or mass of each element). It is also possible to access to the localization of the different chemical elements within the material by the cartography.

The microstructural characterization of the samples was carried out with two types of scanning electron microscope:

The electron microscope (FEI, Quanta FEG 450) is equipped with an in-lens detector, which collects secondary electrons generated for clear topographic imaging and an EsB (Energy Selective Backscattered) detector for compositional contrast imaging, which allows for simultaneous, real-time imaging and mixing of both signals. EsB detector incorporates in filtering technology that allows a high resolution backscattered electrons imaging at low voltages, revealing image details invisible. Combined with the optional AsB (Angle selective Backscattere) detector for crystal composition and orientation imaging, the FEI Quanta FEG 450 is a dedicated nanoscale analysis tool for high-resolution imaging in conjunction with the topography of the surface, the composition, and the orientation of the crystals. In summary, the following are the main features of FEI, Quanta FEG 450 SEM:

- Detectors: In-lens SE, In-lens EsB, AsB, SE and STEM (Scanning Transmission Electron Microscope)
- Acceleration voltage from 100 V to 30 KV.
- Ultra-stable high beam current for analysis applications from 4 pA to 40 nA.
- Resolution: 1 nm at 15 kV, 1.7 nm at 1 kV, STEM: 0.8 nm at 30 kV.
- Gas injection system for load compensation
- Schottky-transmitter, trading room
- Intrinsically easy to use for high reliability in multi-operator environments
- No magnetic field at the sample level

One of the main detectors that can be significantly used withing this microscope is the STEM detector, which allows the process of capturing images of very small nanoparticles (~10 nm). The samples were prepared for the STEM analysis as follows. The hexane colloidal dispersion was submitted to an ultrasonic bath. Then, a quote was sampled and diluted with hexane. The diluted dispersion was then dropped on a carbon-coated copper grid and left to dry for the STEM observations.

This microscope belongs to the nanotechnology platform of MAScIR Foundation (Figure 3. 4).

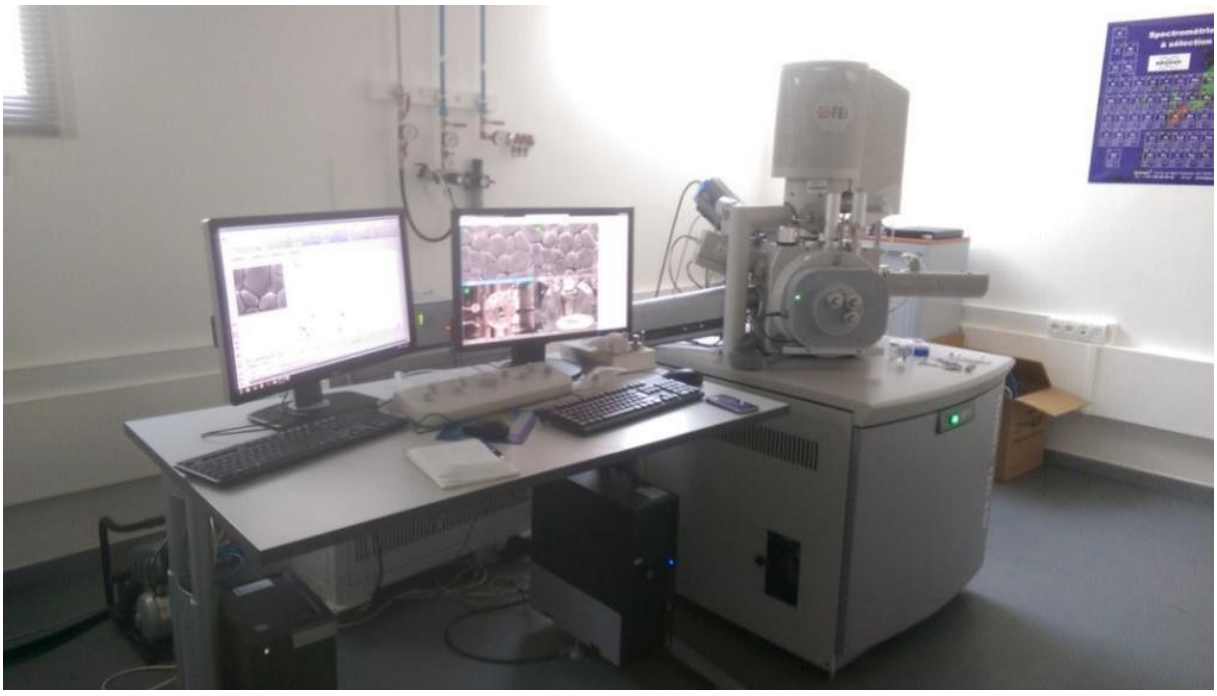

Figure 3. 4: FEI Quanta 450 FEG – Scanning Electron Microscope

The electron microscope (FE-SEM ULTRA PLUS) is equipped with the same detectors as the microscope already mentioned except the STEM detector. FE-SEM ULTRA PLUS does not

include STEM measurements. This microscope (Figure 3. 5) belongs to the Institute for Materials and Surface Technology/IMST - University of Applied Sciences, Kiel, Germany. As part of this work, we used this equipment to observe nanoparticles after putting them inside the pores of the template (Chapter V).


Figure 3. 5: FE-SEM ULTRA PLUS – Scanning Electron Microscope

### 3.7 Superconducting Quantum Interference Device (SQUID) Magnetometry

The study and optimization of the magnetic properties of ferrites constitute a large part of this thesis. Magnetic measurements were performed by SQUID to probe the magnetic properties of the prepared samples.

The Superconducting Quantum Interference Device is an integrated system for measuring and investigating the magnetic properties of matter. SQUID is a magnetic measurement device that allows the magnetic properties of natural materials (rocks, sediments, terracotta) and artificial materials (ferrofluids, carbon nanotubes, thin layers) to be determined with great accuracy over a wide range of temperatures and external magnetic fields (Figure 3. 6). The measurements obtained by this system give information about the magnetic reaction of the material subjected to magnetic fields and make it possible to characterize the magnetic properties of this material which are very dependent on the measurement conditions.

Figure 3. 6: Superconducting Quantum Interference Device (SQUID) Magnetometry

The principle of this measurement is based on the displacement of the sample within a set of superconducting detection coil. During the movement of the sample through the coils at a given temperature and magnetic field, the magnetic moment of the sample induces an electric current in the sensing coils. Any change of this current in the detection circuit induces a change of magnetic flux; therefore, by moving the sample on either side of the detection coils, the magnetic flux is integrated. A flux transformer is used to transmit the signal to the SQUID.

Magnetic measurements using the SQUID can either be field dependent or temperature dependent. The field dependent measurement of a magnetic sample is carried out at a constant temperature to get the saturation magnetization (Ms). Temperature dependent measurements are performed under a constant field - zero field cooled (ZFC) and field cooled (FC). In ZFC measurements, the sample is cooled from room temperature to 10 K, in a zero dc-field. Then a small magnetic field of about 200 Oe is applied and the magnetization is recorded on warming whilst in FC measurements, the sample is cooled from room temperature under an applied magnetic field. These measurements were carried out at the nanotechnology platform of MAScIR Foundation.

The main elements constituting this magnetometer are:

- A superconducting solenoid to generate an intense magnetic field
- A superconducting coil of magnetic induction detection which is located inside and in the center of the magnet
- A SQUID connected to the detector coil (for measuring the magnetization)
- A temperature control system

This magnetometer can measure extremely low magnetic moments in the order of $10^{-8}$ emu.g$^{-1}$ by applying a magnetic field in a wide range (up to 6 T) and for temperatures ranging from 5 K to 300 K.

### 3.8 Conclusion

In this chapter, we have described different techniques used in this work. Some detailed information of the characterization methods were subsequently exposed ranging from thermal and structural analyzes followed by spectroscopic measurements and electron microscopy imaging to superconducting quantum interference device for magnetic properties measurements.

# 4 Synthesis and characterization of $CoFe_2O_4$ nanoparticles

## 4.1 Introduction

Magnetic metal oxide nanoparticles (NPs) have attracted a great interest due to their physical and magnetic properties, which vary dramatically from their bulk counterparts because of their high surface/volume ratio and their size comparable to the magnetic domain [50]. Such nanostructures were found to be promising for extensive applications in several fields including magnetic recording media, spintronics, magnetic resonance imaging (MRI), catalysis, magnetically controlled drug delivery, sensors, etc [51][52][53]. Iron-cobalt based nanoparticles, and especially cobalt ferrite ($CoFe_2O_4$), becomes very attractive for a variety of applications in electronic devices, catalysis, ferrofluids, high-density information storage, magnetic recording (high-density digital recording disks) and biomedical applications, owing to their high physical and chemical stability, high magnetocrystalline anisotropy, moderate saturation magnetization and a large magnetostriction coefficient [54][55][56][57].

In order to synthesize cobalt ferrite nanoparticles, several methods have been developed including microemulsion, sol-gel, microwave, and co-precipitation methods [58][59], but the thermal decomposition of metal complexes in the presence of ligand (as capping agent) appears currently to be the most promising to ensure the control of nanoparticles size, shape and composition [60][61]. In addition, nanoparticles synthesized by this method are coated by an organic layer of ligands, which ensure their good colloidal stability in organic solvents.

When I arrived at the MAScIR Foundation, this process was not developed yet in the laboratory. Therefore, my first aim was to appropriate such method and develop an appropriate synthesis protocol for cobalt ferrite nanoparticles.

In our study, the objective was to obtain nanoparticles with small diameters (i.e. between 5 and 20 nm) likely able to be incorporated in a porous alumina membranes. Among the various works described in the synthesis of these nanoparticles [62][63][47], we have selected that reported by Song et al [26] which leads to $CoFe_2O_4$ nanoparticles of spherical shape and uniform size in the range that we want to obtain. Recall that the principle of synthesis is based on the thermal decomposition of iron and cobalt acetylacetonates in an organic solvent (Benzyl ether) having a high boiling point (298 ° C), in the presence of a reducing agents (oleylamine and oleic acid).

The volume ratio Oleylamine (oleic acid) / Benzyl ether has been modified to study its influence on the size of the nanoparticles.

In the remainder of this manuscript, we give details of the synthesis protocol developed for $CoFe_2O_4$ nanoparticles. Thereafter, we expose the chemical and magnetic characterizations carried out on various synthesized $CoFe_2O_4$ nanoparticles obtained by varying different parameters. We notice herein that the modification of the synthesis parameters allowed us to understand the role of each one on the size, monodispersity, and morphology of nanoparticles as we will see in the following sections.

### 4.2 Synthesis of cobalt ferrite NPs

The thermal decomposition process is a thermal decomposition of acetylacetonate complexes consisting of transition metal and acetylacetonate ligands ($C_5H_7O^{2-}$) at high temperature in presence of oleic acid and oleylamine, surfactants which stabilize the nanoparticles in an organic solvent (Hexane) at the end of the synthesis. The synthesis is carried out in the presence of hexadecanediol which makes it possible to initiate the reaction by promoting the decomposition of acetylacetonate precursors. The solvent used is benzylether because its boiling point (298 °C) is higher than that of precursors. The reaction is carried out by maintaining the solution at the reflux temperature of the solvent at various times up to 120 min and under oxygen-free conditions in a Schlenk line. The equation of the thermal decomposition reaction is as follows:

$$Co(C5H7O2)2 + Fe(C5H7O2)3 \rightarrow CoFe2O4 + CH3COCH3 + CO2$$

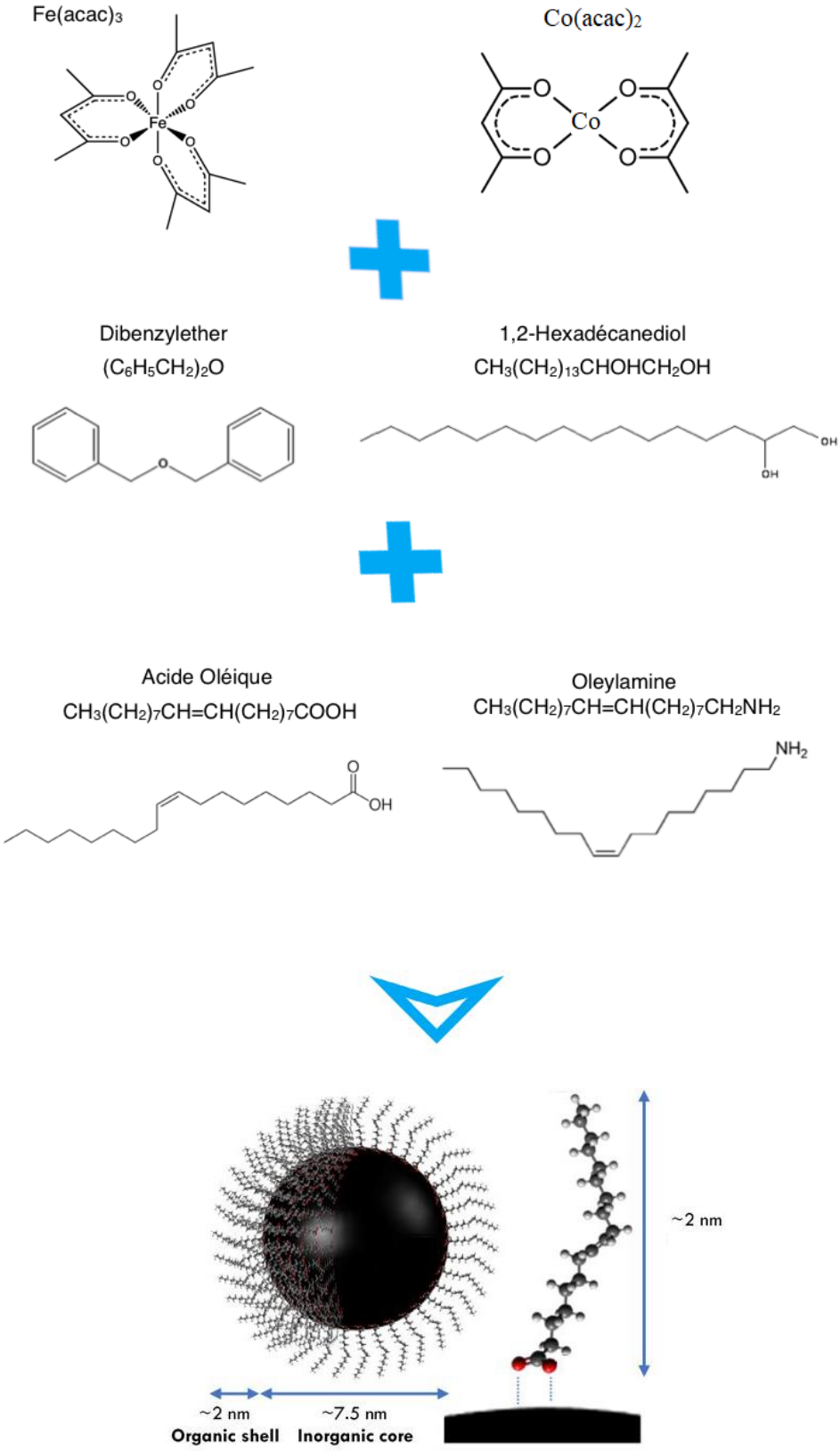


Figure 4. 1: Formulas of reagents used in the thermal decomposition process

This method of synthesis has been chosen because it makes it possible to obtain spherical and monodisperse nanoparticles stabilized in an organic solvent [46]. The size and shape of the

particles obtained depend on different parameters such as the amount of precursors, the temperature or the duration of the heat treatment [26]. They also depend on the ratios of oleic acid to oleylamine, and the presence or absence of hexadecanediol.

- Chemicals

The synthesis was carried out using commercially available reagents. The starting Precursors were iron (III) acetylacetonate ($Fe(acac)_3$, 99.99%), and cobalt (II) acetylacetonate ($Co(acac)_2$, 99%). The used solvents were Benzyl ether (98%, boiling point: 298 °C), absolute ethanol (100%), and hexane (98.5%). For the surfactants and reductant we used oleic acid (90%, boiling point: 360 °C), oleylamine (70%, boiling point: 350 °C), and 1,2-hexadecanediol (90%). All the chemicals were purchased from Sigma-Aldrich Ltd. and were used as received without further purification.
Carcinogenic, mutagenic, reprotoxic (CMR) substances were handled with gloves and under a fume hood.

- Protocol of synthesis

In a typical synthesis named in the text as "standard protocol", into 100 mL three-necked flask under nitrogen flow, we placed 4 mmol of Fe(III) acetylacetonate, 2 mmol of Co(II) acetylacetonate, 20 mmol of 1,2-hexadecanediol, 12 mmol of oleic acid, 12 mmol of oleylamine, and 40 ml of benzyl ether. That is to say in proportions five times higher for the hexadecanediol compared to the Fe(III) acetylacetonate and six times higher for the surfactants (oleic acid and oleylamine) compared to the Fe(III) acetylacetonate.

Thermal controlling is carried out using a thermocouple probe to control the temperature and the duration of heat treatment. The reaction mixture was magnetically stirred and de-gassed at room temperature for 60 min, then was heated and kept at 100 °C for 30 min to remove water. Subsequently, the temperature was increased and kept at 200 °C for another 30 min. Then, the mixture was heated to reflux and kept to the desired temperature (300°C) for 60 min. The final mixture was cooled to room temperature by removing the heat source, and purified three times with ethanol and hexane: 40 ml of absolute ethanol were added to precipitate the nanoparticles from the supernatant, the supernatant was discarded after centrifugation at 10000 rpm (for 30 min). The as-obtained nanoparticles were dispersed in 20 ml of hexane, this washing process was repeated three times. A black magnetic precipitate was obtained after magnetic settling. The precipitate was dispersed in 20 ml of hexane and a ferrofluid composed of surfaced $CoFe_2O_4$ nanoparticles was obtained. Figure 4.2 illustrates the thermal decomposition process.

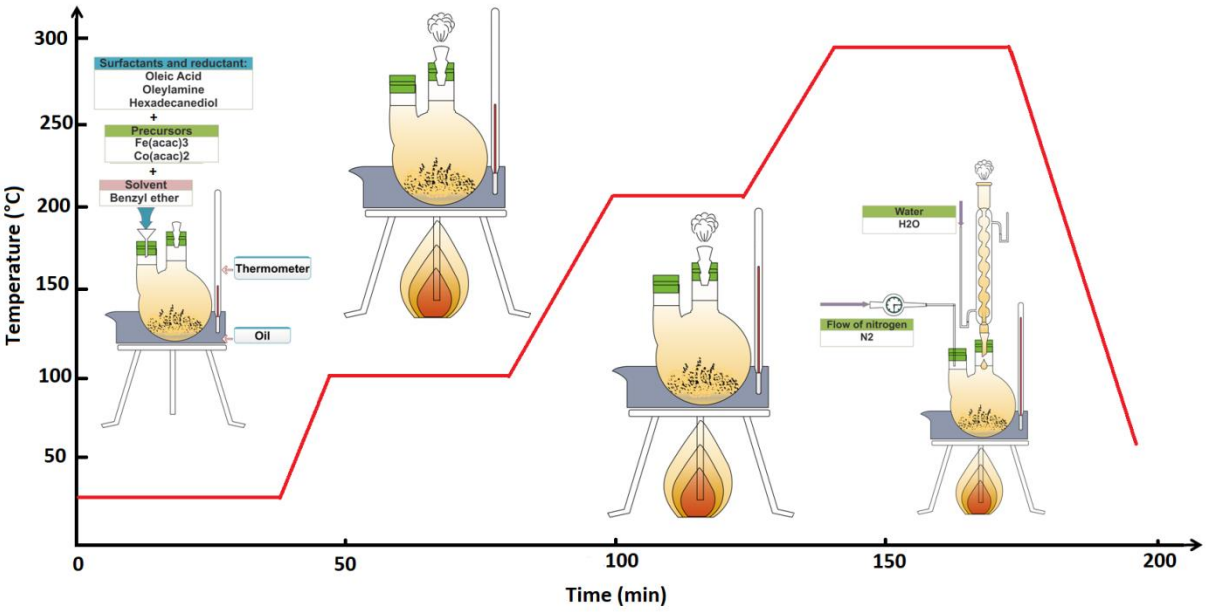


Figure 4. 2: Illustration of the thermal decomposition method

## 4.3 Chemical composition

The chemical composition of the synthesized sample was studied by energy dispersive X-ray spectroscopy (EDS) microanalysis. The sample was analyzed five times on different areas (Figure 4.3: A1, A2, A3, A4, and A5) and the chemical formula was calculated by assuming the absence of anions vacancies. The EDS results were summarized in Table 4. 1.

| Areas | chemical formula |
|---|---|
| A1 | $Co_{1.01}Fe_{1.93}O_{4.04}$ |
| A2 | $Co_{0.99}Fe_{1.96}O_{4.04}$ |
| A3 | $Co_{1.03}Fe_{2.02}O_{3.94}$ |
| A4 | $Co_{0.98}Fe_{1.93}O_{4.07}$ |
| A5 | $Co_{0.95}Fe_{1.87}O_{4.17}$ |

Table 4. 1: Concluded chemical composition obtained from EDS measurement on different areas of the sample.

According to table 4. 1, the concluded chemical formulas from EDS measurements are very close to the theoretical formula of spinel ferrite. The atomic ratio cobalt to iron is very close to 2:1, in agreement with the expected stoichiometry. The below results confirmed that the prepared material is $CoFe_2O_4$, without any impurities. EDS analysis was carried out at a number of different positions on the ferrite sample as shown in figure 4.3. EDS results from different positions were consistent within error, confirming the compositional uniformity of the materials.

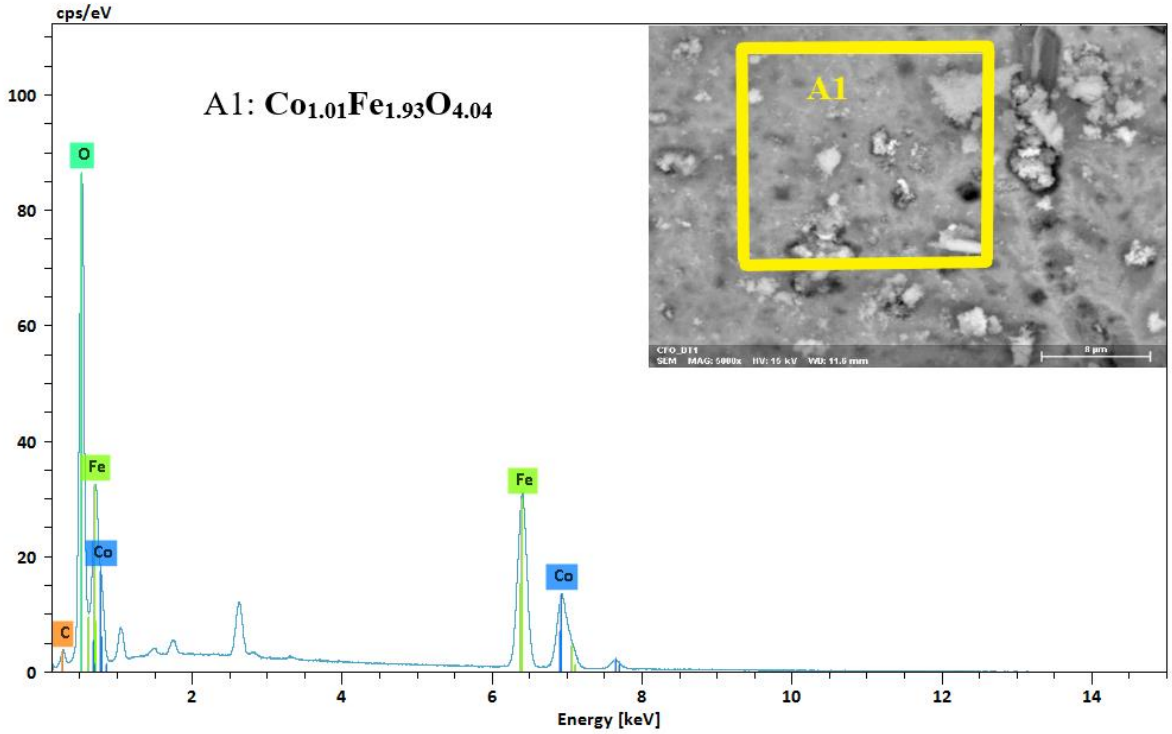


| Element | Line s. | Mass [%] | Mass Norm[%] | Atom [%] |
|---|---|---|---|---|
| Carbon | K-Serie | 0.00 | 0.00 | 0.00 |
| Oxygen | K-Serie | 27.52 | 27.83 | 57.84 |
| Iron | K-Serie | 45.97 | 46.50 | 27.68 |
| Cobalt | K-Serie | 25.37 | 25.67 | 14.48 |
| | | 98.86 | 100.00 | 100.00 |

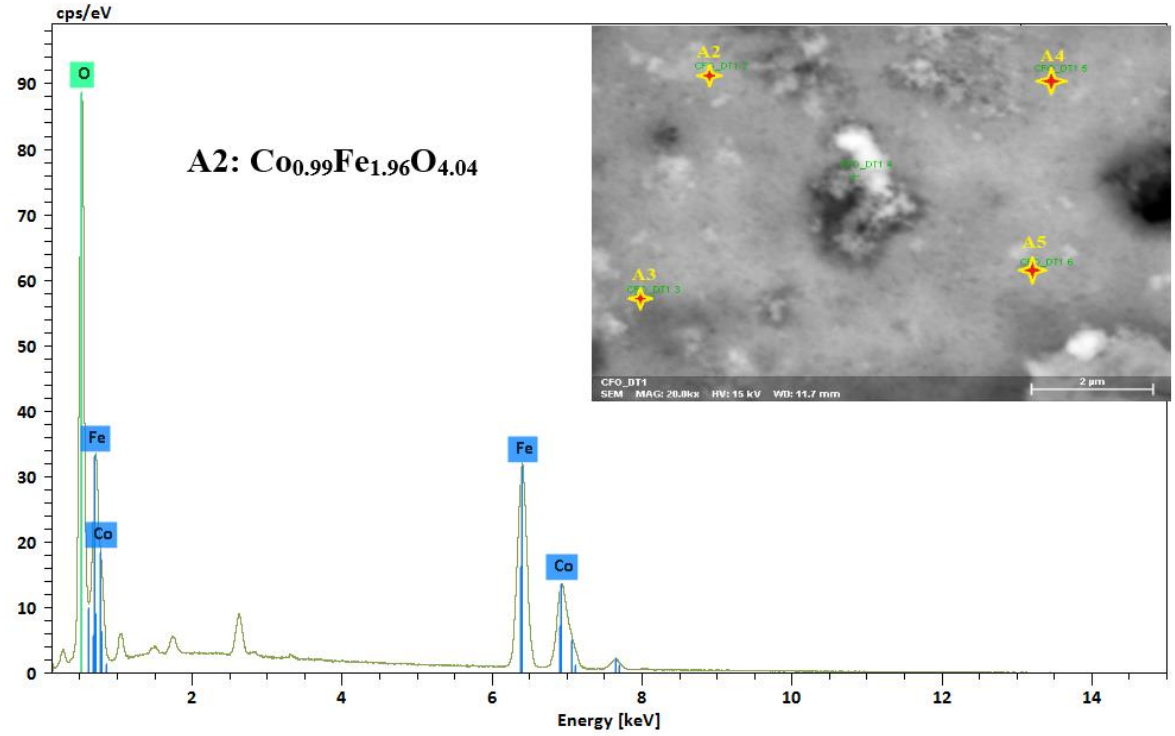


| Element | Line s. | Mass [%] | Mass Norm[%] | Atom [%] |
|---|---|---|---|---|

| | | | | |
|---|---|---|---|---|
| Carbon | K-Serie | 0.00 | 0.00 | 0.00 |
| Oxygen | K-Serie | 27.65 | 27.79 | 57.78 |
| Iron | K-Serie | 46.86 | 47.10 | 28.05 |
| Cobalt | K-Serie | 24.99 | 25.11 | 14.17 |
| | | 99.50 | 100.00 | 100.00 |

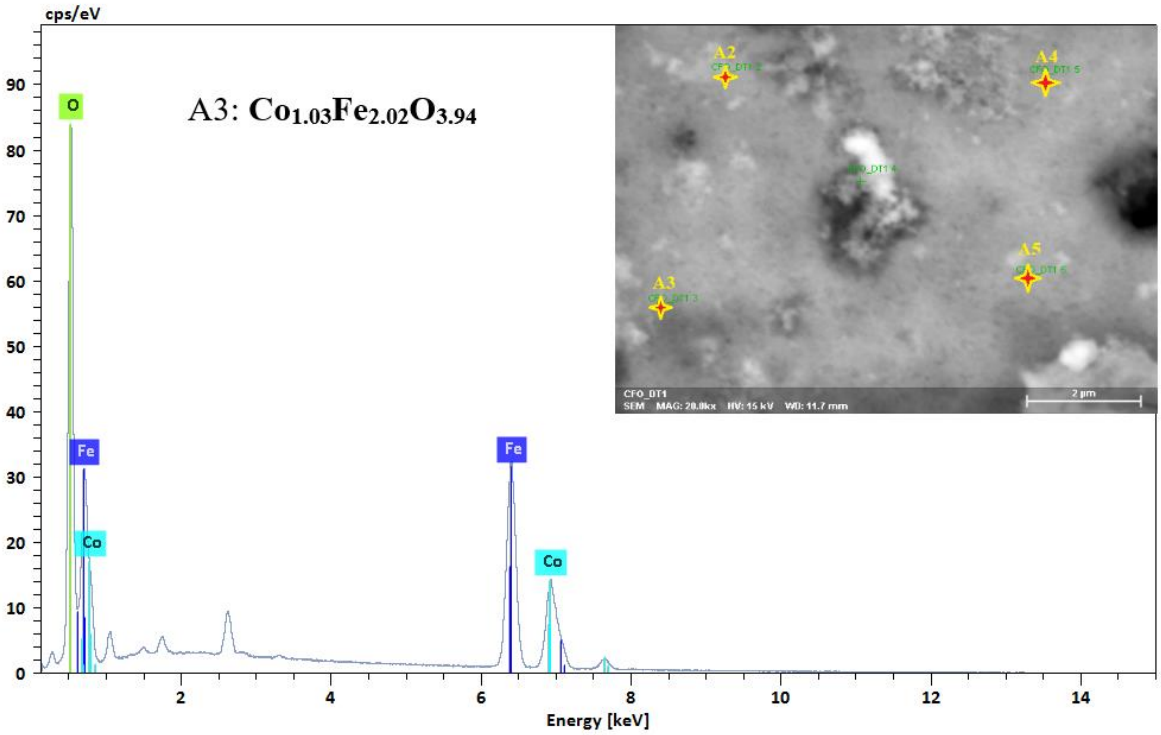


| Element | Line s. | Mass [%] | Mass Norm[%] | Atom [%] |
|---|---|---|---|---|
| Carbon | K-Serie | 0.00 | 0.00 | 0.00 |
| Oxygen | K-Serie | 26.40 | 26.62 | 56.33 |
| Iron | K-Serie | 47.29 | 47.67 | 28.90 |
| Cobalt | K-Serie | 25.50 | 25.71 | 14.77 |
| | | 99.19 | 100.00 | 100.00 |

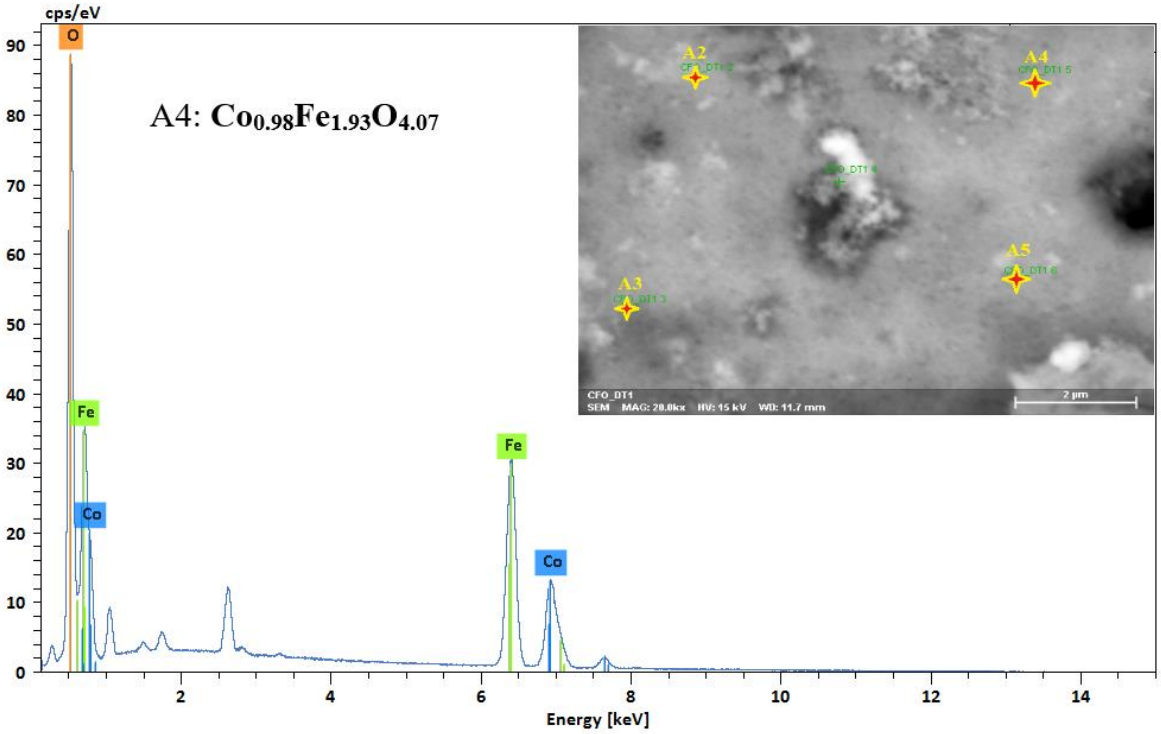


| Element | Line s. | Mass [%] | Mass Norm[%] | Atom [%] |
|---|---|---|---|---|
| Carbon | K-Serie | 0.00 | 0.00 | 0.00 |
| Oxygen | K-Serie | 28.06 | 28.21 | 58.28 |
| Iron | K-Serie | 46.46 | 46.71 | 27.65 |
| Cobalt | K-Serie | 24.95 | 25.09 | 14.07 |
| | | 99.47 | 100.00 | 100.00 |

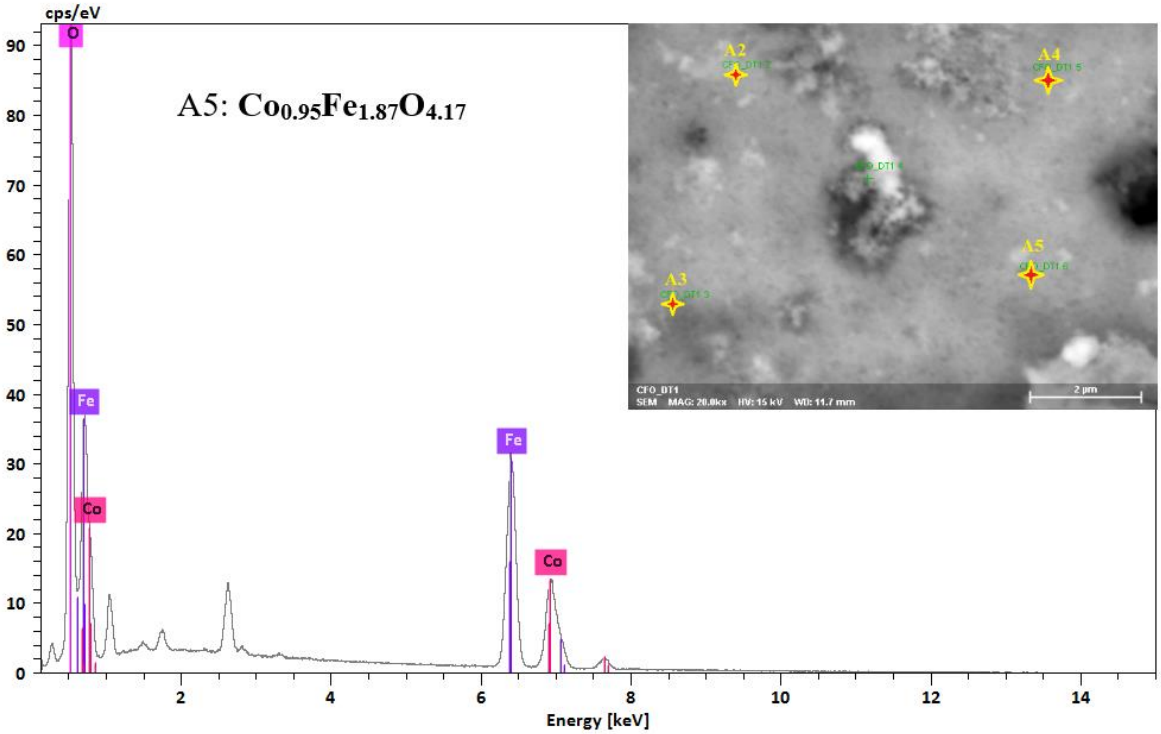


| Element | Line s. | Mass [%] | Mass Norm[%] | Atom [%] |
|---|---|---|---|---|

| | | | | |
|---|---|---|---|---|
| Carbon | K-Serie | 0.00 | 0.00 | 0.00 |
| Oxygen | K-Serie | 28.99 | 29.34 | 59.62 |
| Iron | K-Serie | 45.38 | 45.92 | 26.73 |
| Cobalt | K-Serie | 24.45 | 24.74 | 13.65 |
| | | 98.82 | 100.00 | 100.00 |

Figure 4. 3: EDS analysis of synthesized cobalt ferrite nanoparticles in five different areas.

## 4.4 Microstructure and Morphology

### 4.4.1 X-Ray Diffraction (XRD)

In order to verify the spinel structure and estimate the particle size, X-ray diffraction measurement was carried out. The X-ray diffraction pattern of the synthesized $CoFe_2O_4$ (Figure 4. 4) shows that the obtained diffraction peaks correspond well to the spinel structure (JCPDS No. 04-016-3954) with face centered cubic phase. The cobalt ferrite sample displayed several relatively strong and well defined reflection peaks in the $2\theta$ region of 10–100°, and the positions and relative intensities of all detectable peaks matched well with those from the standard JCPDS patterns (as shown in Figure 4.4) indicating that the resulting material has a pure spinel ferrite structure. Traces of any other phases, kind of detectable impurities or intermediate phase were not observed. The diffraction peaks corresponding to the (111), (220), (311), (222), (400), (422), (511), (440), (533), (622), (642), (731) and (800) reflections provided clear evidence for the cubic spinel structure (space group: Fd3m), confirming the crystallization of the standard ferrite. The prominent diffraction peaks in the XRD pattern of the synthesized cobalt ferrite nanoparticles revealed their high crystallinity. The Bragg reflection pattern showed slightly broad peaks, indicating the fine grain size of the constituent ferrite nanoparticles.

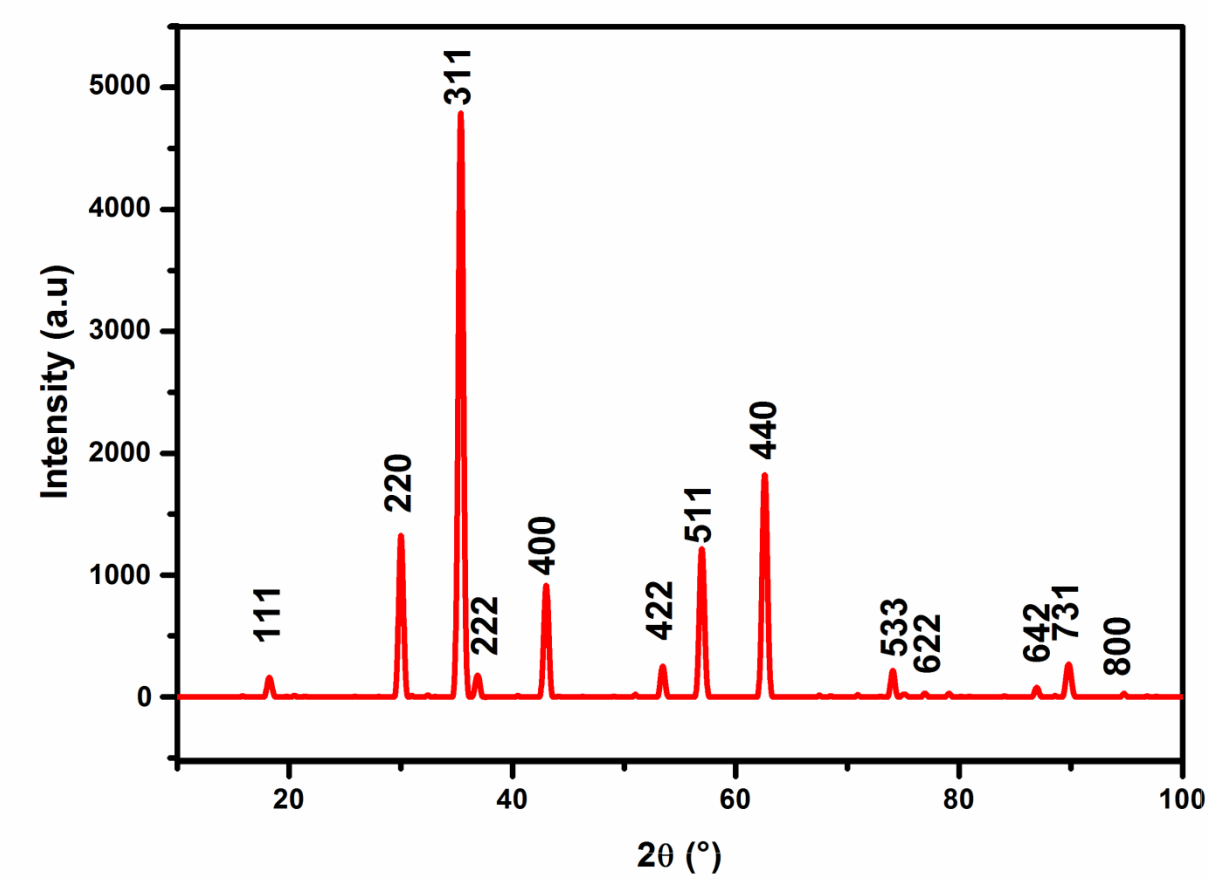


Figure 4. 4: X-ray diffraction pattern of the synthesized $CoFe_2O_4$ nanoparticles.

The broad diffraction peaks obtained are expected for such small crystalline domains. The Scherrer's formula allows estimating the crystallite size by taking the full width at half maximum (FWHM) of the main diffraction peak (311).

$$D = \frac{0.9\lambda}{\beta cos(\theta)} \tag{1.18}$$

Where λ is the X-ray wavelength, β is the broadening at half the maximum intensity (FWHM) of the hkl peak (in our case the 311 peak) and θ is the Bragg angle of this peak. The average crystallite size estimated is 11.2 nm.

The results obtained by X-ray diffraction on the $CoFe_2O_4$ nanoparticles will be compared with those obtained with other characterization techniques such as Raman spectroscopy, Infrared Spectroscopy, and Scanning transmission electron microscopy.

### 4.4.2 Raman spectroscopy

To provide further information about the structure of $CoFe_2O_4$ nanoparticles, the sample was characterized by Raman spectroscopy, the corresponding Raman spectra measured at room

temperature are shown in figure 4.5. The vibration modes characteristic of pure $CoFe_2O_4$ structure were clearly observed, without additional or intermediate phase peaks [64][65][66]. Since the $CoFe_2O_4$ cubic spinel space group belongs to the Fd3m, the typical $A_{1g}+3T_{2g}+E_g$ mode in Raman peaks can be clearly identified. Namely, the five main peaks at 215, 287, 455, 596, and 676 $cm^{-1}$, correspond to the $T_{2g}(3)$, $E_g$, $T_{2g}(2)$, $T_{2g}(1)$, and $A_{1g}$ modes, respectively [66]. Nevertheless, the modes below 200 $cm^{-1}$ were not recorded due to the equipment limitation. Noting that other active mode such as the soft-mode $A_{1g}$ could be clearly distinguished.

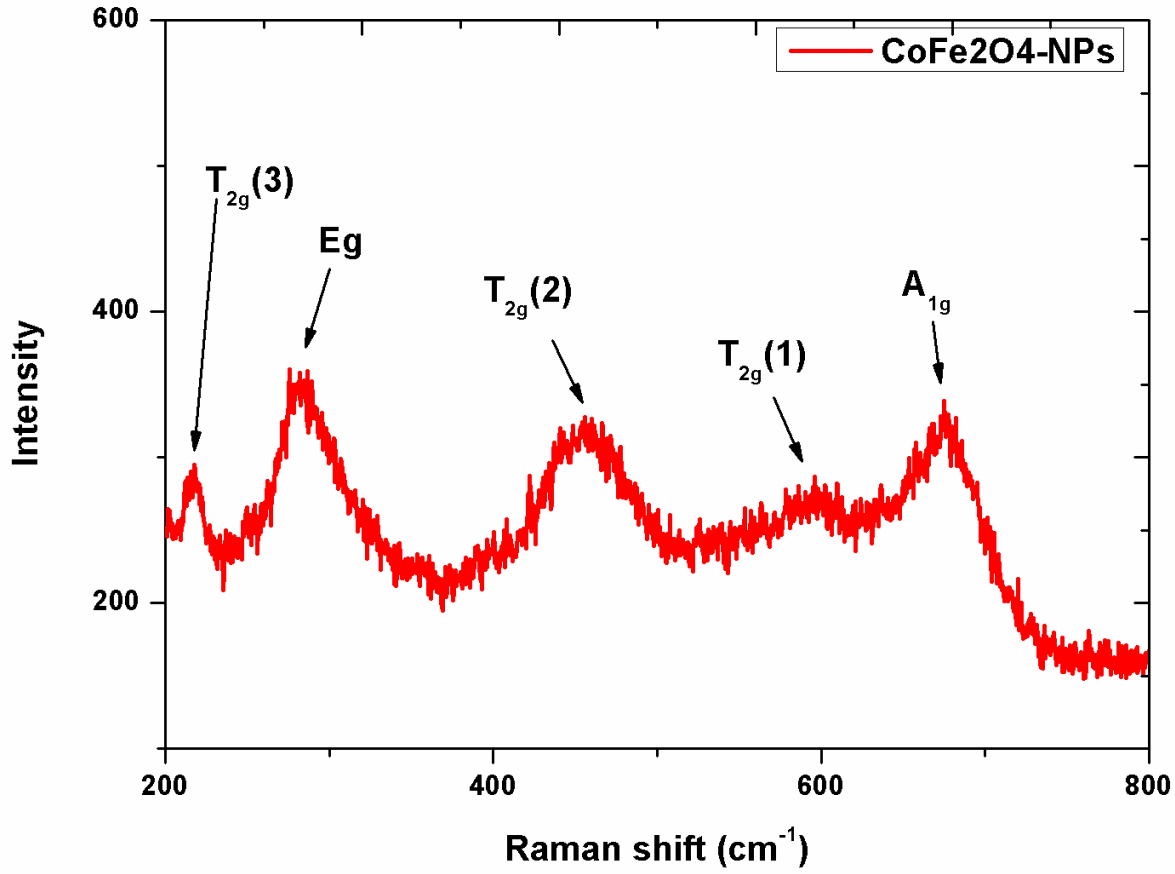


Figure 4. 5: Raman spectra in the 200−800 $cm^{-1}$ range for spinel $CoFe_2O_4$.

### 4.4.3 Fourier Transform - Infrared Spectroscopy (FT-IR)

Complementary vibrational information could be obtained using Fourier Transform Infrared Spectroscopy (FT-IR). With such a technique, it is possible to obtain further information about the structure of nanoparticles from the vibration modes of the bonds present in the ferrite structure and the surface organic layer.

Figure 4.6 shows the FT-IR spectra of the synthesized $CoFe_2O_4$ nanoparticles between 4000 and 400 $cm^{-1}$. Globally, three distinct zones can be distinguished, vibrational modes correspond to a hydrocarbon chain, carboxylate groups, and metal-oxygen (M-O) bonds.

We interest in the first at the zone corresponds to vibrational modes of metal-oxygen bonds for spinel structure. The description of the other bands will be given in the section dedicated to the characterization of the organic layer.

As shown in figure 4.6, the principal vibrational modes of metal-oxygen (M-O) bonds are present between 300 and 670 $cm^{-1}$ that correspond to metals in a tetrahedral or octahedral configuration for spinel structures. In general, M-O bonds in the octahedral sites appear at 380-450 $cm^{-1}$, whereas they are around 540-600 $cm^{-1}$ for tetrahedral sites. In our case, a band of M-O bonds in the octahedral sites appear at 400 $cm^{-1}$, in contrast, the band of M-O bonds in the tetrahedral sites appears at 591 $cm^{-1}$.

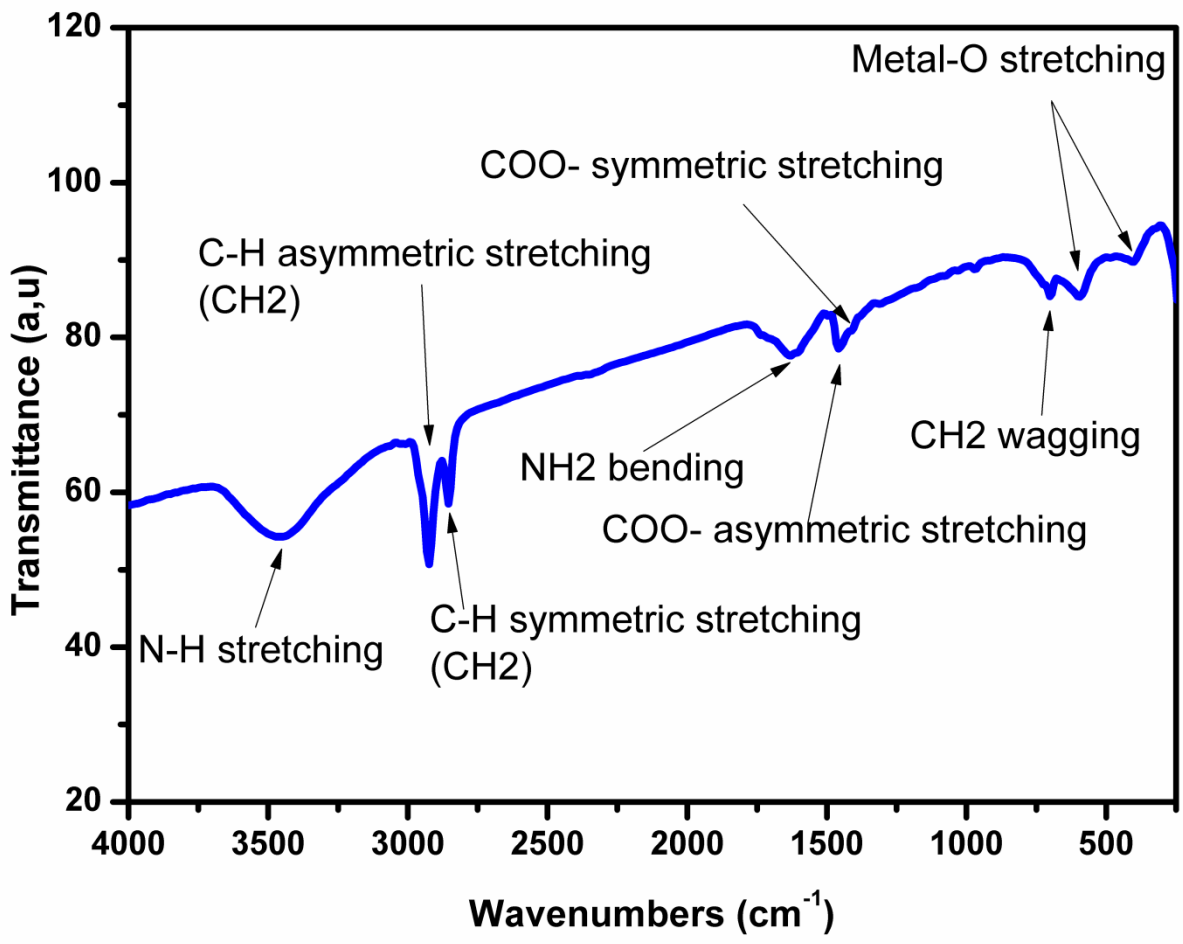


Figure 4. 6: Infrared spectrum of the synthesized $CoFe_2O_4$ nanoparticles.

### 4.4.4 Scanning transmission electron microscopy (STEM)

The photomicrographs taken by scanning transmission electron microscope (STEM) of the $CoFe_2O_4$ nanoparticles are shown in Figure 4.7. The nanoparticles are imaged at different magnitudes and the diameter of the nanoparticles is measured using image processing software (ImageJ). The size distribution is calculated on a large number of nanoparticles (around 550 NPs) considering all particles without distinctions. In particular, during the preparation of the STEM grid, the nanoparticles tend to spontaneously self-assembled and a phenomenon of segregation of the size can be observed with the smallest particles that are rejected at the edge of the assembly. Noting that the set of nanoparticles is considered for the size distribution, not just the center of the assembly, which would have the effect of artificially reducing the size distribution. Figure 4.7 shows the STEM images and particle size distributions.

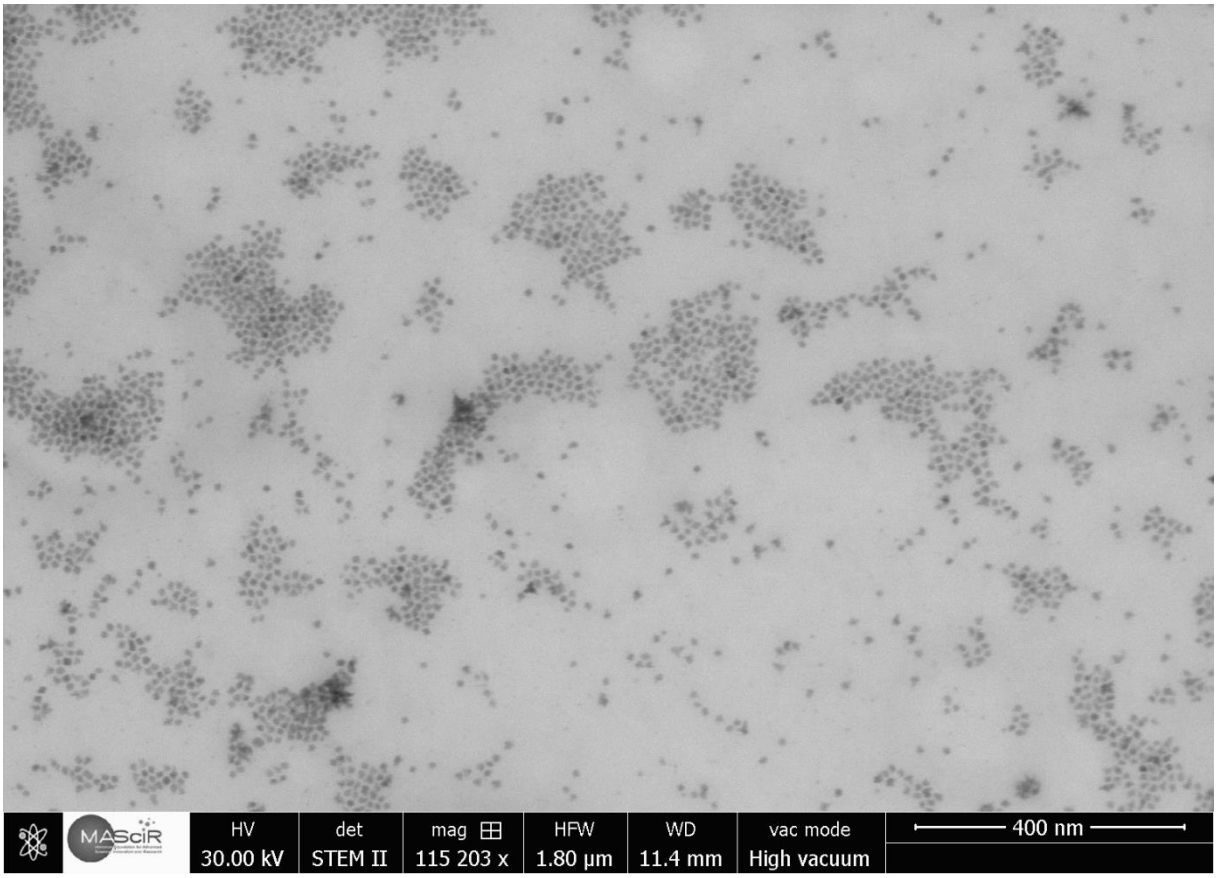

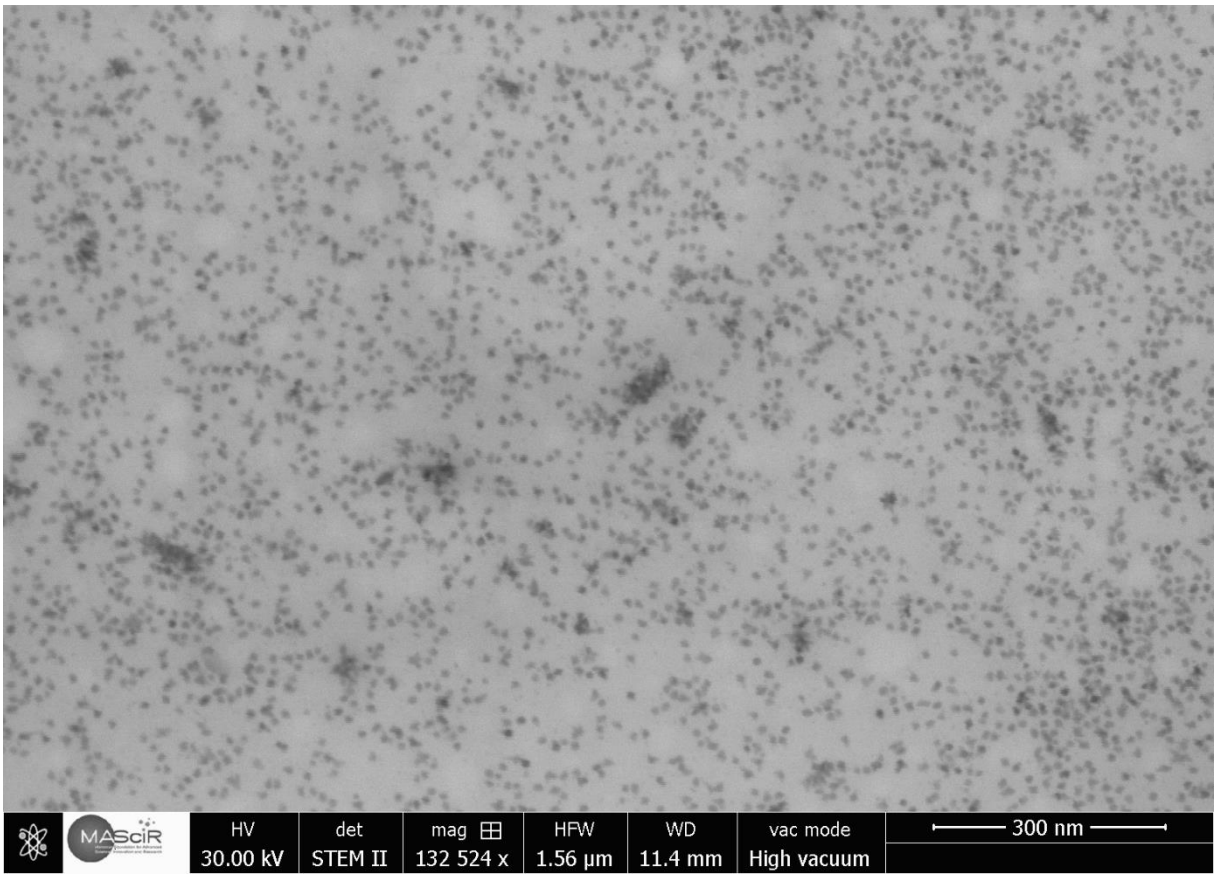
HV
30.00 kV
det
STEM II
mag
132 524 x
HFW
1.56 µm
WD
11.4 mm
vac mode
High vacuum
300 nm

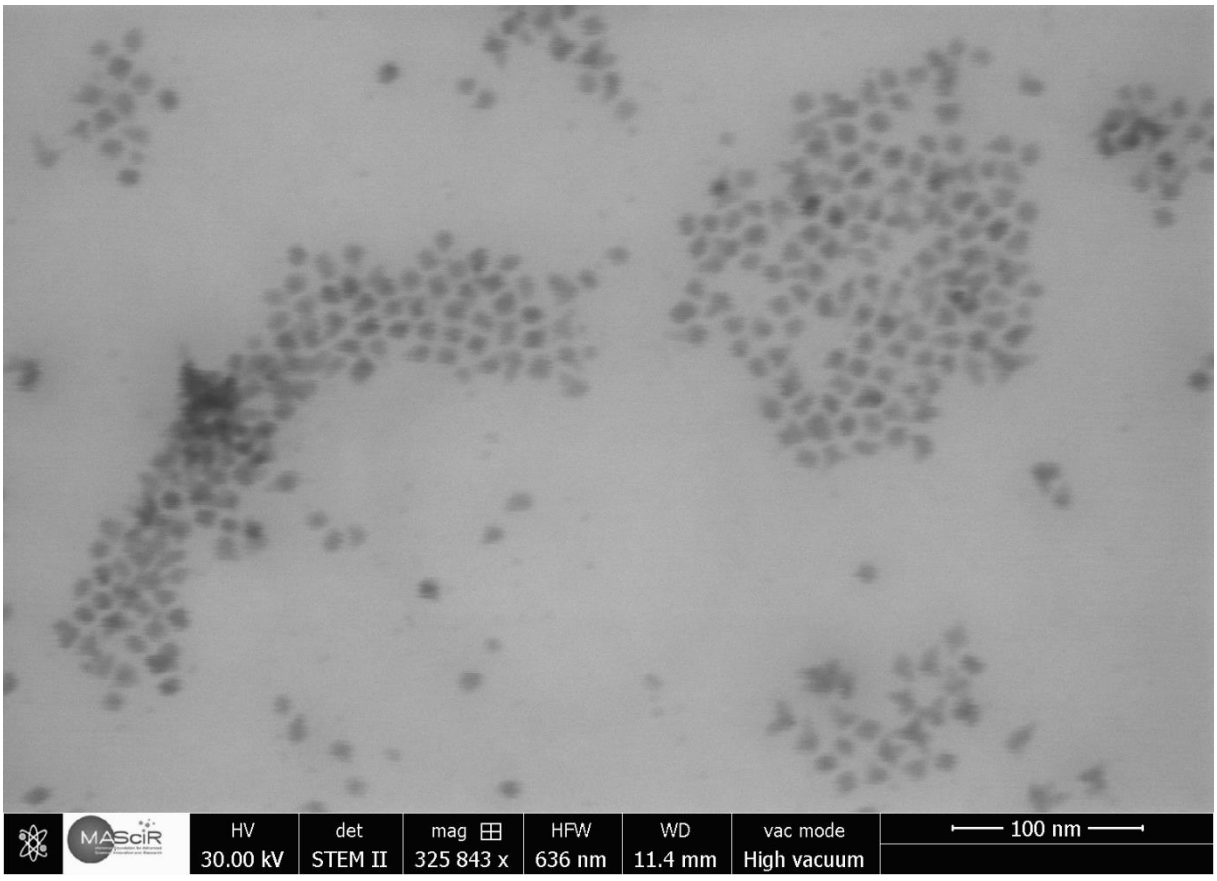
HV
30.00 kV
det
STEM II
mag
325 843 x
HFW
636 nm
WD
11.4 mm
vac mode
High vacuum
100 nm

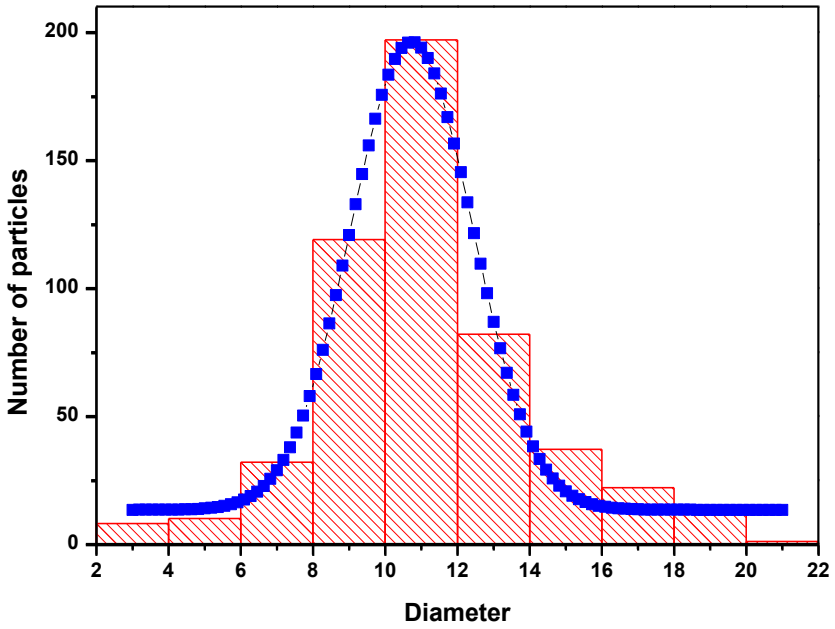


Figure 4. 7: STEM images of synthesized $CoFe_2O_4$ at different magnitudes and their size distribution histogram.

According to the images obtained by STEM (Figure 4.7), the synthesized $CoFe_2O_4$ nanoparticles are spherical and highly monodispersed. The statistical analysis by ImageJ software (macro particle size analyzer), allowed to obtain the histogram giving rise the information about the size distribution of the nanoparticles. We can deduct from the histogram that the average diameter of nanoparticles is around 10.7 nm.

It is worth noting that the mean size calculated from STEM images is in good agreement with that estimated one from XRD. This agreement supports that these nanoparticles are single crystals. The slight difference observed between the two techniques could be explained by the fact that for XRD only the largest particles are counted, whereas in STEM, the size distribution with an average diameter is obtained on a limited number of particles (around 550 NPs).

For the application of $CoFe_2O_4$ nanoparticles, it is important to get these nanoparticles suspended in an organic solution (Hexane in our case) with a narrow size distribution. Dynamic Light Scattering (DLS) is used to measure the hydrodynamic diameter of suspended particles. The size distribution measured by STEM is a number distribution because the number of nanoparticles with a given size is counted. In order to compare these two distributions, we have represented the size distribution by DLS measured number. In addition, we also gave the

volume distribution because it is the most often used in the literature and which is the most representative of the sample. Size distributions of $CoFe_2O_4$ nanoparticles in Hexane measured by DLS are shown in Figure 4.8.

| | Diam (nm) | % Number | Width (nm) |
|---|---|---|---|
| **Peak 1:** | **10.70** | **100.0** | **3.282** |
| **Peak 2:** | **0.00** | **0.0** | **0.0** |

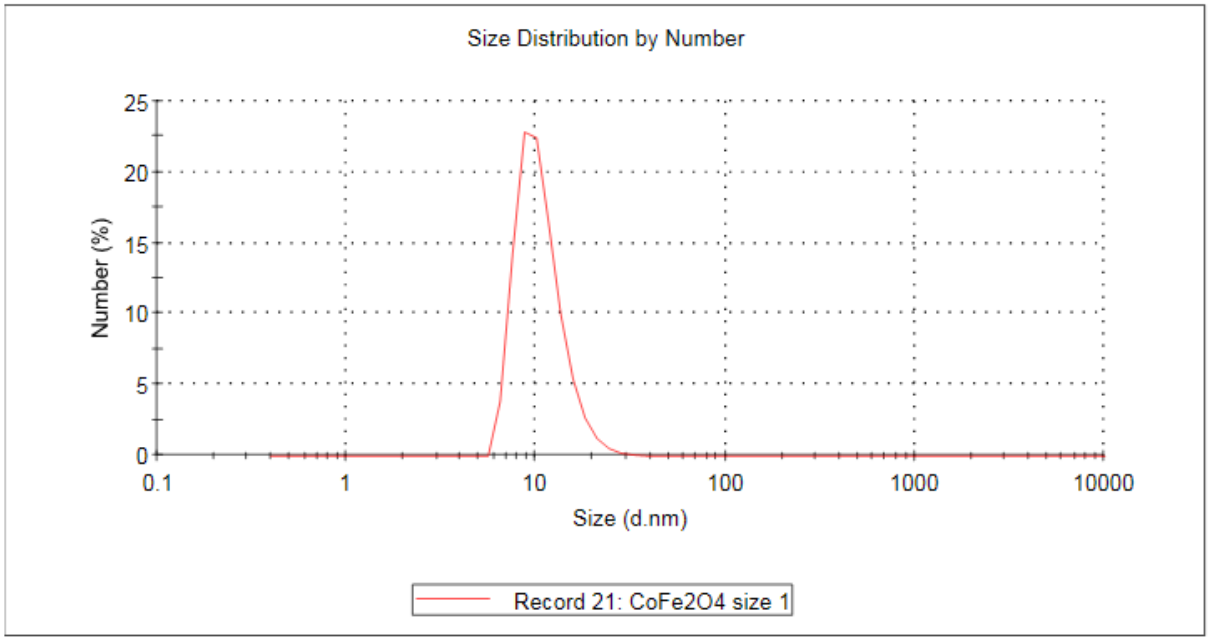


| | Diam (nm) | % Volume | Width (nm) |
|---|---|---|---|
| **Peak 1:** | **14.75** | **100.0** | **6.75** |
| **Peak 2:** | **0.00** | **0.0** | **0.0** |

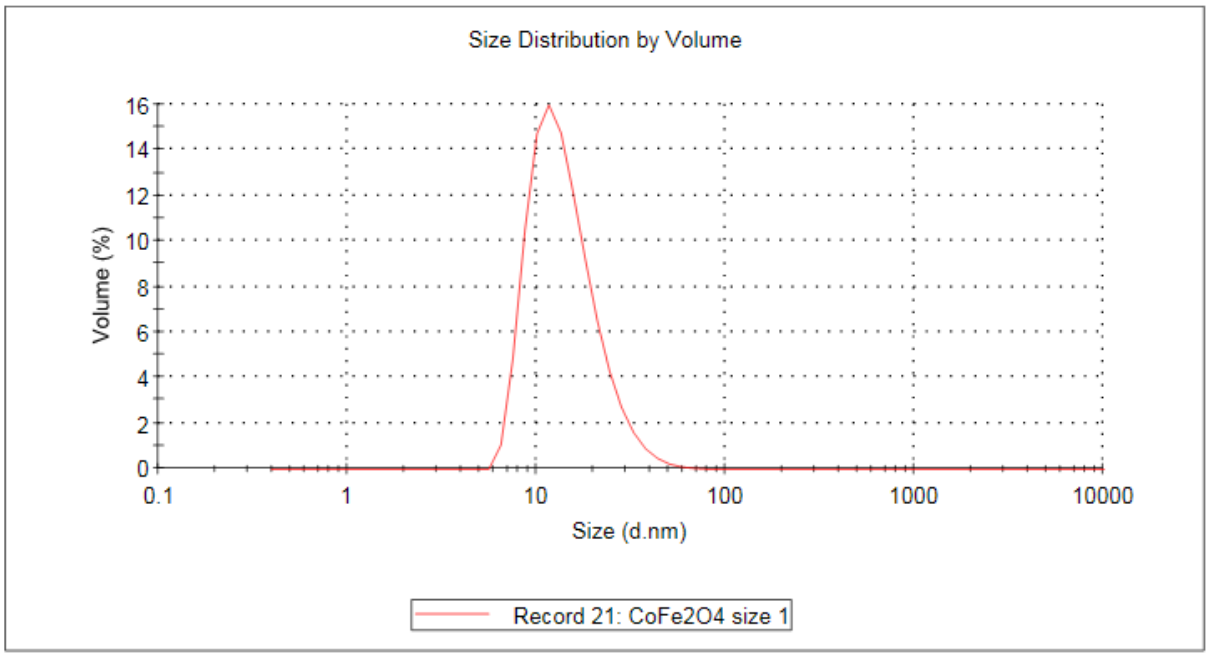

Figure 4. 8: Size distribution by number (Top) and size distribution by volume (Bottom) measured by DLS.

The average diameter measured by DLS according to the size distribution by number is equal to that measured in STEM which is 10.7 nm. The presence of aggregates is rather detected during the representation of size distribution by volume. As can be seen in Figure 4. 8, the size distribution by volume is slightly different compared to size distribution by the number which suggests the presence of a few suspended aggregates, but it remains relatively narrow. Thus, the quality of suspension is very good.

It is interesting to mention that thermal decomposition of iron and cobalt acetylacetonate in the presence of oleic acid has made it possible to obtain monodispersed and suspended nanoparticles. The nanoparticles have spherical morphology with narrow size distributions. The next section will focus on the characterization of the organic layer on the surface of nanoparticles.

## 4.5 Characterization of the organic layer on the surface of nanoparticles

### 4.5.1 Fourier Transform - Infrared Spectroscopy (FT-IR)

Figure 4. 9 represents the FT-IR analysis which allows to identify the presence of functional groups of organic molecules surrounding nanoparticles as well as the vibrational modes of metal-oxygen bonds of the spinel structure. The absorption bands observed in the range 670-3700 $cm^{-1}$ correspond to the vibration bands of the surfactant groups. The bands at 2924 and 2851 $cm^{-1}$ can be assigned to the asymmetrical and symmetrical stretching of $CH_2$ groups, characteristic of the hydrocarbon chain of the used surfactants. Two bands at 1453 and 1408 $cm^{-1}$ are observed and correspond to the asymmetric and symmetric elongations of the carboxylate groups ($COO^-$ stretching). In addition, vibrational modes observed at 3440 and 1611 $cm^{-1}$ correspond to the angular deformations of the amine groups (NH stretching and $NH_2$ bending, respectively), another band appearing at 702 $cm^{-1}$ correspond to $CH_2$ wagging.

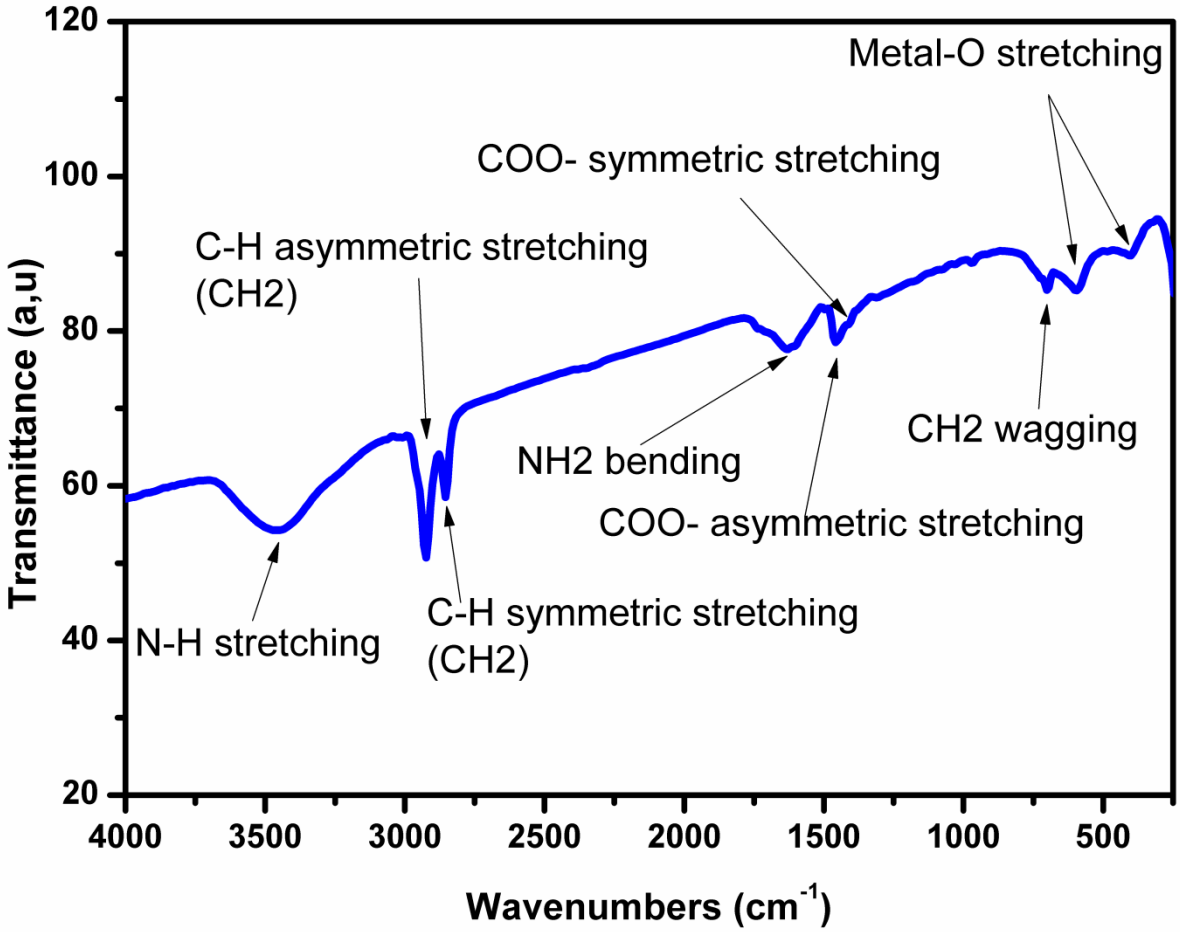


Figure 4. 9: Infrared spectrum of the synthesized $CoFe_2O_4$ nanoparticles.

### 4.5.2 Thermo Gravimetric Analysis (TGA)

Recall that the nanoparticles are covered with an organic layer on the surface. When the particles are heated under an inert atmosphere, this organic layer decomposes at a given temperature, which results in a loss of mass. The quantification of this mass lost during heating makes it possible to calculate the proportion of the organic layer present on the surface of the nanoparticle. The thermogravimetric analysis (ATG) of the nanoparticles was performed by increasing the temperature of the sample from 25 to 600 ° C under an inert atmosphere with a ramp of 5 °C/min. The obtained curves are shown in figure 4. 10. As can be seen in Thermogravimetric analysis (black curve) and differential thermal analysis (blue curve), a mass loss of about 5% is detected below 300 °C, which can be attributed to solvent remainders and adsorbed humidity. However, near to 350°C a mass loss of about 12.5% is clearly identified as the thermal degradation of the surfactants (oleic acid and oleylamine) on the surface of the nanoparticles (the boiling point between 300 °C and 360 °C). Moreover, no other peaks are observed in the range of test temperature, which means that there is no phase change of the

material after heating at high temperature (T ≤600 °C). This diagram confirms thermal stability and negligible structure leaching.

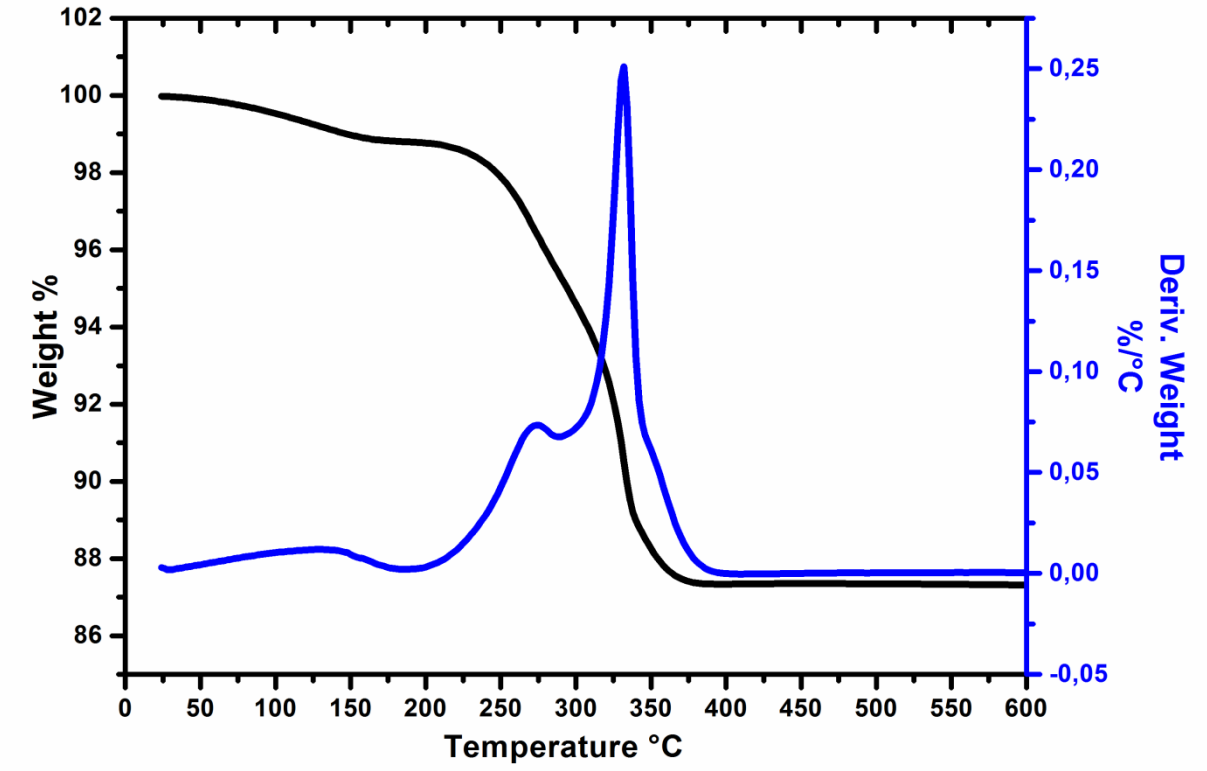


Figure 4. 10: Thermogravimetric analysis (black curve) and differential thermal analysis (blue curve) of the synthesized $CoFe_2O_4$ nanoparticles at atmospheric pressure.

### 4.6 The influence of solvent, surfactant, reductant and synthetic conditions

Various synthesis parameters described above in the standard protocol have been modified in order to know the influence of synthesis parameters on the shape, size, and monodispersity of nanoparticles: the decomposition temperature, the duration of the heat treatment or the quantity of the reagents. This also allowed to better understand the role of reagents such as hexadecanediol, oleic acid, and oleylamine in the synthesis.

The fact of the matter, when the amount of the surfactants increases four times compared to the standard protocol, the obtained nanoparticles are smaller (d = 7.3 ± 2.1 nm), but they show a polydispersion phenomenon, as seen in figure 4. 11(a). Another parameter likely to reduce the particle size is to work under more dilute conditions [67]. For example, a twofold dilution compared to the original protocol, leading to a diameter comparable to the first one (d = 7.8 ± 1.6 nm), but with a lower polydispersity of nanoparticles than those obtained by increasing the amount of surfactants (see Figure 4. 11(b)). On the contrary, for increasing the particle size, we

have increased the duration of the heat treatment, Figure 4. 11(c) shows that the size of $CoFe_2O_4$ nanoparticles increased from 10.7 nm to 13.2 nm when the duration of heat treatment increased from 60 min to 120 min. This result is in good agreement with the work of Perez-Mirabet et al. [68]. In the meanwhile, another parameter could involve in the control of the size of nanoparticles, is the nature of the solvent used during the reaction. Baaziz et al. [69], carried out the synthesis with both polar and non-polar solvents having different boiling temperatures. With the non-polar solvents, the authors found that the size of the nanoparticles increased almost linearly when the boiling temperature of the solvent increased, they suggested that the growth step of the particles depends on the temperature of the reaction. However, using the polar solvents, the size of the nanoparticles deviated from this linear growth. The authors concluded that the nature of the solvent has an influence on the nucleation and growth steps of the nanoparticles. That was related to the stability of the formed metal complexes which depends on the interactions with the solvent and its functional group. Basing on these conclusions, we replaced the benzylether (Bp= 298 °C) by octadecene (Bp= 318 °C) to see the influence of the solvent on size and morphology of nanoparticles. We found that the nanoparticles obtained in octadecene have a higher size than those obtained before in benzyl ether. This result confirms the conclusion of Baaziz et al. [69], which says that the nature of the solvent has an influence on the nucleation and growth steps of nanoparticles.

Concerning the indispensability of the hexadecanediol, Crouse et al. [71] reported that the absence of hexadecanediol does not influence the particle size, but affects nanoparticles polydispersity. The higher is the concentration of hexadecanediol, the greater the particle size distribution is, and with linear dependence. On the other hand, Moya et al. [72] reported that hexadecanediol favors the decomposition of acetylacetonate precursors, and therefore nucleation of the particles at lower temperatures. So, the $CoFe_2O_4$ nanoparticles obtained without hexadecanediol have a defective crystallographic structure. In this context, we have synthesized $CoFe_2O_4$ nanoparticles without hexadecanediol, the STEM image (Figure 4.11(d)) shows that the synthesized particles without hexadecanediol are slightly larger, more polydisperse than those synthesized with hexadecanediol, and have a poorly defined morphology; which is different from the results described above. The role of hexadecanediol in the synthesis is not clearly defined; complementary supporting evidence is needed to shed more light on its influence. Continuously, in order to study the role of each surfactant in the synthesis, $CoFe_2O_4$ nanoparticles were synthesized in the absence of each one. Without oleic acid, the particles are very small and more aggregated (Figure 4.11(e)), whereas without oleylamine the

particles have a poorly defined morphology and are highly polydisperse (Figure 4.11(f)). We surmise then that oleic acid is a surfactant that stabilizes nanoparticles, and oleylamine provides the basic medium necessary to form oxides of the spinel structure.

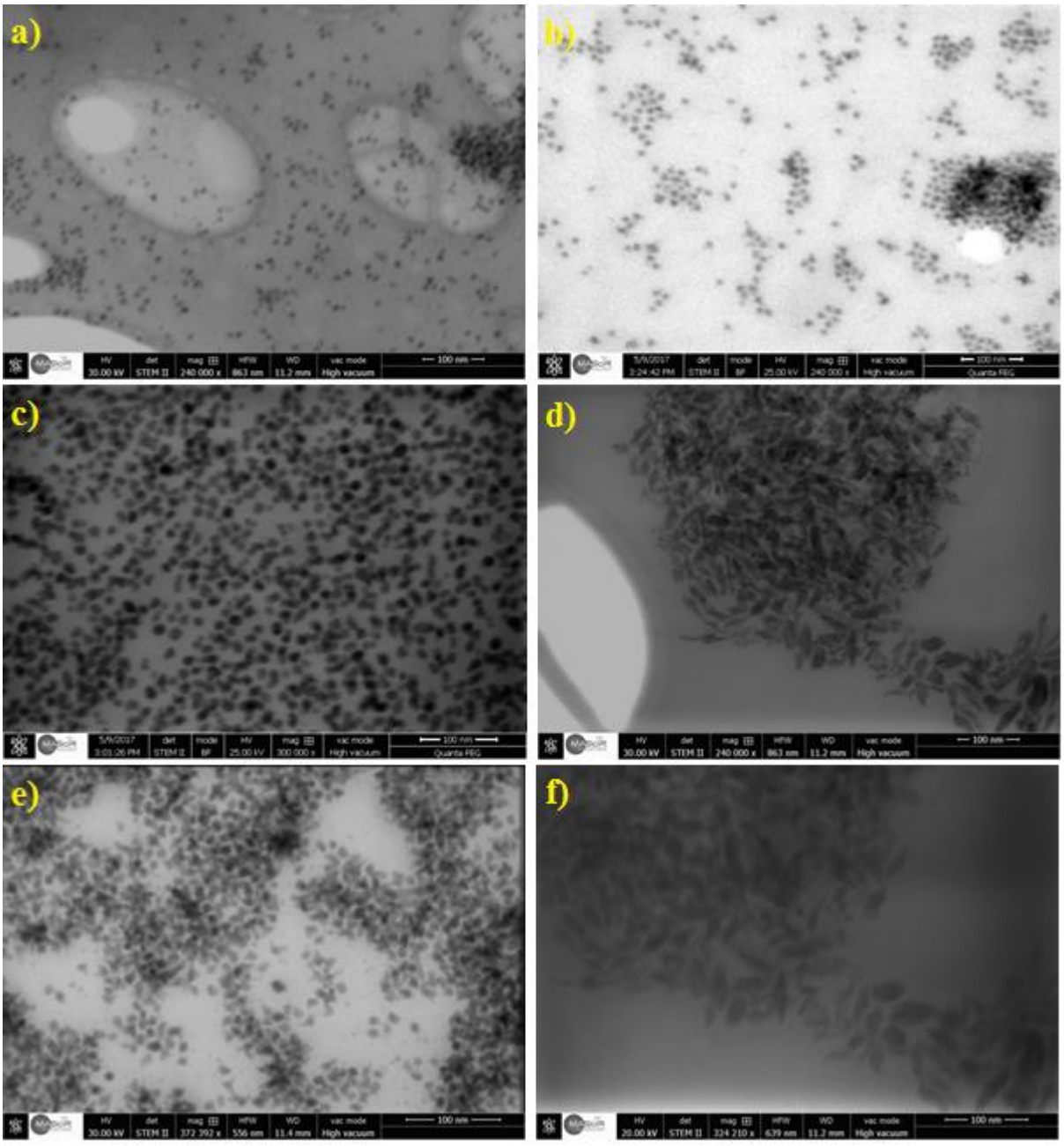


Figure 4. 11: STEM image of the synthesized $CoFe_2O_4$ nanoparticles.

## 4.7 Magnetic properties

Magnetic properties of nanoparticles are highly dependent on their size and composition. In addition, dipolar interactions increase when the distance between particles is reduced, also influence their magnetic behavior. The objective of this part is to compare the magnetic properties of the nanoparticles with and without organic layer on the surface of nanoparticles

in order to evaluate the influence of the dipole interactions between these two states. In this section, nanoparticles of different diameters will be compared to evaluate the influence of nanoparticle size on magnetic properties. For that, we will study the magnetization curves at different temperatures, as well as the magnetization as a function of the temperature under a very weak magnetic field.

### 4.7.1 Sample preparation

In order to evaluate the effect of dipole interactions on magnetic properties, the nanoparticles in powder form (nanoparticles without an organic layer on the surface) were compared to the same nanoparticles surrounded by an organic layer and dispersed in Hexane. In the case of powder form, the particles are close to each other, and the dipolar interactions must modify their individual behavior. Conversely, the nanoparticles surrounded by an organic layer and dispersed in Hexane are far enough apart to greatly reduce the intensity of the dipolar interactions, and try to access to their individual properties.

The intensity of the dipolar interactions is inversely proportional to the square distance between two nanoparticles, and these interactions become negligible below a certain concentration of nanoparticles. However, the magnetization is proportional to the volume of the particles and it takes a sufficient quantity of nanoparticles to have a measurable magnetization, especially for measurements under a magnetic field where the applied field is very small. This constraint imposes a minimum concentration of nanoparticles to have measurements with a good resolution.

Nanoparticles surrounded by organic layer are directly deposited in the SQUID capsule by depositing drops of suspension in hexane and allowing the solvent to evaporate at room temperature. The mass obtained at the end of evaporation varies between 5 and 10 mg.

To study $CoFe_2O_4$ nanoparticles without the organic layer on the surface, we removed the organic layer by a heat treatment at 400 °C for 2 hours. After the heat treatment, the powder was put directly into the SQUID capsule by using a spatula. The mass used for the measurement varies between 5 and 10 mg.

### 4.7.2 Influence of organic layer on magnetic properties for nanoparticles of about 10 nm

The first characterization consists in studying the sample magnetization as a function of the applied magnetic field. The magnetization measurements are carried out at different temperatures after cooling the sample without applied magnetic field and by varying the field between 0 T and +6 T then between +6 T and -6 T, then between -6 T and +6 T. In our case, we recorded the cycles at 10 K and 300 K, which are the temperatures usually used in the literature to characterize the magnetization of nanoparticles.

A second characterization consists in recording the variation of the magnetization as a function of the temperature under a weak magnetic field. At first, the magnetization is recorded between 10 K and 300 K under a magnetic field of 200 Oe after decreasing the temperature from the ambient temperature to 10 K without applying a magnetic field. This measurement results in a curve named ZFC (Zero Field Cooled). The sample is then cooled from 300 K to 10 K maintaining the field of 200 Oe, and the magnetization is recorded between 300 K and 10 K, always under a magnetic field of 200 Oe. This measurement results in a curve named FC (Field Cooled) (See Chapter 1 for more details).

Figure 4.12 shows the magnetization curves as a function of the magnetic field at 300K and 10K of $CoFe_2O_4$ nanoparticles. As it is clearly seen from the plots, a difference in saturation magnetizations of about 12% is spotted between $CoFe_2O_4$ nanoparticles with and without organic molecules on the surface. Therefore, the contribution of the organic layer is estimated at 12%. This value agrees well with that one found by TGA measurement (12.5%).

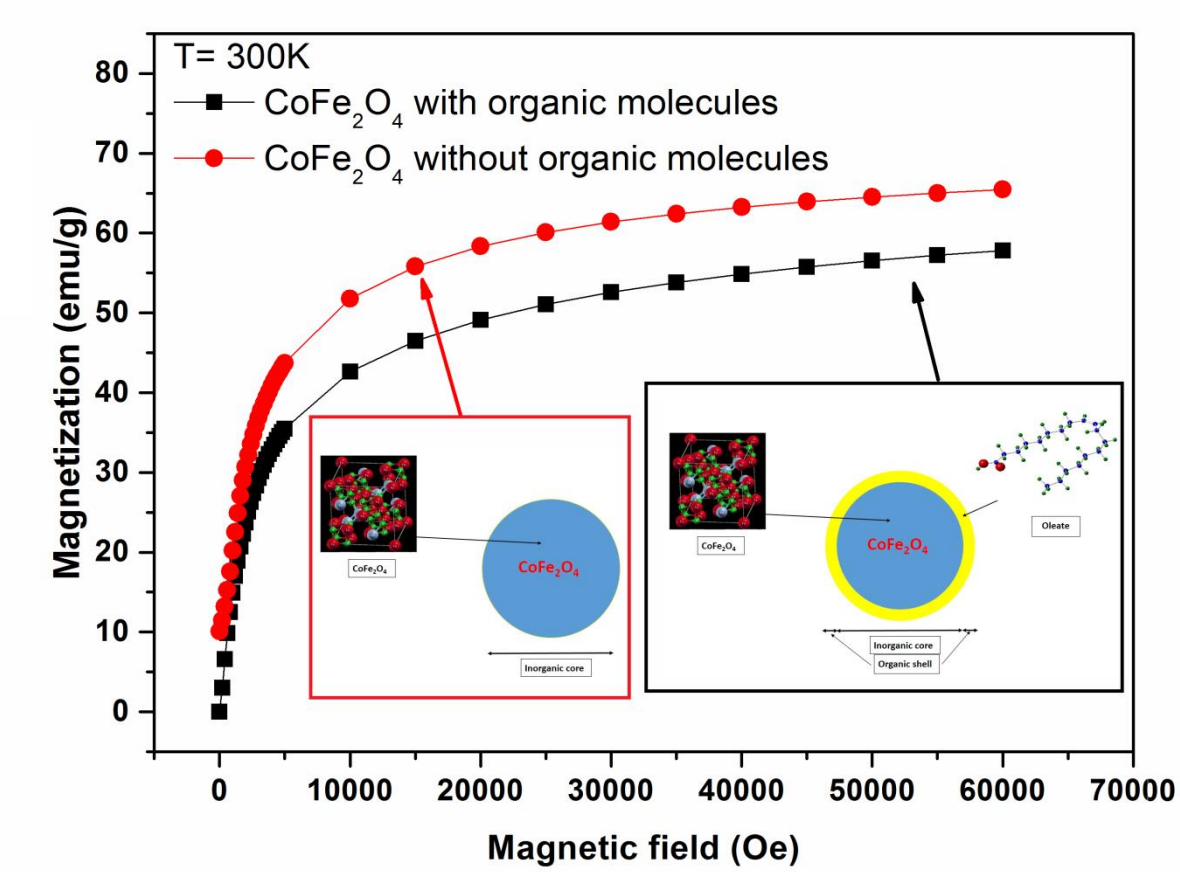
T= 300K
CoFe2O4 with organic molecules
CoFe2O4 without organic molecules
Magnetization (emu/g)
Magnetic field (Oe)
0
10
20
30
40
50
60
70
80
0
10000
20000
30000
40000
50000
60000
70000
CoFe2O4
Inorganic core
Oleate
Organic shell

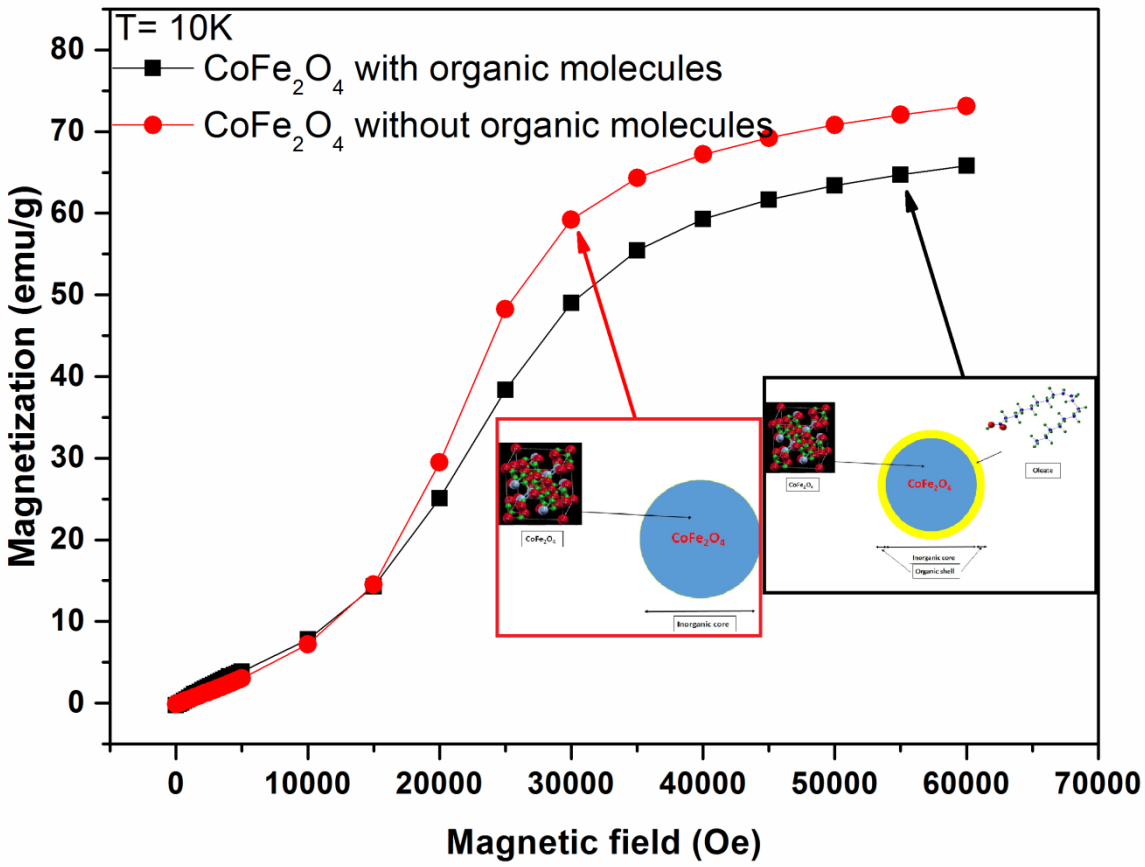
T= 10K
CoFe2O4 with organic molecules
CoFe2O4 without organic molecules
Magnetization (emu/g)
Magnetic field (Oe)
0
10
20
30
40
50
60
70
80
0
10000
20000
30000
40000
50000
60000
70000
CoFe2O4
Inorganic core
Oleate
Organic shell

Figure 4. 12: Magnetization as a function of a magnetic field of $CoFe_2O_4$ nanoparticles with and without magnetic field at 10 K (bottom) and 300 K (top).

Note that the saturation magnetizations is higher at 10 K than at 300 K for the synthesized nanoparticles. Indeed, spins are better aligned at low temperatures because there are fewer thermal fluctuations. These results are in agreement with the values observed in the literature for bulk materials [73].

At room temperature (300 K), the behavior of $CoFe_2O_4$ nanoparticles surrounded by the organic layer is superparamagnetic (Figure 4. 13). The orientation of their magnetic moments responds freely to thermal fluctuations. Its magnetization curve is reversible and follows the Langevin model (see Chapter 1. 2). When we adjust this curve by the Langevin model we can deduce the magnetic size. The magnetic size obtained for the synthesized $CoFe_2O_4$ nanoparticles is summarized in Table 4. 2 and it is compared to the size obtained by scanning transmission electron microscope. A similar size is found by both techniques, and a small difference observed, this difference is due to the approximations made during the adjustment by the Langevin model.

| Ferrite | $d_0$ STEM (nm) | $d_0$ magn (nm) |
|---|---|---|
| $CoFe_2O_4$ | 10.7 | 9.6 |

Table 4. 2: STEM and magnetic sizes of synthesized cobalt ferrite nanoparticles.

At low temperature (10 K), the sample is frozen and we find the intrinsic characteristics of the $CoFe_2O_4$ nanoparticles. The magnetization curve follows the Stoner-Wohlfart model and exhibits an open hysteresis loop (Figure 3. 13). Therefore, the nanoparticles are in a locked state. Cobalt ferrite is a hard magnetic material because it has a large hysteresis loop and a high coercive field.

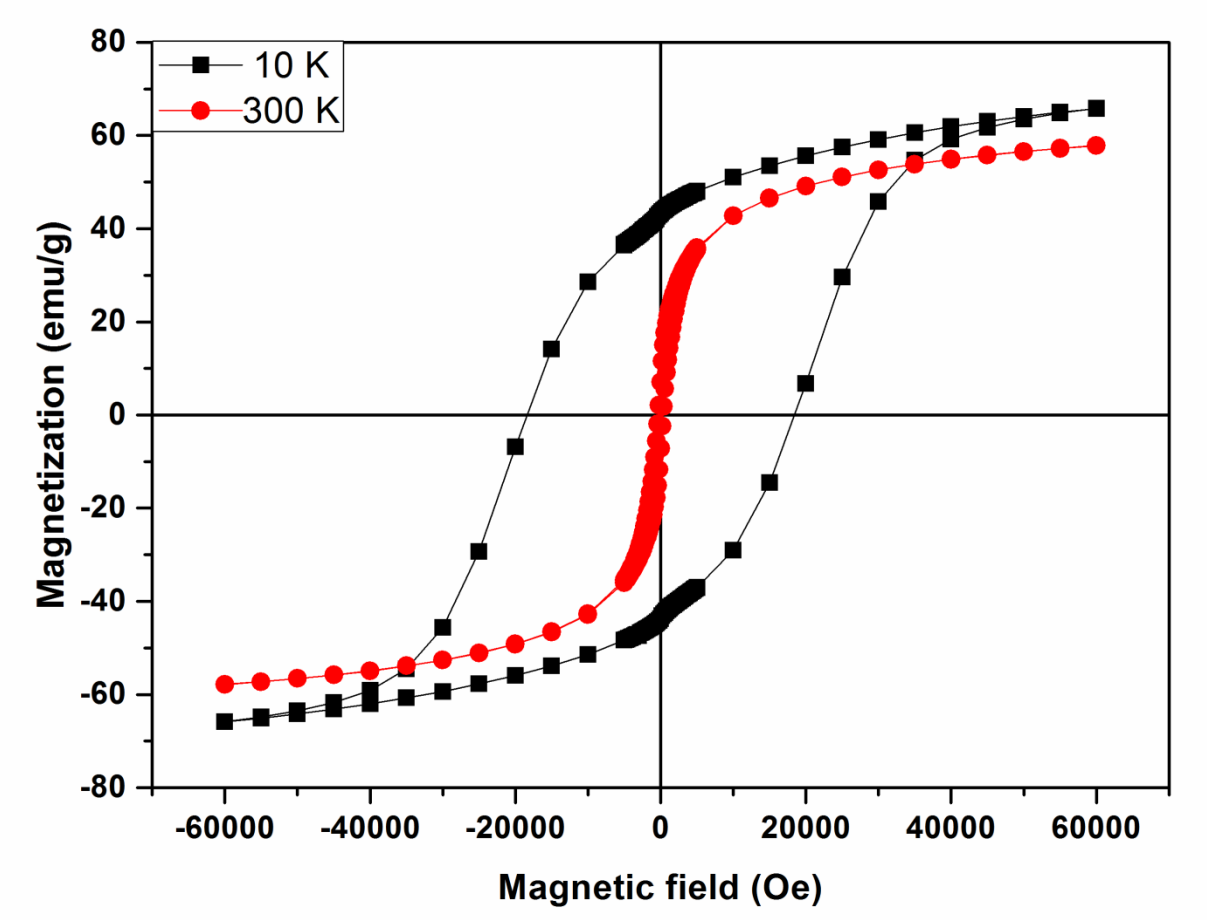


Figure 4. 13: Hysteresis loops of the $CoFe_2O_4$ nanoparticles surrounded by organic layer measured at 10 K and 300 K.

The Hysteresis loops of $CoFe_2O_4$ nanoparticles without organic layer are presented in figure 4.14. Field dependent magnetization studies performed at temperatures of 10 and 300 K on $CoFe_2O_4$ nanoparticles showed that the saturation magnetization ($M_S$) increases when the organic layer is removed at both temperatures.

Cobalt iron oxide nanoparticles surrounded by an organic layer are characterized by $M_S$ values of 65.84 (10 K) and 57.84 emu/g (300 K) whilst those without organic layer on the surface exhibit $M_S$ values of 73.56 (10 K) and 65.47 emu/g (300 K). Bulk cobalt iron oxide was reported to have $M_S$ = 80 emu/g at room temperature which is greater than that observed for our cobalt iron oxide nanoparticles [74]. Such a difference is often observed with the nanoparticles and is most likely attributed to the existence of organic layer, and intrinsic spin disorder, at the surface of such small nanoparticles [75][76].

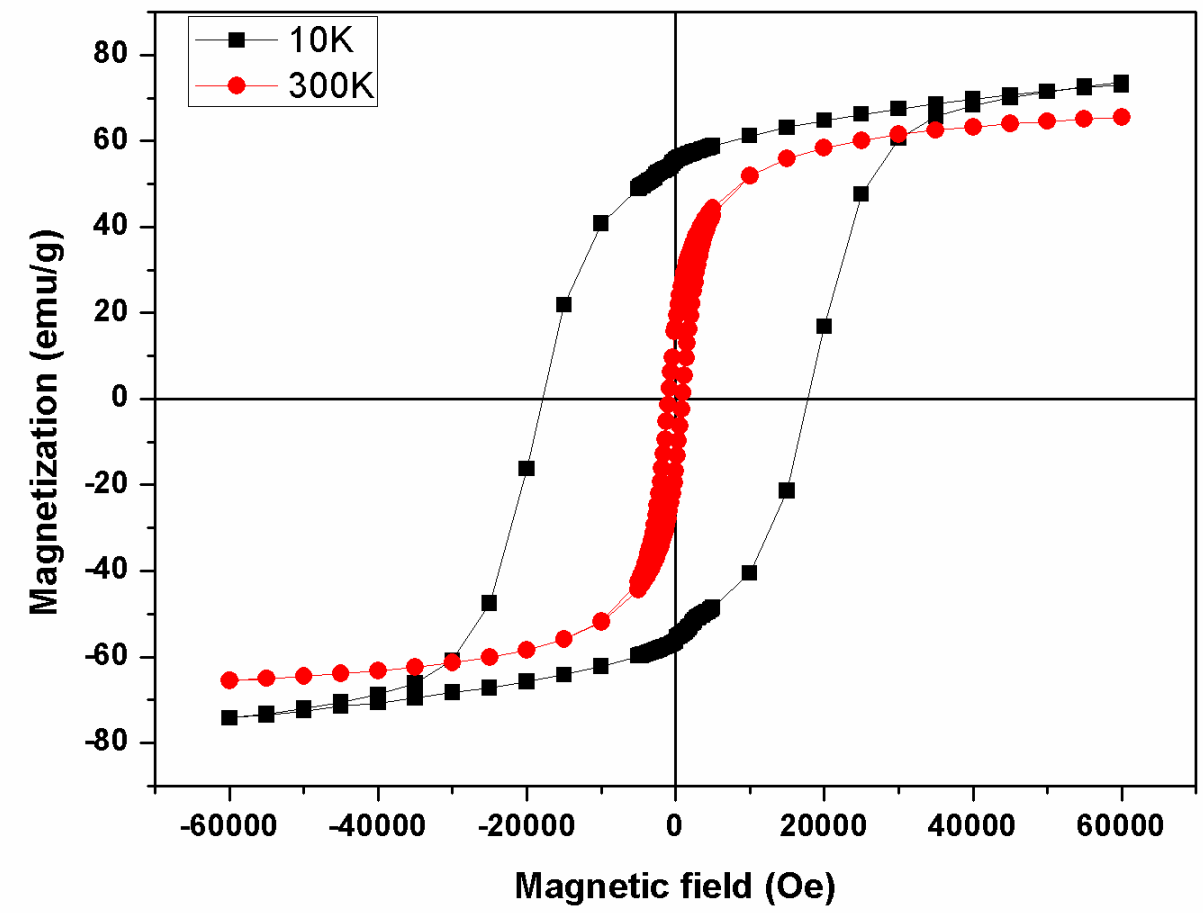


Figure 4. 14: Hysteresis loops of the $CoFe_2O_4$ nanoparticles without the organic layer on the surface measured at 10 K and 300 K.

Remarkably, the magnetization versus field measurements at 10 K have revealed the presence of a large hysteresis loop with values of the coercive field ($H_C$) (i.e. the magnetic field needed for the magnetization to return to zero) and remanent magnetization ($M_R$) (i.e. the magnetization retained by nanoparticles when the magnetic field is switched off) of 18.33 kOe and 43.31 emu/g for cobalt iron oxide nanoparticles surrounded by organic layer, and 17.68 kOe and 55.44 emu/g for those without organic layer. Such behavior is directly correlated with the large magnetic anisotropy of the cobalt iron oxide nanoparticles [77]. In addition, the slightly higher Cobalt content of the nanoparticles without organic layer as compared to those with the organic layer is likely to justify their lower $M_S$ and $M_R$ values.

Table 4.3 summarizes the values of the coercive fields ($H_C$), saturation magnetization ($M_S$), and remanent magnetization ($M_R$) of $CoFe_2O_4$ nanoparticles with and without organic layer.

| | $CoFe_2O_4$ nanoparticles **with** the organic layer | | $CoFe_2O_4$ nanoparticles **without** the organic layer | |
|---|---|---|---|---|
| Temperature (K) | 10 | 300 | 10 | 300 |
| $M_S$(emu/g) | 65.84 | 57.84 | 73.56 | 65.47 |
| $M_S$(emu/g) | 43.31 | 7.09 | 55.44 | 16.52 |
| $H_C$(Oe) | 18333 | 315 | 17680 | 930.5 |

Table 4. 3: Coercive fields ($H_C$), saturation magnetization ($M_S$), and remanent magnetization ($M_R$) of $CoFe_2O_4$ nanoparticles.

As presented in Chapter 1, the transition from the superparamagnetic state to the blocked state occurs at a temperature called the blocking temperature $T_B$. This depends on the material but also on the particle size. To access to this blocking temperature, we follow the evolution of the magnetization as a function of the temperature.

Magnetic measurements of $CoFe_2O_4$ nanoparticles revealed that the nanoparticles display superparamagnetic behavior near room temperature, that is, the orientation of their magnetic moments responds freely to thermal fluctuations. This property is important for many applications. An estimate for the blocking temperature ($T_B$) of the $CoFe_2O_4$ nanoparticles surrounded by organic layer is obtained through examination of the field-cooled (FC) and zero-field-cooled (ZFC) magnetization curves collected at 200 Oe magnetic field (Figure 4. 15). This blocking temperature defines the crossover between ferrimagnetism and superparamagnetism and is graphically determined to be the point at which the gradient of the ZFC curve approaches zero [78]. The data show that blocking temperature ($T_B$) of the $CoFe_2O_4$ nanoparticles surrounded by the organic layer is greater than 300 K.

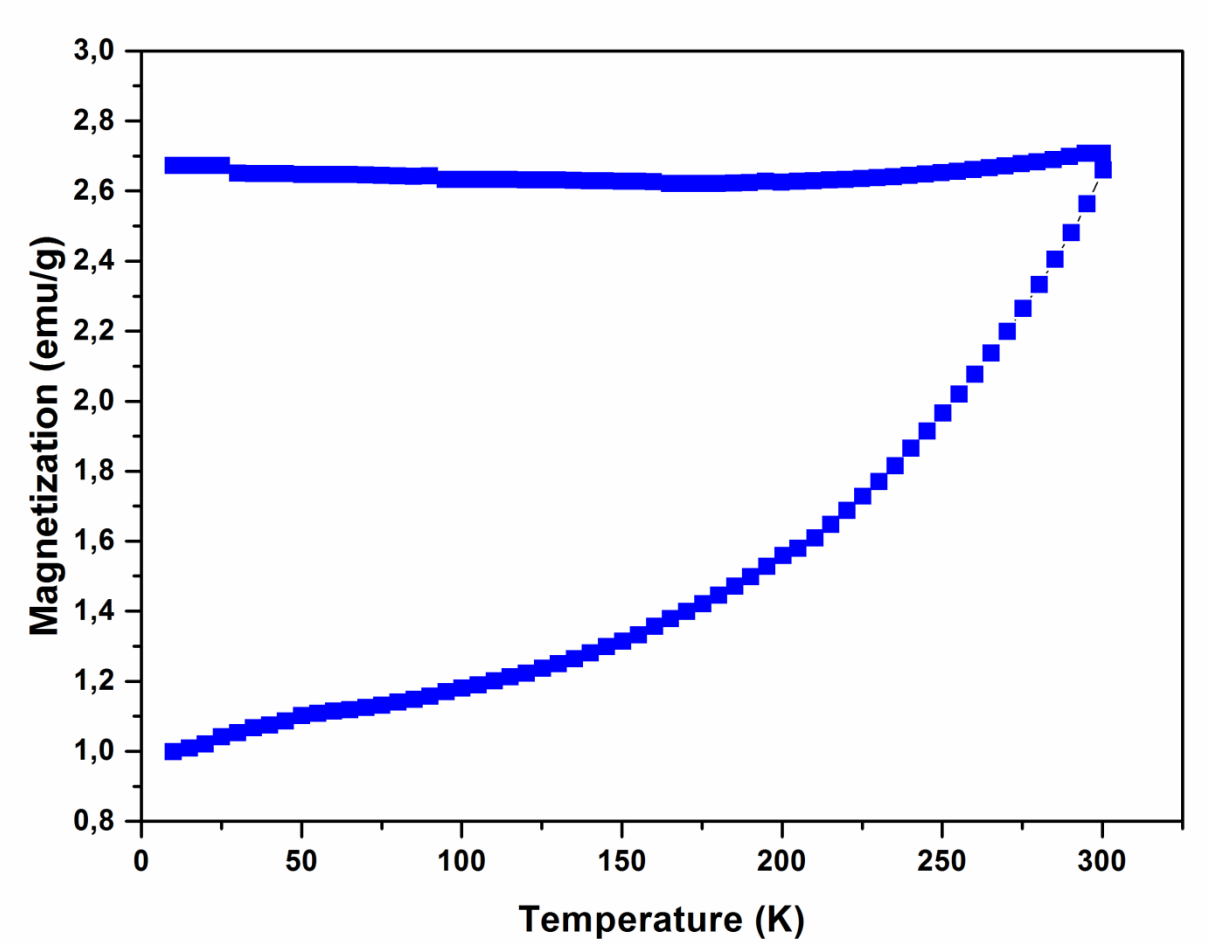


Figure 4. 15: ZFC/FC curves of cobalt ferrite nanoparticles measured at temperatures ranging from 10 K to 300 K and with an applied magnetic field of 200 Oe.

Above the blocking temperature, the thermal energy is enough to overcome the anisotropy energy barrier of the particles, thus the remanent magnetization tends towards zero and the particles are said to exhibit superparamagnetism [69].

➢ Anisotropy constant

According to the model of Stoner-Wohlfarth seen in Chapter 1, we can calculate the constant of anisotropy using the measured values of the coercive field and saturation magnetization at 10K.

$$K = 25.K_B T_B V^{-1}$$

Where $K_B$ is the Boltzman constant, $T_B$ is the blocking temperature of the samples, and V is the volume of a single particle. The calculated magnetic anisotropy constant (K) of our sample is found equal to$1.6*10^5$ $J.m^{-3}$. This estimated value is comparable with the value reported in the literature for the bulk material [79].

### 4.7.3 Influence of particle size on the magnetic properties of $CoFe_2O_4$ nanoparticles surrounded by the organic layer

To better understand the influence of particle size on magnetic properties, magnetization as a function of applied magnetic field measurements are made for $CoFe_2O_4$ nanoparticles of different sizes. The measured hysteresis loops of cobalt ferrite nanoparticles at 10 K, with sizes ranging from 5 to 15 nm, are plotted in Figure 4. 16. We notice that the evolution of $H_C$ as a function of the size is gradual but moderate compared to the large increase in the particle size.

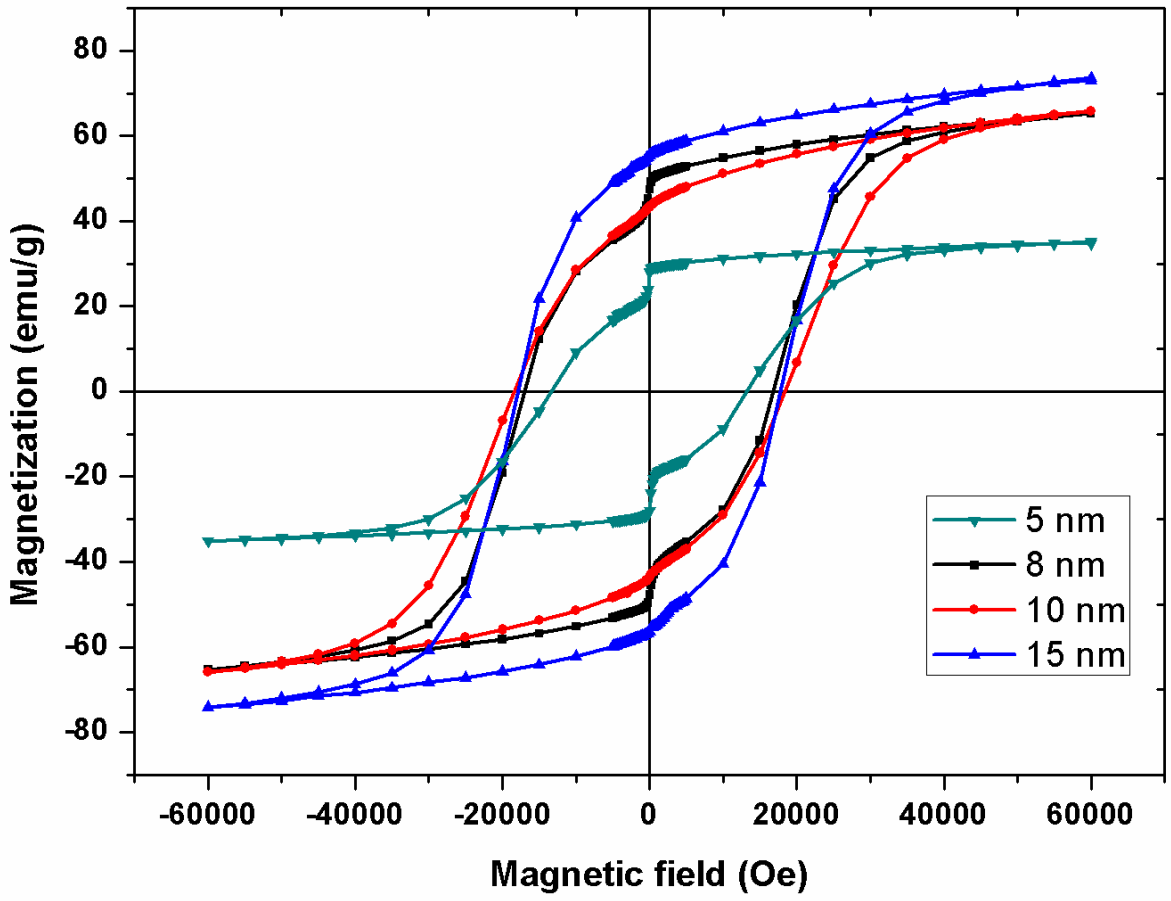


Figure 4. 16: The measured hysteresis loops of cobalt ferrite nanoparticles at 10 K with different sizes.

The magnetization curves at 10 K show the magnetic characteristics of $CoFe_2O_4$ nanoparticles below the blocking temperature for four sizes. All sizes show a high coercive field, and non-zero remanent and saturation magnetization. In order to compare the hysteresis cycles, the values of coercive field $H_C$, the ratio $M_R/M_S$ and saturation magnetization $M_S$ are reported in Table 4. 4 as a function of the diameter of the particle.

| | $H_C$ (Oe) | $M_R$ / $M_S$ | $M_S$ (emu/g) |
|---|---|---|---|
| NP5 nm | 13294 | 0.80 | 34.81 |
| NP8 nm | 16968 | 0.72 | 64.91 |
| NP10 nm | 18398 | 0.65 | 65.97 |
| NP15 nm | 17872 | 0.75 | 73.09 |

Table 4. 4: Values of coercive field $H_C$, the ratio $M_R$ / $M_S$ and saturation magnetization $M_S$ for different diameters of the particle.

The coercive field increases with the size of the particles then decreases for the size greater than 12 nm, which has already been observed for similar particles [80][81][82]. In order to explain this result, the analogy can be made with the multi-domain magnetic material. Cobalt ferrite nanoparticles are monodomains, but we can suppose that the reversal of the magnetization could be done in the same way as in a material composed of several magnetic domains by assimilating each nanoparticle to a magnetic domain. Commonly, in a multi-domain material, the reversal of the magnetization is done by the displacement of the walls. However, the coercive field is related to the nucleation field of the domains and the field of the propagation of walls. The field of propagation of walls passes through a maximum according to the size of the grains, when this size is comparable to the width of walls. In addition, the coercive field follows the same trend when the field of the propagation of walls is greater than the nucleation field.

On the other hand, the saturation magnetization $M_S$, at 10 K, of NP5, NP8, NP10, and NP15 were found to be 34.81, 64.91, 65.97 and 73.09 emu/g, respectively. Such values are in good accordance with those reported for $CoFe_2O_4$ nanoparticles with similar sizes and prepared by the thermal decomposition method. Song Q. reported $M_S$ values in the range of 60-80 emu/g for spherical and cubic $CoFe_2O_4$ of 5-13 nm [83], while Cabrera L.I. found that nanoparticles of 12 nm display an $M_S$ value of 54 emu/g [84]. Indeed, the saturation magnetization values of $CoFe_2O_4$ at the "nanometer scale" vary with the synthesis method and increases as a function of the size, but still lower than those of bulk cobalt ferrite (80 emu/g) [85], due to the presence of defects and a surface and volume spin canting [86][87][88].

It is also seen that there are jumps on small size curves (NP5 and NP8) when the external magnetic field became zero from both positive and negative saturated magnetization states. This physical phenomenon can be attributed to the low temperature spin reorientation and the crystal alignment of $CoFe_2O_4$ nanoparticles, which is not observed for NP10 and NP15. This is also attributed to the domain-wall pinning, the separation angle between the effective magnetic moment and the applied field which is at an acute angle at zero field as illustrated in the figure

4.17, resulting in a change of the magnetization. The domain wall pinning happens when the direction of the applied field changes to the opposite direction.

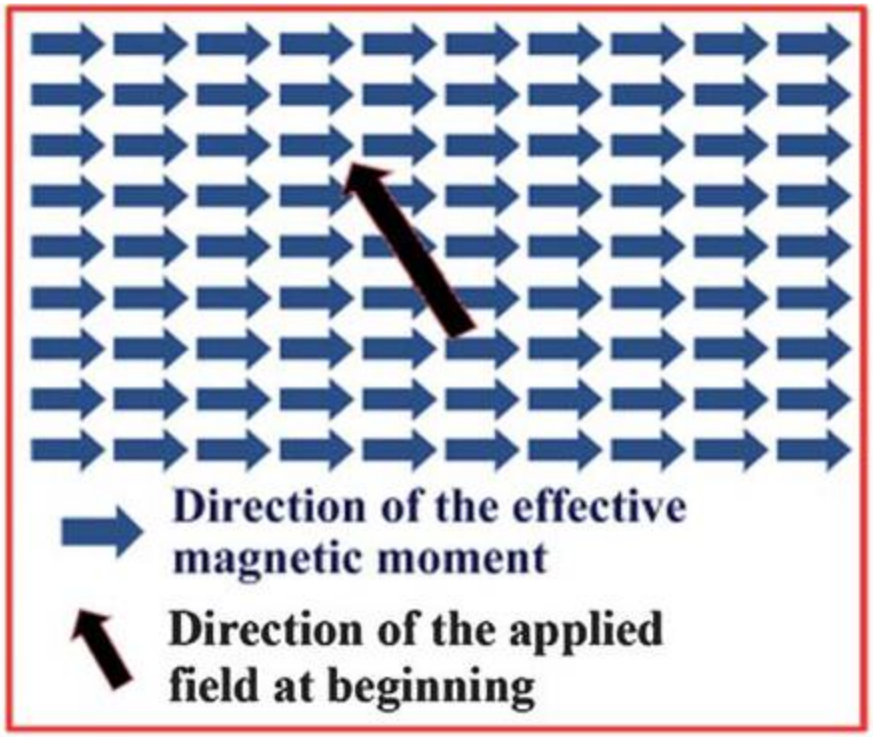


Figure 4. 17: Inset illustrating the origin of the skew in the hysteresis loops for $CoFe_2O_4$ NP5 and NP8 at 10 K and zero field.

## 4.8 Conclusion

In conclusion, spherically-shaped nanoparticles of cobalt ferrite have been synthesized with controlled size and very narrow size distribution by adjusting the experimental conditions of thermal decomposition of metal complexes such the nature of precursors, surfactants, reductant, and solvents. We reported also that using acetylacetonate as precursors with oleic acid and oleylamine as surfactants lead to spherical nanoparticles exhibiting a core-shell structure with a $CoFe_2O_4$ in core and an organic layer at the surface as a shell.

We demonstrate in this work that this crystalline structure is due to the reducing environment owing to the presence of hydrocarbon, carboxylate groups, and oleic acid surfactant. The structure was investigated by STEM, XRD, FT-IR, and Raman spectrometry. We have shown that using STEM analysis, the size, and shape of NPs could be controlled by varying certain parameters such as the synthesis temperature, the quantity, and nature of reagents. In addition, EDS, XRD, and Raman spectroscopy measurements confirmed the formation of $CoFe_2O_4$ nanoparticles with spinel structure. Furthermore, FT-IR analysis allows identifying the

presence of functional groups of organic molecules surrounding nanoparticles as well as the vibrational modes of metal-oxygen bonds for spinel structure.

Finally, we highlight a room temperature superparamagnetic of the synthesized $CoFe_2O_4$ nanoparticles and low temperature (10 K) blocked state. We found that the magnetic properties ($H_C$, $T_B$, $M_S$) depend on the size and the organic layer surrounded nanoparticles. Indeed, the increase of their size has an important influence on their saturation magnetizations as well as their coercive field.

# 5 Insertion of cobalt ferrite nanoparticles into a porous anodic aluminum oxide (AAO)

## 5.1 Introduction

The magnetoelectric effect can be found intrinsically in some materials only at very low temperatures. The use of magnetostrictive and piezoelectric materials makes it possible to overcome this problem by coupling them mechanically.

A new route consists of designing composite materials that could be described as "extrinsic" multiferroic, combining ferroelectric and ferromagnetic materials. A coupling is then performed by the mechanical stresses between the two related materials. By applying a magnetic field, the ferromagnetic will deform by magnetostrictive effect, and thus transmit the constraints to the piezoelectric which change its dielectric properties, such as polarization, and vice versa. The magnetoelectric composites could have various connectivity schemes, but the common connectivity schemes are 0-3–type particulate composites of piezoelectric and magnetic oxide grains, 2-2–type laminate ceramic composites consisting of piezoelectric and magnetic oxide layers, and 1-3–type nanorods composites with nanorods of one phase embedded in the matrix of another phase.

In this thesis, 1-3–type nanorods composite is chosen to be the connectivity scheme. Several methods and approaches have been discussed for making this type of nanocomposites. We have developed a new approach to transfer $CoFe_2O_4$ nanoparticles to nanorods by using the AAO template.

The main method (or idea) is to incorporate and solidify spherical magnetic particles of $CoFe_2O_4$ with size less than 20 nm in a synthesized porous alumina membrane. In such configuration, all the magnetic particles are oriented according to an external magnetic field and keep in this orientation even without a magnetic field after solidification of the matrix. The procedure consists of three preliminary steps. Firstly, mixing well-dispersed $CoFe_2O_4$ nanoparticles in a solvent (Hexane), allowing a change from the liquid state ($CoFe_2O_4$ nanoparticles surrounded by organic layer and dispersed in Hexane) to the solid state (Only $CoFe_2O_4$ Nanoparticles). Secondly, incorporation of $CoFe_2O_4$ nanoparticles into pores of the alumina membrane. Thirdly, a step of a heat treatment compatible with the magnetic

nanoparticles is necessary in order to evaporate all the organic compounds. The insertion of nanoparticles has been done with the help of an external magnetic field.

We should mention that the porous alumina membranes used in this thesis work were fabricated by the team of Mohammed Es-Souni at the Institute for Materials and Surface Technology/IMST - University of Applied Sciences, Kiel, Germany. The AAO template was synthesized with a diameter of 2 cm, a thickness of 650 nm and a porosity of 68%. The membranes have an average pore diameter of 92 nm. $CoFe_2O_4$ nanoparticles were synthesized by the thermal decomposition method. The average diameter of the nanoparticles is between 8 nm and 14 nm (Figure 5. 10) and well dispersed in hexane. These nanoparticles have been prepared in Mascir's laboratory.

## 5.2 Membrane growth

In 1970, O'Sullivan and Wood [89] presented a model to describe the self-organized growth of pores in alumina. This model is based on the distribution of the electric field in the oxide layer. The pore growth, perpendicular to the surface, results from an equilibrium between the dissolution of the oxide at $Al_2O_3$/electrolyte interface and the growth of the oxide at $Al/Al_2O_3$ interface [89][90]. This model shows that oxide formation is due to the migration of ions containing oxygen ($O^{2-}$, $OH^-$) from the electrolyte to the bottom of the pores (Figure 5. 1, red circle), through the oxide layer. On the other hand, the $Al^{3+}$ ions simultaneously pass through this layer in the opposite direction and are released into the electrolyte at $Al_2O_3$/electrolyte interface.

The growth of $Al_2O_3$ takes place at $Al_2O_3$/Al interface following the chemical reaction:

$$2Al^{3+} + 3O^{2-} \longrightarrow Al_2O_3$$

The fact that the $Al^{3+}$ ions are transferred to the electrolyte could explain the formation of the porous oxide. However, these $Al^{3+}$ ions contribute to the formation of the layer itself. The density of aluminum atoms in alumina is twice lower than that in metallic aluminum. The mechanical stresses associated with the volume expansion, that occurs during oxide formation, are responsible for forces between neighboring pores [91]. Thus, the dissolution of the oxide being at the same rate as its growth at the bottom of each pore, it results in the formation of vertical walls. Figure 5. 1 depicts more generally the steps of the growth of the porous oxide. During the early stages of the application of the anodizing voltage, a layer called barrier layer

is formed whose thickness is proportional to the anodization voltage (step a). Small variations in the topography of this layer induce inhomogeneities in the applied electric field (step b). This causes locally increase in the rate of dissolution of the oxide. The depth of the pores increases while the dissolution of the alumina separating two pores slows (step c). During the anodization, the pores deepen continuously (step d).

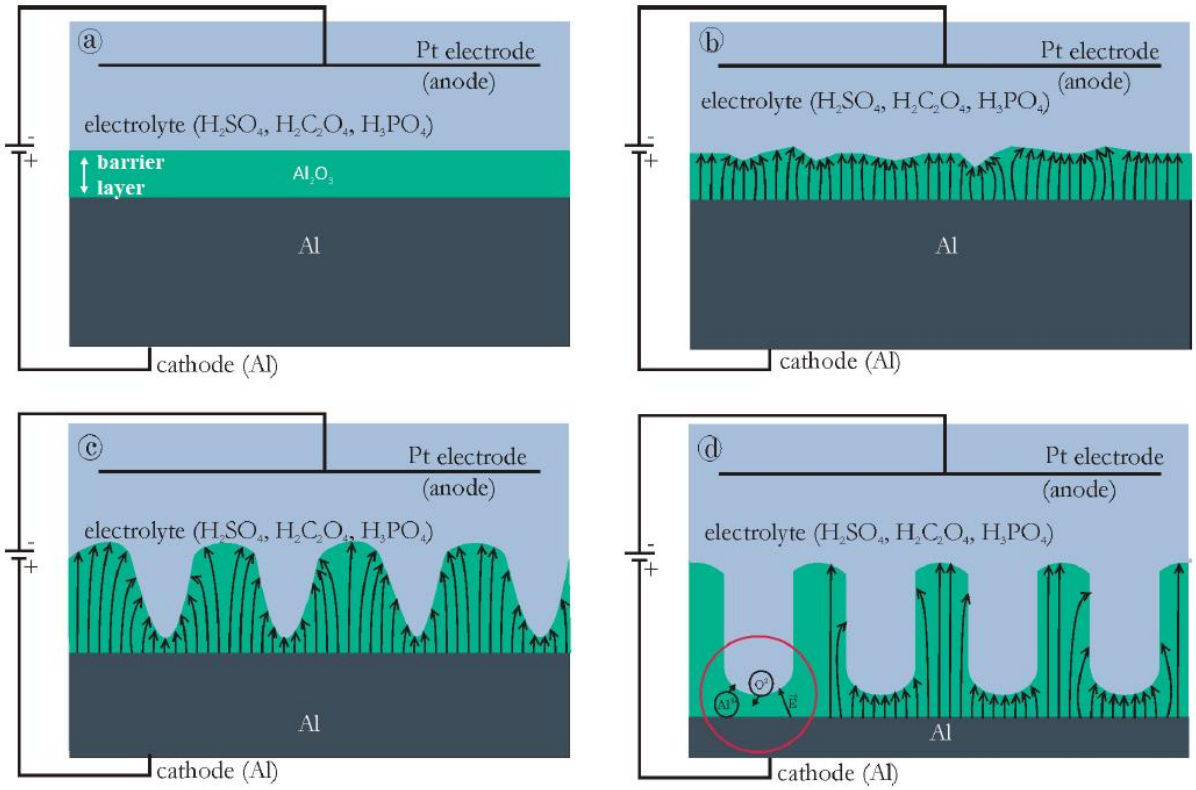


Figure 5. 1: The different steps of pore formation

Masuda and Fukuda [92] were the first who find the specific anodizing conditions to a pores configuration with an ordered arrangement through a double anodizing technique. Indeed, the elaboration of alumina having a highly ordered pores network is possible only in the range of specific voltages for each acid used. The pore size evolves linearly with the applied voltage, with a constant factor equal to 2.5 nm/V :

$$D_{int} \approx 2.5 * V$$

Where $D_{int}$ is the average distance between pores in nm and V in Volts.

In addition, the distance between pores can reach up to three times the pore diameter. The table summarizes the characteristics of the membranes obtained at different tensions.

| Acids | $H_2SO_4$ | $H_2C_2O_4$ | $H_3PO_4$ |
|---|---|---|---|
| Voltage (V) | 25 | 40 | 195 |
| $D_{int}$ (nm) | 60 | 120 | 500 |
| $D_{pore}$ (nm) | 20 | 40 | 180 |
| Density ($cm^{-2}$) | $4.1*10^{10}$ | $1.1*10^{10}$ | $0.41*10^{9}$ |

Table 5. 1: Characteristics of alumina membranes [93]

## 5.3 Elaboration of alumina membranes

For the fabrication of AAO template, it is first necessary to process an heterostructure thin-film on a substrate consisting of an adhesion layer, an electrode, and the Al-film to be anodized. The adhesion layer is usually an ultra-thin film of Ti with a few nanometers (2–5 nm) on top of which an Au-film of 5–20 nm is sputtered to serve as an electrode. In order to improve the adhesion between Au and the subsequently deposited Al-film, it is advised to use the same Ti adhesion layer. The main advantage of Ti lies in its ability to form strong intermetallic bonds with both metals at the interface (see related phase diagrams [94][95]). A PVD system that allows deposition of the thin-film heterostructure without breaking the vacuum (in order to prevent oxidation of the reactive metals) is best suited for high-quality AAO template. However, because the Al-film is subjected to high stresses during anodization, the requirements on the Al-film adhesion are high. Further, the formation of well-ordered pore domains is dependent on film microstructure and roughness. Films free of spikes and highly smooth are best suited. Noting that the conditions for obtaining these films must be iterated for the particular substrate and PVD system used. The experience set up of growing heterostructures films using either sputtering (RF or DC) or e-beam evaporation of Al- layer is summarized below.

In fact, sputtering of Ti and Au is in principle easily achieved. Providing a clean substrate and a PVD chamber free from contaminants, are among the critical issues to be dealt with when depositing the Al-film. Sputtering of Al had in this case invariably led to rough films because the sputtering rate of Al was relatively low at the chosen conditions (below 0.16 nm/s at an argon pressure of 10−3 mbar and 220 W; these conditions were iteratively found to yield films with best adhesion properties for successful anodization). Under these conditions, the

deposition of the desired 500–600 nm thick films took approximately 1 h, which resulted in substrate heating and grain growth. Even when the films were sputtered with extreme precaution to avoid heating, e.g., sequential sputtering with waiting time for the substrate to cool down, the results remained unsatisfactory. Anodization of such films leads to poor pore ordering.

Smoother and more homogeneous Al-films are obtained at high deposition rates by electron beam evaporation while maintaining the substrate at low temperature. In this process, an applied magnetic field allows dynamically deflecting the electron beam in x–y directions with a given frequency in order to ensure homogeneous material evaporation. In addition, the substrate is rotated during deposition to achieve uniform material thickness over the whole surface. A PVD system equipped with a module for e-beam evaporation is, therefore, necessary in order to obtain high-quality Al-films. After the sequential sputtering of Ti and Au, Al is e-beam evaporated without breaking the vacuum.

Once a well-adherent film heterostructure with a smooth Al-film is obtained, anodization is straightforward and is in principle similar to that of bulk Al, involving the same electrochemical reactions and mechanisms leading to pore formation [96][97]. Usually, anodization is performed in oxalic acid ($C_2H_2O_4$) at a constant voltage of 40 V. Either one-step or two-step anodization is possible with better pore ordering for the latter. The kinetics is rather fast with complete anodization of 500 nm – 1µm Al-films being accomplished within few minutes. Barrier-layer etching and pore widening is achieved in a dilute solution of KOH or NaOH. Figure 5. 2 schematically depicts the different processing steps of AAO elaboration [98].

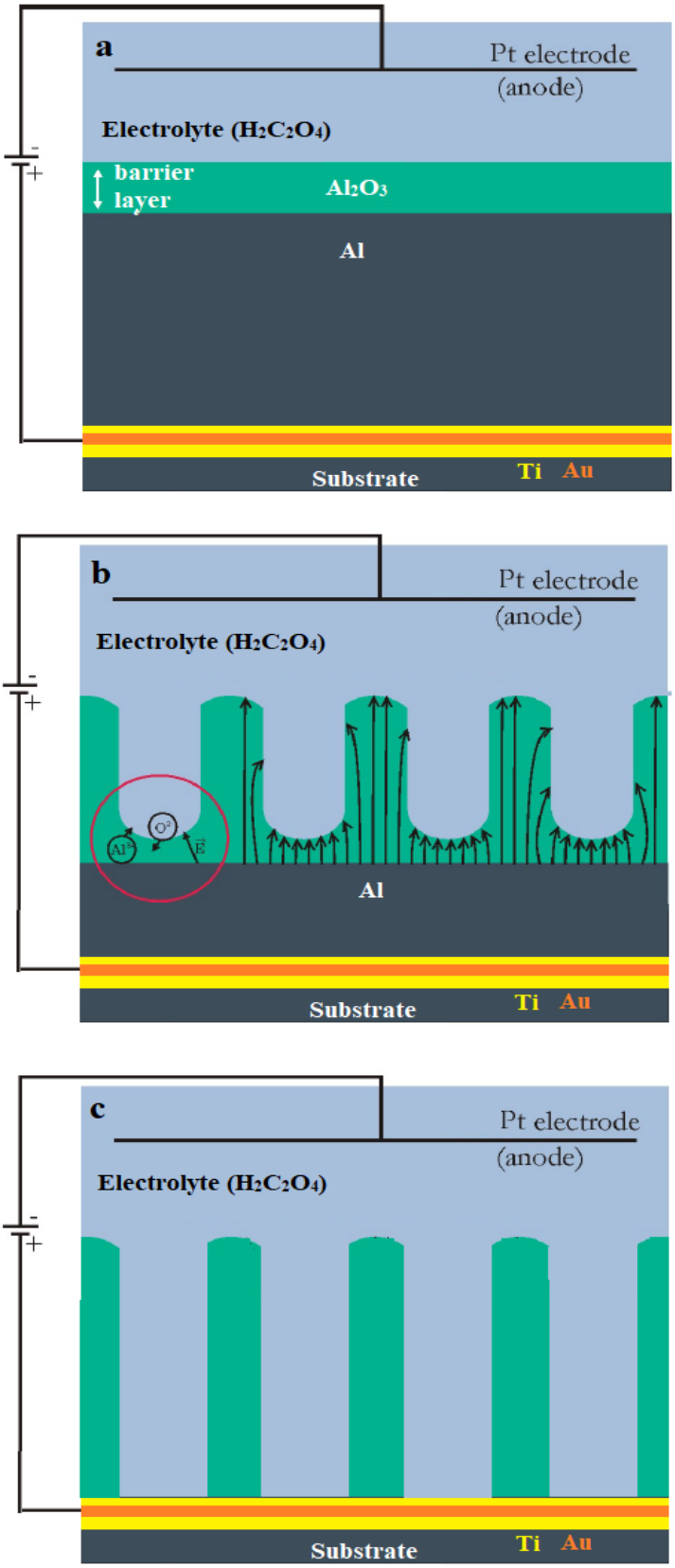


Figure 5. 2: Schematic illustration of the processing steps of AAO elaboration : (a) film heterostructure, (b) anodization, and (c) barrier-layer opening

Figure 5. 3 shows the digital camera image of AAO template obtained.

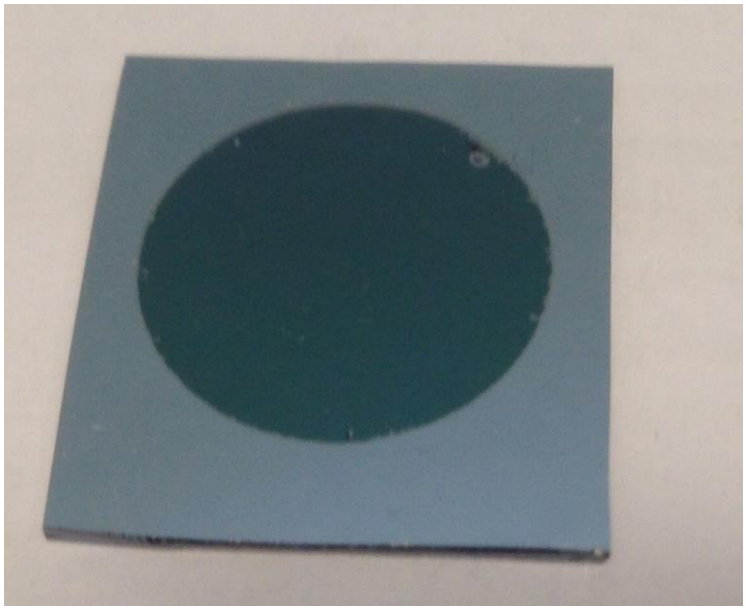

Figure 5. 3: The photo of the elaborated AAO membrane

## 5.4 Characterization of AAO template

The microscopy observations were made with a scanning electron microscope (SEM). Microscopy snapshots allow us to directly observe the morphology of the membrane. The observation of the surface (Figure 5. 5) allows us to plot the pore diameter distribution histogram, conclude the average pore diameter, and the average distance between two pores. To have access to the thickness of the pores, it is necessary, before proceeding to the observation, to cut the membrane in two pieces or more.

The SEM measurement parameters used to analyze the top surface of the AAO template are shown in figure 5. 4.

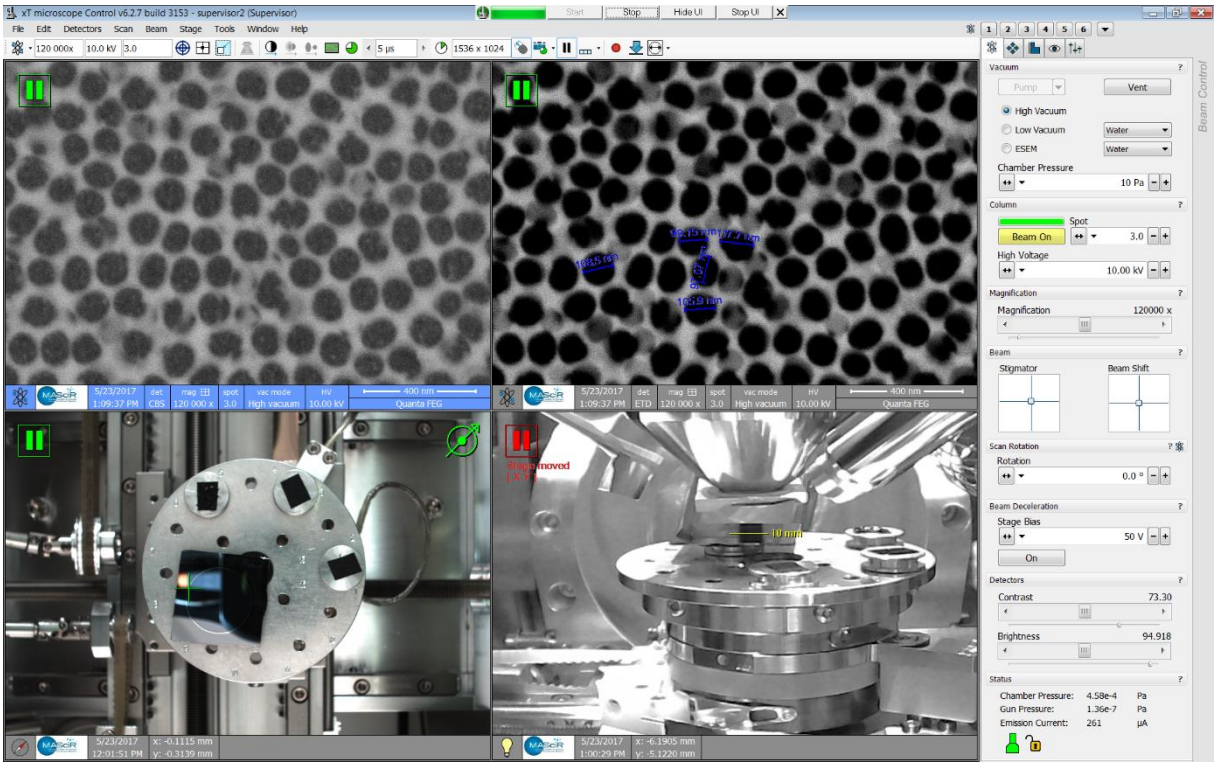


Figure 5. 4: SEM measurement parameters

The resulting alumina membranes have cylindrical pores, uniform diameter, and organized into hexagonal cells (Figure 5. 5). Generally, they are defined by a number of parameters (Figure 5. 6) such as the interpore distance ($D_{int}$), the pore diameter ($D_p$), the wall thickness ($T_w$), and the porosity (P).

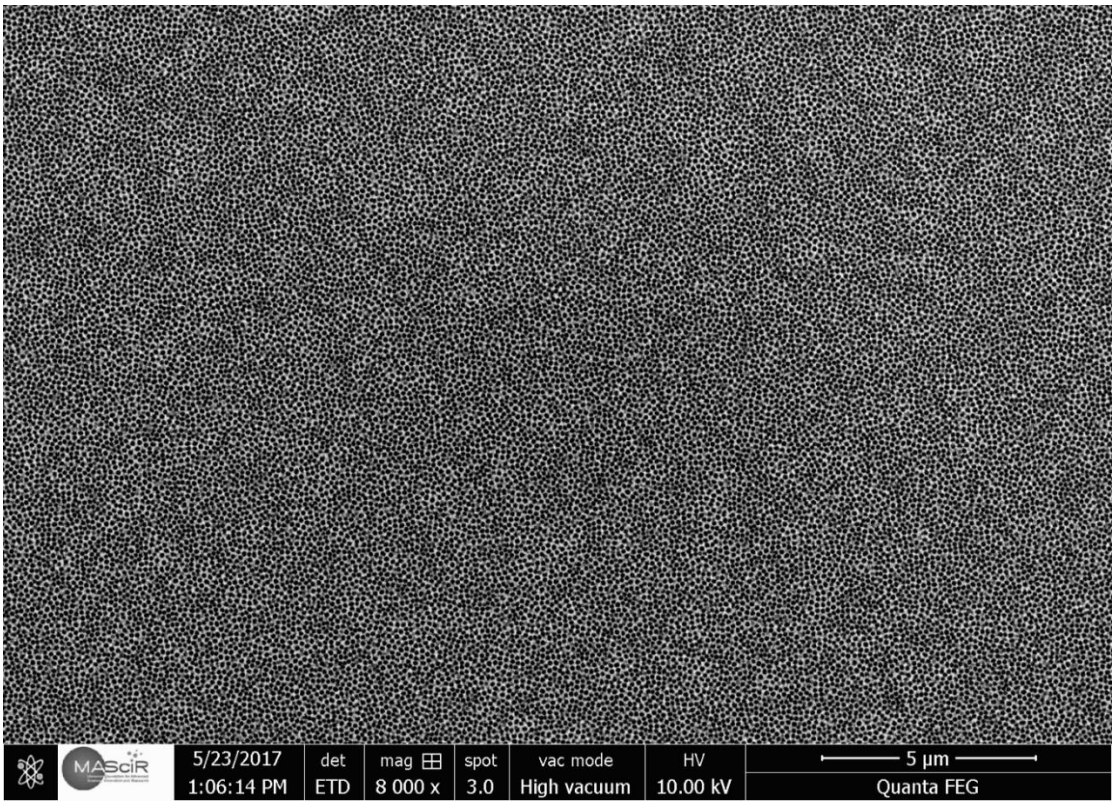


Figure 5. 5: Top view SEM image of AAO template.

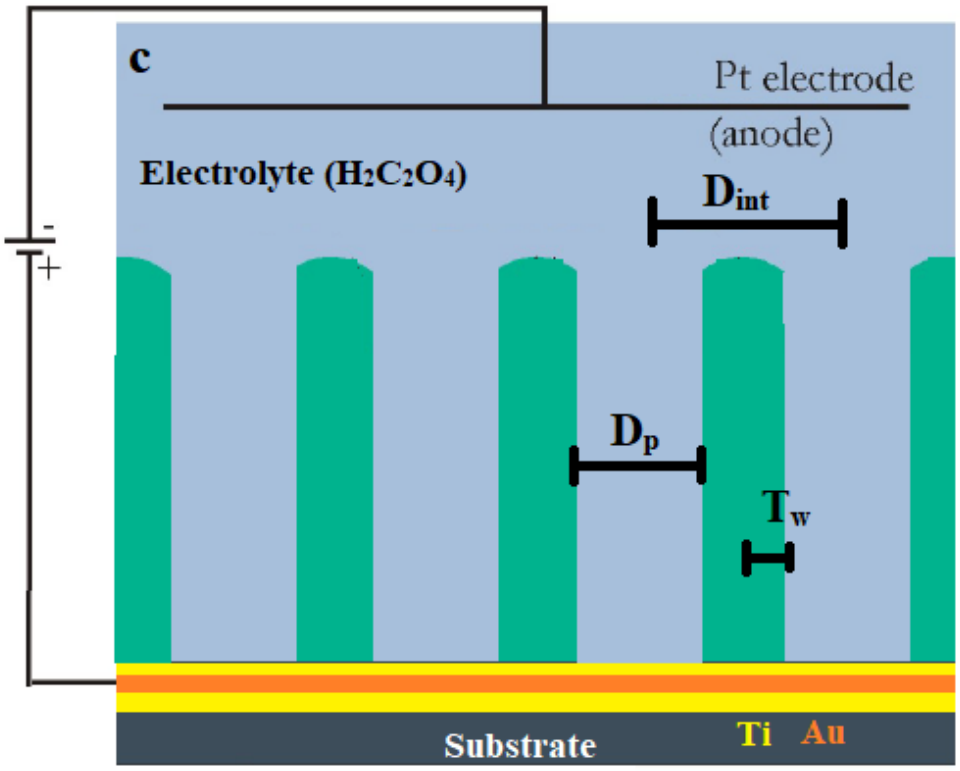


Figure 5. 6: Structural parameters of AAO template

By simple geometrical consideration, the following relations can be established :

$$D_{int} = D_P + 2T_W$$

$$P(\%) = \left(\frac{\pi}{2\sqrt{3}}\frac{D_P}{D_{int}}\right) * 100$$

Where $D_{int}$ and $D_p$ in nm and $\rho_p$ in $cm^{-2}$.

These structural parameters are dependent on the conditions of anodization, in particular of the used electrolyte (temperature, concentration …), electrical parameters (constant voltage, current density) and substrate (purity, surface state). Thus, the pore diameters of the anodic membranes can vary from 10-400 nm, and for the inter-pore distance, its vary from 50 to 600 nm. However, for the porosity, the variation range is from 5% to 70% [99][100].

Top view SEM image of the alumina template after the anodization procedure is shown in Figure 5. 7. This image allows us to directly observe the morphology of the membranes, access to the average pore diameter, the wall thickness, and the average distance between two pores.

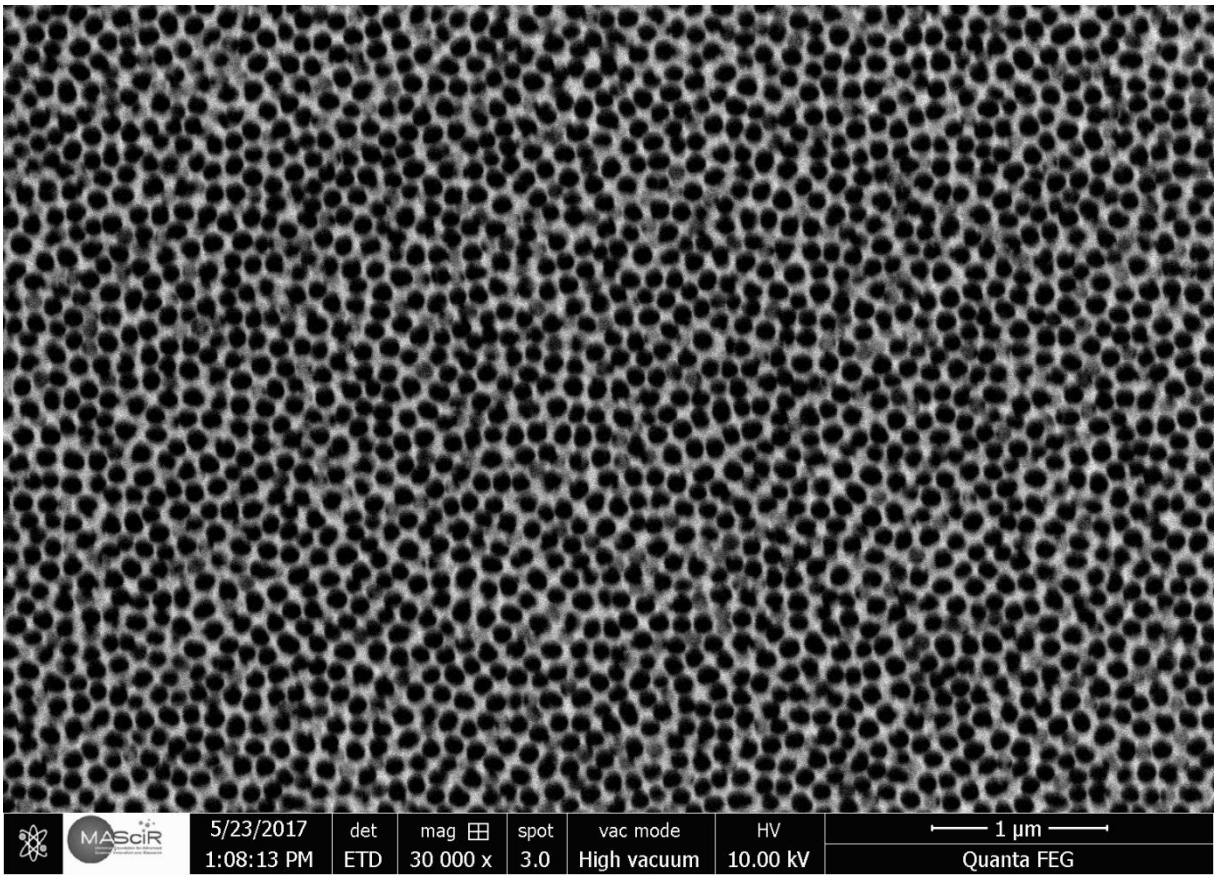


Figure 5. 7: Top view SEM image of AAO template

The analysis of SEM images using ImageJ software can be used to evaluate pore diameter by likening them to disks. In our case, this software proves to be a valuable tool to evaluate a

possible shrinkage or clogging of pores. The pore diameter distribution histogram (Figure 5. 8) obtained from 1790 pores analyzed shows that the average pore diameter is 92.39 ± 16.15 nm. The wall thickness ($T_w$) measured manually from the SEM image is around 15 nm. So, by using the relations above and the measured $D_p$ and $T_w$, this elaborated template has a porosity of about 68.4% and the interpore distance is around 122 ± 16.15 nm.

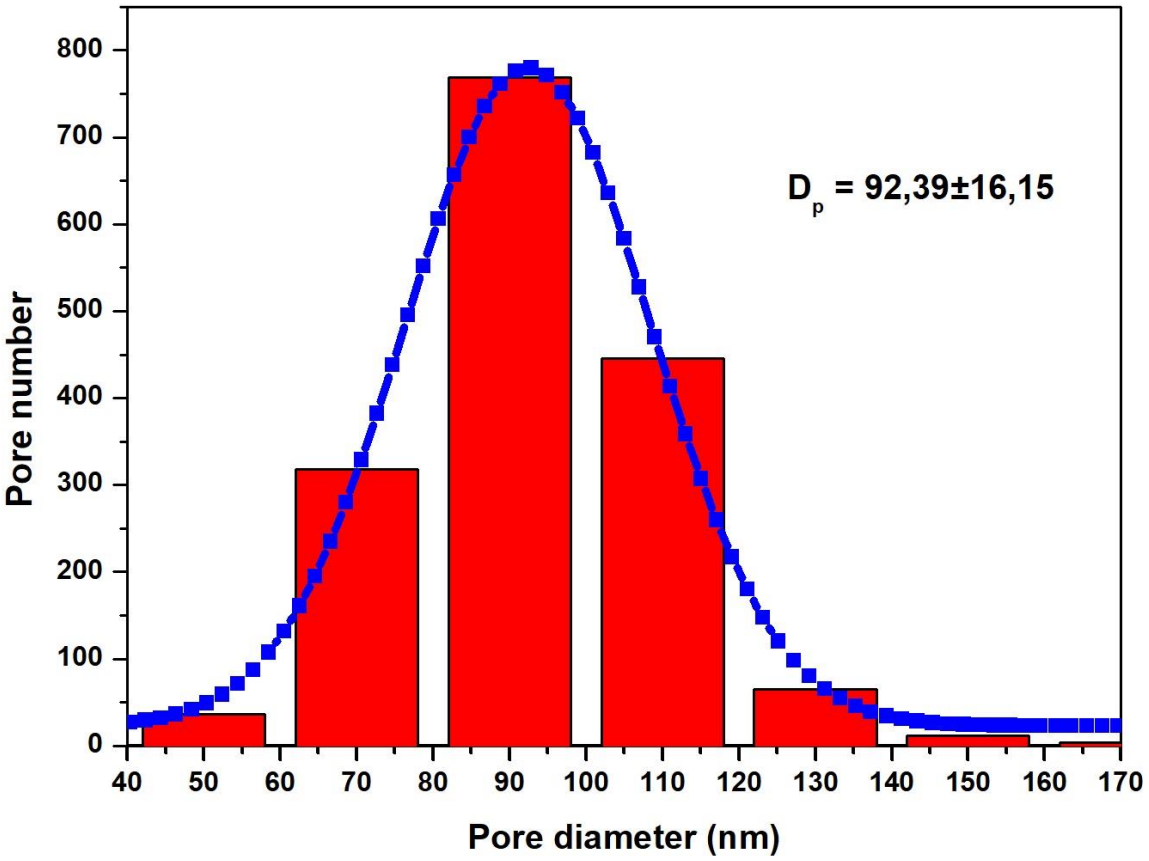


Figure 5. 8: Pore diameter distribution histogram

However, the cross section SEM image allows us to measure the thickness of the pores membrane (Figure 5. 9). The measured value of the thickness of the pores membrane is about 650 nm.

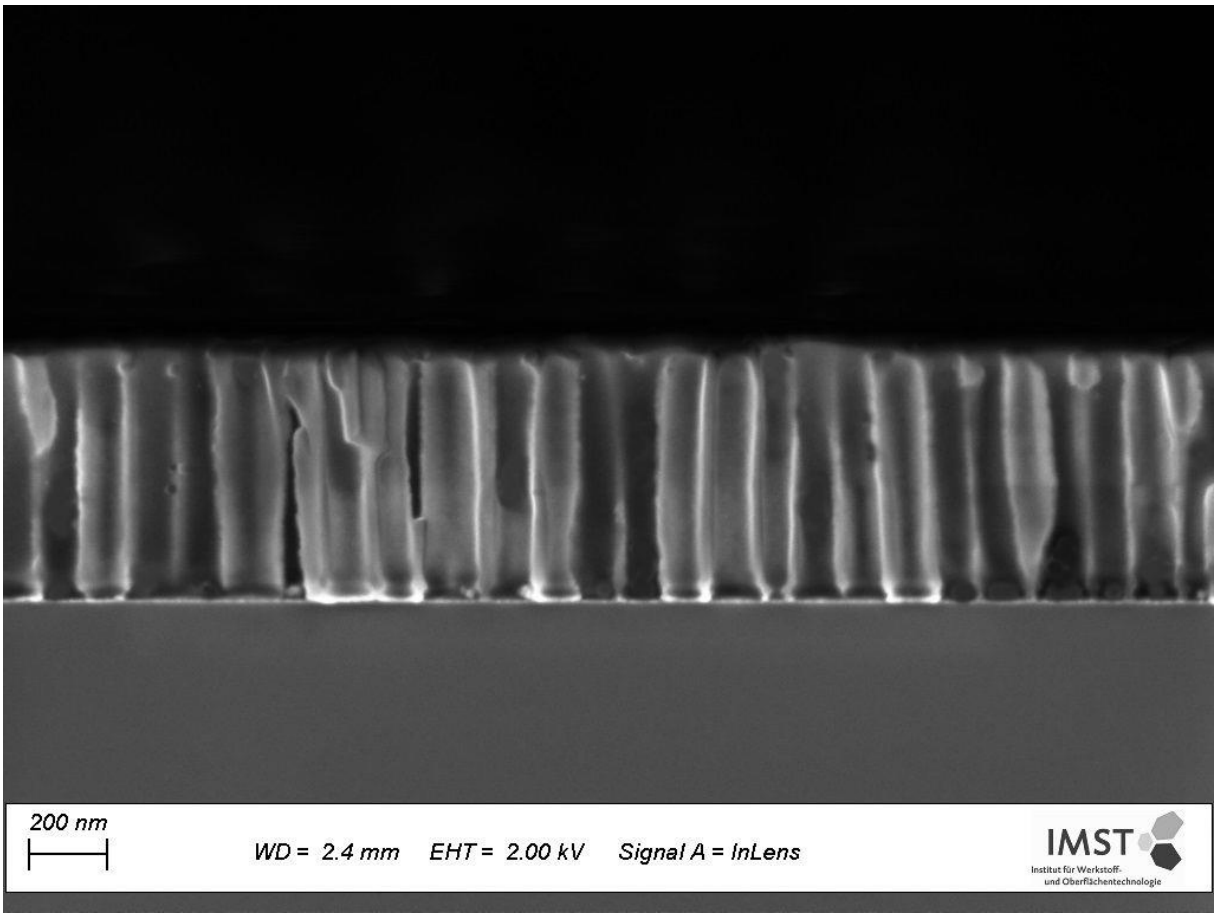


Figure 5. 9: Cross-section SEM image of AAO template

## 5.5 Insertion of cobalt ferrite nanoparticles into alumina membrane pores

In this section, we present the use of alumina membranes to transform $CoFe_2O_4$ nanoparticles to $CoFe_2O_4$ nanorods. Numerous examples relating to the preparation of nanorods, nanotubes or nanowires in alumina membranes have been reported in the literature. A wide variety of nanostructures have been obtained, like metals nanotubes, and semiconductors nanowires [101][102]. The most commonly used techniques are Atomic Layer Deposition (ALD), and chemical or physical vapor deposition (CVD or PVD) [103]. Unfortunately, these techniques need expensive equipment and special conditions of high vacuum. However, the method that we will use in this thesis is simple and less expensive.

Our method for the transformation of $CoFe_2O_4$ nanoparticles to $CoFe_2O_4$ nanorods is to synthesis, in the first, monodisperse $CoFe_2O_4$ nanoparticles then to make them highly monodisperse in hexane by using sonication. All synthesis and characterization details of $CoFe_2O_4$ nanoparticles are shown in chapter 4, the nanoparticles used in this section are the nanoparticles synthesized with optimized conditions. The STEM image and its size distribution

histogram are shown in the figure below. The nanoparticles are highly dispersed and its average size is 10.7 nm.

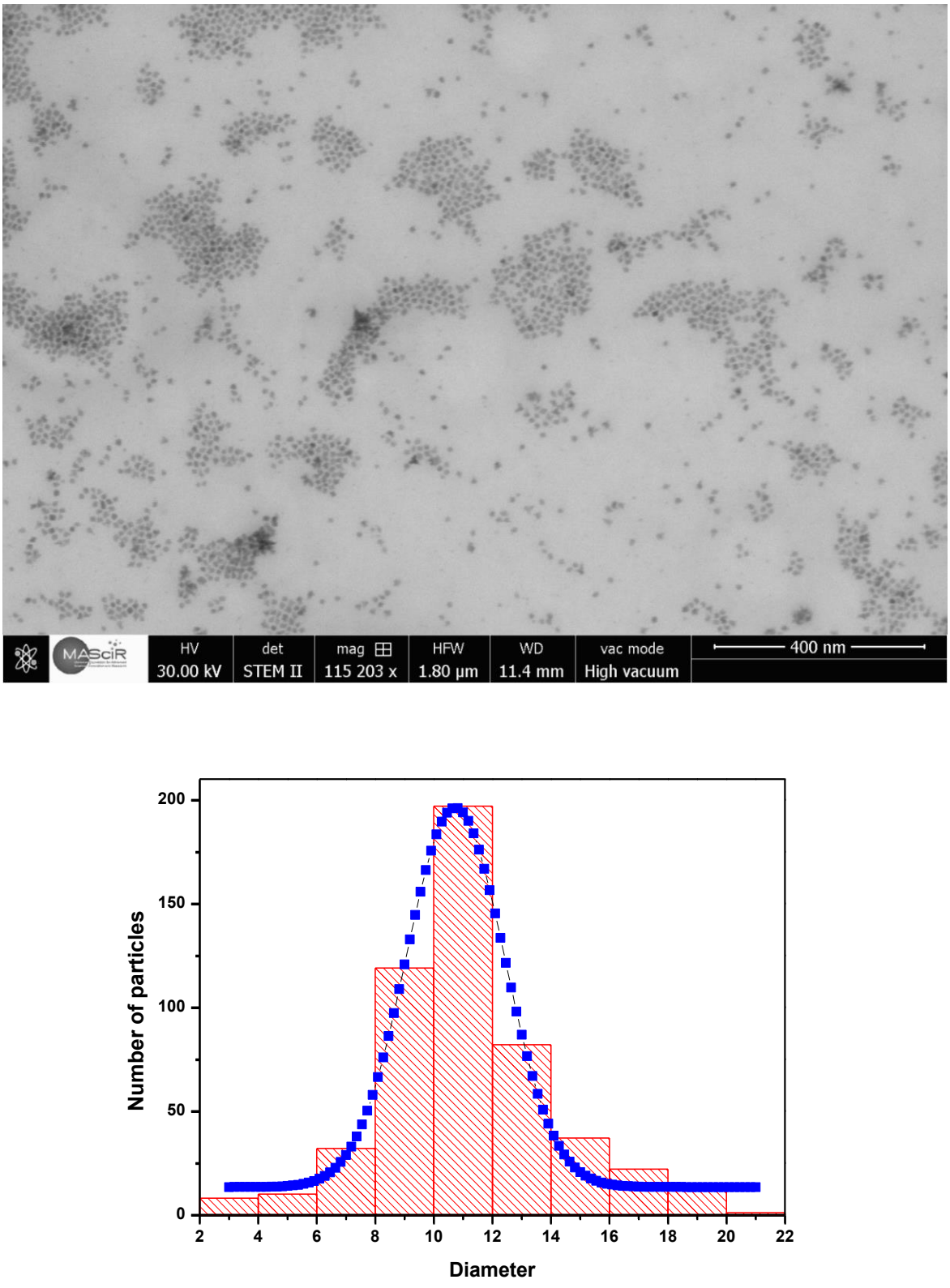


Figure 5. 10: STEM image of synthesized $CoFe_2O_4$ nanoparticles and its size distribution histogram

After getting monodisperse $CoFe_2O_4$ nanoparticles, in a bottle of 100 ml, the alumina membrane is placed in the bottom. Then, the bottle is placed on a permanent magnet (0.5 T). The solution which contains $CoFe_2O_4$ nanoparticles is poured into the bottle. The permanent magnet will force the penetration of the magnetic nanoparticles into the pores of the membrane. After a few hours, the majority of pores will be filled with magnetic nanoparticles. The alumina membrane which is filled now with magnetic nanoparticles is withdrawn from the bottle. After one hour at room temperature, all the solvents will evaporate. An annealing step at 400 ° C for 2 hours is required to remove the organic layers surrounding $CoFe_2O_4$ nanoparticles. In addition to the organic layer removing, the annealing step merges the nanoparticles between each other to become nanorods.

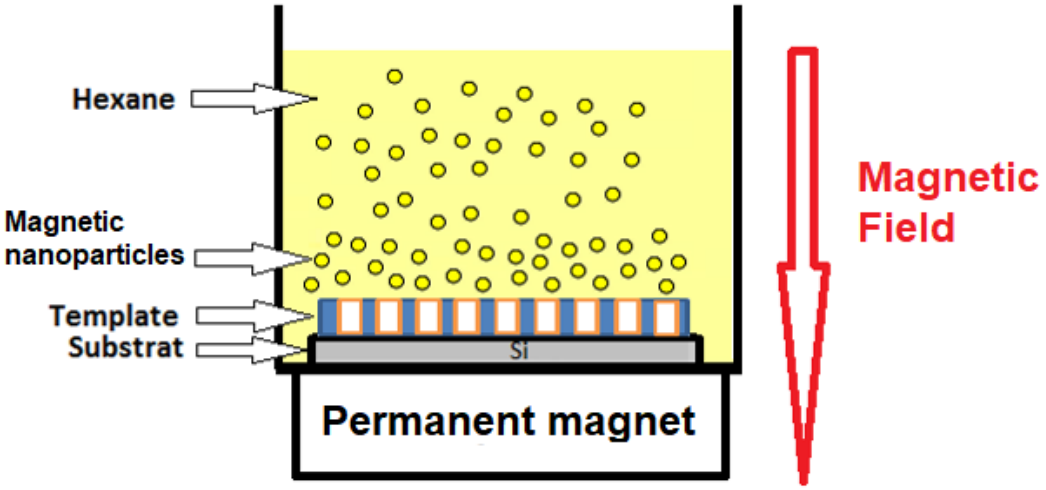


Figure 5. 11: Illustration of the insertion method of CoFe2O4 nanoparticles into alumina membrane pores.

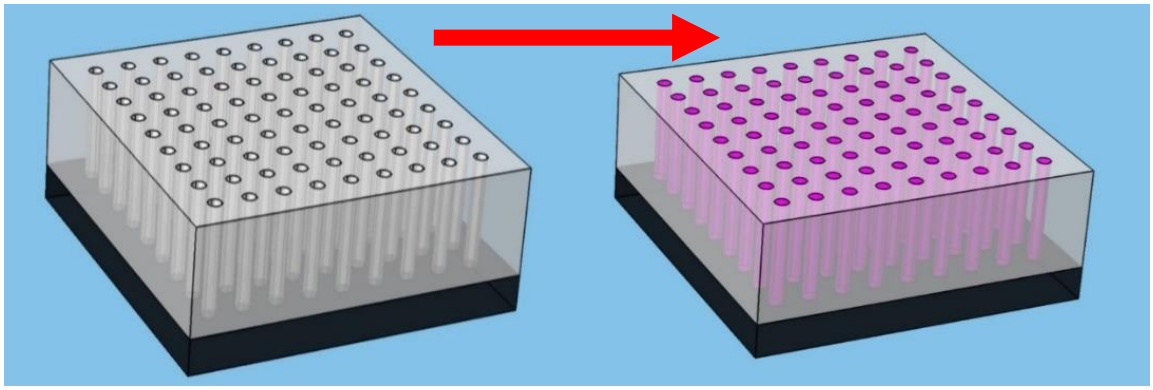

Figure 5. 12: Alumina membrane pores before and after the insertion of nanoparticles

### 5.5.1 Before annealing step

Alumina membranes were measured by scanning electron microscopy to verify the penetration of nanoparticles into membrane pores. A transverse view of a porous alumina membrane on which the nanoparticles have been deposited on its surface is given in Figure 5. 13. As can be seen from the figure, the majority of pores are filled with $CoFe_2O_4$ nanoparticles.

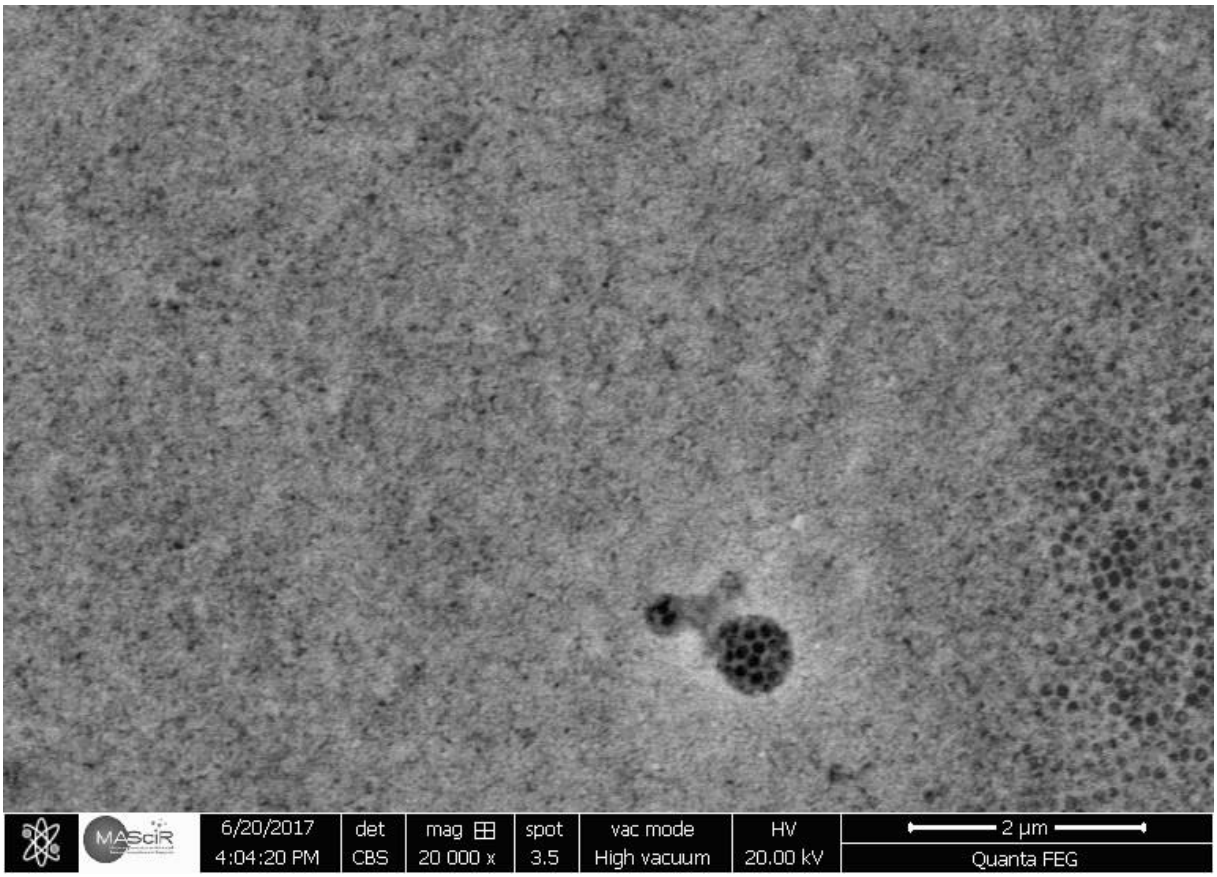


Figure 5. 13: Top view SEM image of both $CoFe_2O_4$ nanoparticles and AAO template

Figure 5. 14, represents the results of the penetration of the $CoFe_2O_4$ nanoparticles in the pores of the aluminum membrane under a magnetic field. It can be observed on all the image that there are cylinders filled with nanoparticles. The presence of these filled pores confirms that the monodispersed $CoFe_2O_4$ nanoparticles are inserted into the pores of the alumina membrane under a magnetic field of about 0.5 T. From this figure, it can be said that the filling coefficient is very high (between 80 and 95%). Also, it can be seen that there is some nanoparticles are out of pores (bottom side of $Al_2O_3$ layer). There are two reasons for that, the first reason is when the AAO template was cut for SEM measurements the nanoparticles got out of the pores; the second reason is that the nanoparticles and the AAO template have not yet annealed (the annealing step makes the nanoparticles more solid).

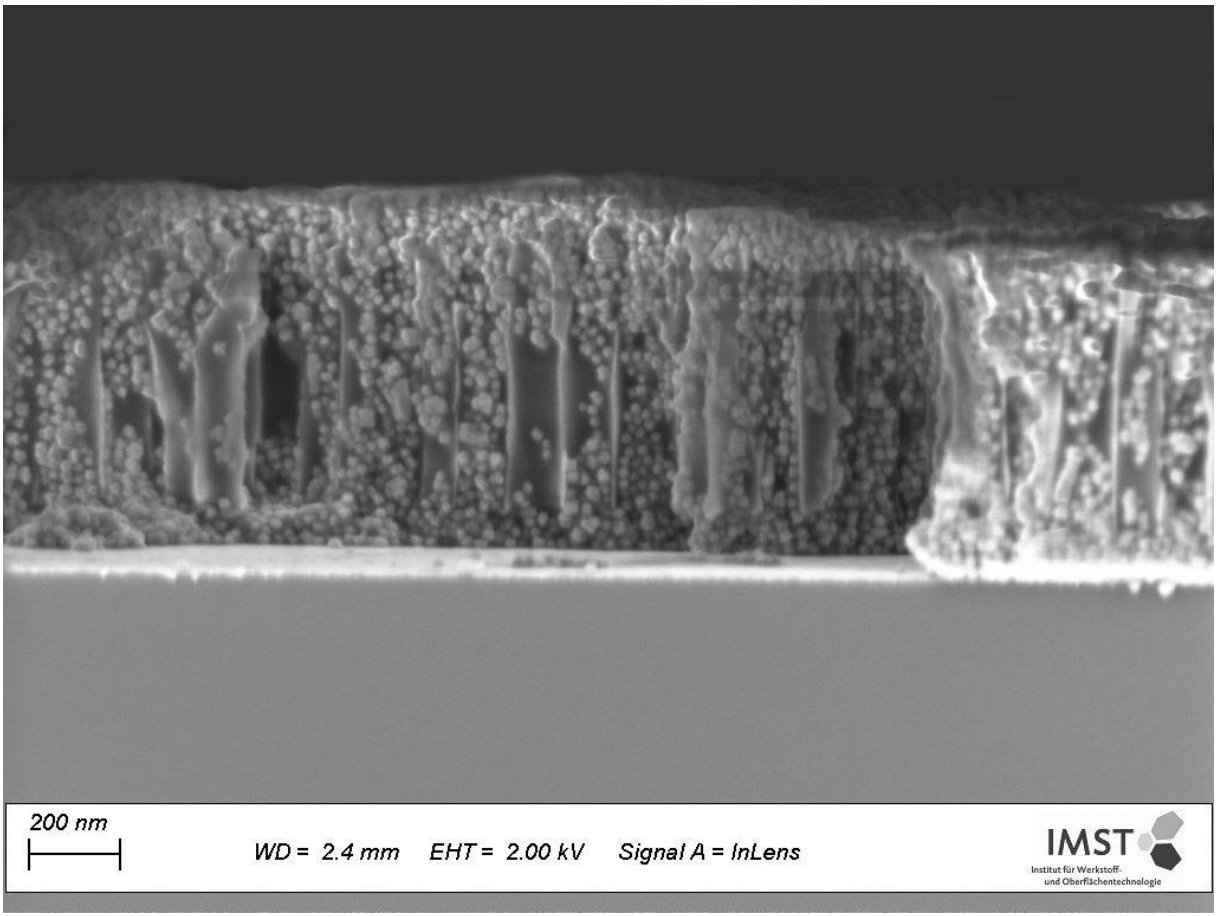


Figure 5. 14: Cross-section SEM image of $CoFe_2O_4$ nanoparticles inside alumina membrane pores

### 5.5.2 After annealing step

After annealing both $CoFe_2O_4$ nanoparticles and AAO template at 400°C for 2 hours, the organic layer surrounding nanoparticles should be removed, and the nanoparticles should be merged between each other and become nanorods. Figure 5. 15 shows the SEM image of $CoFe_2O_4$ nanoparticles inside alumina membrane pores afters annealing step. As can be seen in figure 5. 15, due to the influence of the heat treatment, the nanoparticles are well merged and become more solid and take nanorods shape. Recall that in chapter 4, it was found that the thermal annealing at 400°C for 2 hours does not affect the crystalline structure of $CoFe_2O_4$ structure. The average diameter of $CoFe_2O_4$ nanorods measured from the figure below using ImageJ software is around 85 nm which is close to the diameter of the pores of the alumina membrane.

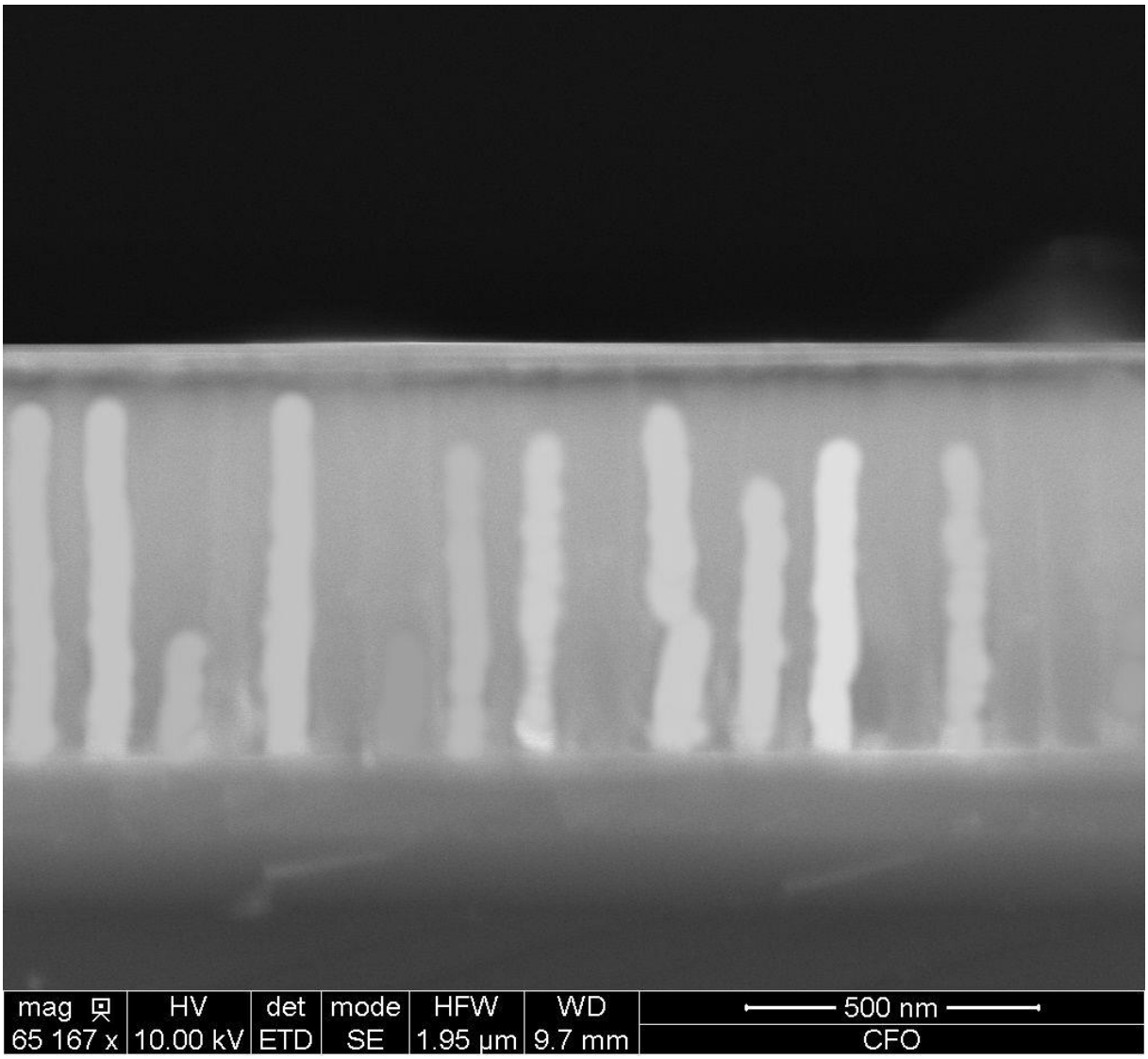


Figure 5. 15: Cross-section SEM image of $CoFe_2O_4$ nanorods.

## 5.6 Conclusion

In this chapter, we have shown the realization of a new method to transform $CoFe_2O_4$ nanoparticles to $CoFe_2O_4$ nanorods by using the AAO template. This method, easy to develop and cheap. The SEM observations of AAO template in top view and cross-section modes gave access to different information on the morphology and the height of the pores. We have studied the mechanisms of the insertion of magnetic nanoparticles into the pores of alumina membrane with applying an external magnetic field. The results obtained by SEM measurements showed that the insertion of nanoparticles was done successfully and the impact of the annealing step to change the shape of material from nanoparticles to nanorods.

The results obtained highlight the perfect feasibility of the implemented process and similar studies can be extended to other materials.

# Conclusions

Today, for the applications of nanoparticles, such as magnetic recording, sensors or hyperthermia, the materials used must have specific magnetic properties. The principal objective of my thesis was to synthesize monodisperse magnetic nanoparticles with a specific size and shape. Then, transform these nanoparticles to nanorods using AAO Template. Different Cobalt ferrite nanoparticles were synthesized. The thermal decomposition at high temperature made it possible to obtain monodisperse nanoparticles of controlled size and morphology. These nanoparticles are surrounded by an organic layer and stabilized as ferrofluid in an organic solvent (Hexane). However, due to the ligands on the surface of the nanoparticles, they could be inserted into the pores of alumina membranes. By modifying the parameters of the synthesis such as the amount of surfactants, the reaction volume, the duration of the heat treatment, or the temperature of the final stage, we were able to modify the size and shape of the nanoparticles obtained. The magnetic properties of monodisperse nanoparticles according to their size were compared. The influence of solvent, surfactant, reductant and synthetic conditions was studied as well as the influence of organic layer surrounding nanoparticles on magnetic properties of nanoparticles obtained with optimized conditions.

Porous alumina membranes seem to open new ways for the development of nano-objects. The main advantage of porous alumina consists of a geometric structure (pore size, inter-pore distance, and pore depth), easily controllable according to anodizing conditions. In the case of using membranes as a template, by deposition the materials inside the pores, it is possible to obtain a complex structure of nanorods. We have used these membranes to transform cobalt ferrite nanoparticles to nanorods. We have shown the realization of a new method to insert the nanoparticles into the pores with the help of an external magnetic field, followed by the SEM measurement before and after a step of heat treatment. The heat treatment step is necessary to make the nanoparticles more dense and solid. In this way, when the template will be removed the nanorods keep their geometry. Results obtained by SEM measurements show that the insertion of nanoparticles has done successfully. With annealing step, the nanoparticles become solid and dense nanorods.

Finally, this thesis proposes a new technique for organizing nano-objects and provides support with many advantages for the study of nanostructures.

# Résumé de la thèse en Français

## 1. Résumé

Dans le présent travail, les nanoparticules monodisperses à base de ferrite de cobalt ont été explorés pour leurs propriétés magnétiques et leur effet magnétostrictif, ainsi que pour une utilisation en tant que ferrofluide. Les nanoparticules ont été dispersées avec succès dans un solvant organique. La chimie de surface de la nanoparticule magnétique s'avère cruciale pour obtenir une dispersion haute densité homogène et bien séparée dans l'hexane. De plus, l'acide oléique a été utilisé pour modifier la surface des nanoparticules de ferrite de cobalt et permettre d'obtenir une bonne dispersion. Les nanoparticules obtenues sont caractérisées par XRD, spectroscopie Raman, TGA, FT-IR, DLS, SEM et la caractérisation magnétique. En utilisant l'analyse STEM, nous avons constaté que la taille et la forme des nanoparticules pouvaient être contrôlées en faisant varier certains paramètres tels que la température de synthèse, la quantité et la nature des réactifs. En outre, des membranes anodiques poreuses à pores très ordonnés ont été fabriquées avec succès avec une anodisation en plusieurs étapes. Des nanorods de ferrite de cobalt ont été produites par la transformation des nanoparticules de $CoFe_2O_4$ à l'aide d'une membrane d'alumine poreuses. L'insertion des nanoparticules de $CoF_2O_4$ dans les pores des membranes a été étudiée par le microscope électronique à balayage, et il a été possible de suivre le comportement des nanoparticules de $CoFe_2O_4$ dans les pores lors de l'insertion ainsi que lors de la transformation.

**Mots clés :** Ferrite de cobalt, nanoparticules monodisperses, décomposition thermique, membranes d'alumine, nanorods.

## 2. Introduction générale

De nos jours, les nanotechnologies couvrent un grand nombre de domaines technologiques dont le dénominateur commun est la taille nanométrique des structures. En fait, il s'agit d'un sujet de recherche majeur, tant pour les sciences fondamentales que pour les applications industrielles, qui fait largement appel au développement des nano-objets. En raison de leurs propriétés originales, les nanomatériaux permettent des innovations dans divers domaines. En effet, il existe un large éventail d'utilisations potentielles des nanomatériaux dans différents domaines et pour diverses applications physiques, chimiques, médicales et biologiques. Leur

développement permet également de réaliser un gain de productivité significatif et d'ouvrir de nouvelles perspectives en ayant accès à des technologies innovantes.

La forte demande des nouvelles technologies a incité les chercheurs à explorer des approches novatrices en matière de développement de matériaux multifonctionnels. À l'échelle nanométrique, les propriétés physiques (optiques, électroniques, magnétiques, etc…) des particules sont uniques et présentent un intérêt particulier, car ils sont fortement dépendants des effets quantiques liés à leur taille réduite. En fait, lorsque la taille du matériau devient nanométrique, des phénomènes particuliers liés au confinement quantique peuvent avoir lieu. Récemment, des différences entre les propriétés magnétiques d'un matériau massif et d'un nanomatériau montrent que la réduction de la taille implique de profonds changements dans les propriétés magnétiques. Étant donné que les nanoparticules ont un rapport surface / noyau central très élevé, les effets de surface ou d'interface entraînent des modifications significatives des valeurs moyennes des anisotropies et des moments magnétiques. Sur ces effets, les caractéristiques intrinsèques telles que les températures de transition magnétique (température de Curie et température de Neél) peuvent fortement dépendre de la taille et de la morphologie des nanoparticules. Ainsi, en contrôlant la taille, la forme, la composition et la structure des nanoparticules, nous parvenons à contrôler les caractéristiques magnétiques du matériau, ce qui est l'intérêt principal de nombreuses applications.

Dans ce travail, nous nous sommes intéressés aux nanomatériaux à base de ferrites de structure spinelle. Ils ont déjà de nombreux domaines d'application, en raison de leurs propriétés magnétiques originales, de leur faible coût de synthèse, par rapport à des matériaux magnétiques mieux connus à base de métaux précieux. Les applications les plus courantes sont les supports d'enregistrement magnétique, la spintronique, l'administration de médicaments à commande magnétique, les capteurs et l'hyperthermie.

Les nanoparticules magnétiques à structure spinelle $MFe_2O_4$ (M = Fe, Co, Mn, Zn, Ni ...) ont été largement étudiées pour leurs applications variées allant du stockage d'informations aux applications biomédicales. Parmi ces applications, certaines des plus récentes basées sur les propriétés magnétiques des nanoparticules sont en pleine expansion, telles que les supports d'enregistrement magnétiques ou l'hyperthermie, qui nécessitent des nanoparticules magnétiques de taille, morphologie et composition chimique contrôlées.

Afin de synthétiser des nanoparticules de ferrite de cobalt, plusieurs méthodes ont été développées, notamment la hydrothermale, les méthodes sol-gel et la co-précipitation, mais la décomposition thermique des complexes métalliques en présence de ligand semble actuellement la plus prometteuse pour assurer le contrôle de la taille, de la forme et de la composition des nanoparticules. De plus, les nanoparticules synthétisées par ce procédé sont recouvertes par une couche organique de ligands, ce qui garantit leur bonne stabilité colloïdale dans les solvants organiques.

Néanmoins, le problème du développement de nanoparticules magnétiques de haute qualité constitue un véritable défi. En effet un matériau présentant à la fois une homogénéité en taille et une dispersion est rarement rapporté dans la littérature. De plus, il existe un sérieux problème de reproductibilité, notamment en ce qui concerne la synthèse réalisée par décomposition thermique de précurseurs organométalliques dans des solvants organiques. En ce qui concerne les méthodes de préparation des nanorods, elles ont souvent des limites. Au cours de ce présent travail, nous avons utilisé une méthode originale de synthèse de nanorods magnétiques (unidimensionnelle). Elle nous a permis de produire un grand nombre de nanorods sans le problème d'agrégation souvent rencontré dans d'autres techniques de synthèse.

L'étude avancée des nanoparticules par les techniques de caractérisation habituelles (DRX, EDS, Raman, SEM, STEM, ATG, FT-IR ...) nous a permis de collecter toutes les informations nécessaires à la compréhension de leurs propriétés physiques ainsi que de la couche organique les entourant. Nous soulignons ici que nous avons entrepris une étude avancée dont le but est d'étudier l'influence des conditions synthétiques, l'influence de la couche organique et l'influence de la taille sur les propriétés physiques des nanoparticules élaborées.

Par ailleurs, nous nous sommes intéressés également à utiliser des membranes d'alumine nano-poreuses pour synthétiser un réseau régulier de nanorods de $CoFe_2O_4$. Il faut noter que depuis de nombreuses années, l'intérêt se porter sur les membranes d'alumine nano-poreuses pour la synthèse de nano-objets. Ces membranes ont des pores très verticaux, organisés en réseau hexagonal.

C'est dans ce contexte et au cours de cette thèse, des composites de type 1-3 nanorods sont choisis comme schéma de connectivité. Plusieurs méthodes et approches ont été proposées et discutées initialement pour transférer des nanoparticules de $CoFe_2O_4$ aux nanorods en utilisant les membranes d'alumine nano-poreuses.

L’idée retenue était d’incorporer et de solidifier des particules magnétiques sphériques de $CoFe_2O_4$ d’une taille inférieure à 20 nm dans une membrane d’alumine poreuse synthétisée au préalable. Dans cette configuration, toutes les particules magnétiques sont orientées selon un champ magnétique externe et conservées dans cette orientation même sans champ magnétique après la solidification de la matrice. La procédure consiste en trois étapes préparatifs préliminaires. Tout d'abord, avoir des nanoparticules de $CoFe_2O_4$ bien dispersées dans un solvant (hexane), permettant ainsi de passer de l'état liquide (nanoparticules de $CoFe_2O_4$ entourées par une couche organique et bien dispersées dans l'hexane) à l'état solide (seulement les nanoparticules de $CoFe_2O_4$). Deuxièmement, l’incorporation des nanoparticules de $CoFe_2O_4$ dans les pores de la membrane d’alumine. La Troisième étape consiste au traitement thermique nécessaire pour évaporer tous les composés organiques. Nous soulignons ici que l'insertion de nanoparticules a été réalisée à l'aide d'un champ magnétique externe.

Dans l’ensemble de ce travail de thèse, le manuscrit est divisé en cinq chapitres. Dans un premier temps, les nanoparticules de ferrites et leur structure cristalline sont présentées, ainsi que leurs propriétés magnétiques. Dans le deuxième chapitre, divers procédé de synthèse de nanoparticules de ferrite sont discutés sur la lumière des travaux menés. Le troisième chapitre présentait les techniques de caractérisation que nous avons utilisées pour caractériser les nanoparticules de ferrite synthétisées. Le chapitre quatre était consacré aux détails expérimentaux de la méthode de décomposition thermique ainsi qu'aux caractérisations chimiques et physiques des nanoparticules de $CoFe_2O_4$ obtenues. Au dernier chapitre, l’élaboration de membranes d’alumine, la caractérisation de la membrane d’alumine poreuse et l’insertion des nanoparticules de ferrite de cobalt dans les pores de la membrane d’alumine étaient examinés en détail.

## 3. Résumé du Chapitre 1

Les propriétés magnétiques des nanoparticules sont influencées par de nombreux paramètres, notamment leur taille, leur forme, leur composition chimique, leur structure cristalline et leurs interactions interparticulaires [104].

Généralement, les matériaux magnétiques se trouvent partout : dans les sols, les plantes, les animaux et même dans le cerveau humain. Particulièrement, dans les matériaux magnétiques massifs, les propriétés magnétiques intrinsèques, notamment l'aimantation de saturation, le champ coercitif et la température de Curie, dépendent uniquement de leur structure chimique et cristallographique. Par ailleurs, dans le cas où ces matériaux sont sous forme des

nanoparticules, ces propriétés sont influencées par la taille finie et les effets de surface. Par conséquent, l'évolution des nanoparticules présente une réelle occasion d'étudier les propriétés magnétiques à l'échelle atomique. C'est ainsi, ces nanoparticules magnétiques présentent parfois des propriétés novatrices, notamment le superparamagnétisme, une coercivité magnétique élevée et un coefficient de magnétostriction élevé.

Il faut rappeler que le magnétisme est le résultat de moments magnétiques associés à des électrons individuels. Les moments magnétiques proviennent de deux sources principales : le mouvement orbital et le spin électronique. Le moment magnétique net est la somme de ces moments de tous les électrons.

Il est à noter aussi que la propriété magnétique d'un matériau dépend de la réponse des dipôles électroniques et magnétiques à un champ magnétique appliqué ; ceux-ci sont classés en matériaux diamagnétiques, paramagnétiques, antiferromagnétiques, ferrimagnétiques et ferromagnétiques.

Les propriétés magnétiques dépendantes de la taille sont généralement observées dans la gamme de quelques microns à quelques nanomètres. Dans les particules plus grosses, il existe une structure multidomaine où des régions d'aimantation uniforme sont séparées par des parois de domaine et dont l'aimantation peut être inversée par le déplacement ou le déplacement des parois de domaine. Lorsque la taille des particules diminue, ces parois deviennent énergiquement défavorables, ce qui entraîne la formation d'un seul état de domaine dans lequel tous les spins sont alignés dans la même direction. Ceci est généralement observé en quelques dizaines de nanomètres, connu sous le nom du diamètre critique $D_C$ [105].

Concernant la coercivité d'un matériau, elle est définie comme le champ magnétique nécessaire pour que l'aimantation revienne à zéro après la saturation ; elle dépend de la taille. Initialement, la coercivité augmente avec la diminution de la particule jusqu'à atteindre un diamètre critique. Cela est dû au fait que le changement de la magnétisation ne peut pas être obtenu par le mouvement de la paroi du domaine qui nécessite normalement un champ magnétique faible.

Les nanoparticules sont dites en superparamagnétisme lorsque l'aimantation des nanoparticules est un seul moment magnétique géant dans chaque particule au lieu du moment atomique individuel [106]. Ce comportement peut être expliqué en termes d'anisotropie magnétique définie comme la dépendance de propriétés dans une direction préférentielle. Notons qu'en raison de l'anisotropie magnétique de la nanoparticule, le moment magnétique n'a généralement que deux orientations stables séparées par une barrière d'énergie. À une température donnée, il

est possible que l'aimantation bascule et change d'orientation. Le temps entre deux retournements est appelé temps de relaxation de Néel.

Dans ce contexte, les nanoparticules de ferrites de spinelle sont d'un grand intérêt en science fondamentale, en particulier pour traiter les relations entre les propriétés magnétiques et leur chimie cristalline. La chimie cristalline montre comment la formule chimique, la structure interne et les propriétés physiques sont liées. Les nanoparticules de ferrites ont la formule générale $MFe_2O_4$ (où M est un cation divalent et pourrait être Fe, Co, Mn, Zn, Ni, Cr). En modifiant la composition du cation divalent, ses propriétés électriques et magnétiques diffèrent. Elles trouvent des applications dans différents domaines, notamment l'enregistrement magnétique, le biomédical, les systèmes de stockage, les transformateurs, le médical et le diagnostic. Ces nombreuses applications ont conduit au développement de nombreuses méthodes de synthèse et à la caractérisation de ces nanoparticules.

Les ferrites ($MFe_2O_4$) sont structurellement classées en spinelles et peuvent être décrits comme un arrangement cubique compact d'atomes d'oxygène avec un cation divalent ($M^{2+}$) et un cation trivalent ($Fe^{3+}$) en deux sites cristallographiques différents. Notamment, les sites tétraédriques (A) et octaédriques (B) qui dépendent des positions des ions oxygène dans la cellule unité et totalisent 24 sites (8 sites A et 16 sites B). Dans une structure spinelle normale, les cations divalents ($M^{2+}$) occupent les positions tétraédriques, tandis que les sites octaédriques sont occupés par les cations trivalents ($Fe^{3+}$). Un exemple courant de ferrite normale est le ferrite de zinc. Cependant, la structure devient un spinelle inverse si tous les sites A sont occupés par $Fe^{3+}$, tandis que les sites B sont occupés par $M^{2+}$ et $Fe^{3+}$. Les ferrites de magnétite et de nickel sont des exemples de spinelles inverses. Dans certains cas, il pourrait y avoir une redistribution des cations dans chaque site donnant lieu à une structure de spinelle mixte.

## 4. Résumé du Chapitre 2

Des nanoparticules magnétiques ont été synthétisées pour différentes compositions et phases, notamment des oxydes de fer, le ferrite de cobalt, le ferrite de zinc, le ferrite de nickel, le ferrite de chrome et le ferrite de manganèse. De nombreuses méthodes ont été utilisées pour la synthèse de ces nanoparticules de ferrite, notamment la co-précipitation, le sol-gel, la décomposition thermique, les méthodes hydrothermale, ainsi que par des méthodes biologiques.

- **La méthode Sol Gel**

Historiquement, cette technique est utilisée depuis la seconde moitié du vingtième siècle, elle est de plus en plus utilisée pour la synthèse de poudres à l'échelle nanométrique. Le principe de cette méthode est de développer un solide à partir d'une solution appelée "sol" (suspension de particules colloïdales dans un liquide) à un état solide appelé "gel", qui est un solide semi-rigide dans lequel le solvant est piégé dans le matériau solide, qui peut être colloïdal (sol concentré ou polymère). Les avantages de cette méthode sont la simplicité, la rapidité et la pureté chimique des matériaux obtenus.

Il est intéressant de mentionner que l'un des intérêts majeurs du procédé «sol-gel» est la possibilité de produire une large gamme de gels dopés par différents types de dopants tels que des particules métalliques, des ions ou des nanoparticules magnétiques (le sujet du présent travail) constituant toutefois la phase solide du ferrofluide [107]. L'insertion de dopants spécifiques par la méthode sol-gel permet la création de matériaux spécifiques, ouvrant la voie à de nombreuses applications.

Cette méthode présente plusieurs avantages et inconvénients :

- Avantages de la méthode sol-gel
- Travailler à des basses températures.
- La composition du matériau final contrôlable au niveau moléculaire
- Excellente homogénéité
- La facilité de production de systèmes complexes
- Inconvénients de la méthode sol-gel
- Long temps de processus
- Tailles et formes de particules irrégulières
- Prix de précurseur élevé

➢ **La méthode Co-précipitation**

Cette méthode est un moyen simple et pratique pour synthétiser des nanoparticules de ferrite à partir de nitrate de $Fe^{3+}$ et de nitrate $M^{2+}$ à la température ambiante ou à une température élevée. Les facteurs ayant une incidence sur la composition, la taille et la forme des nanoparticules sont les suivants : le rapport $Fe^{3+}/M^{2+}$, la température, le pH et l'addition de tensioactifs.

➢ **Les méthodes hydrothermales**

Un système hydrothermal implique l'utilisation d'eau à une température supérieure à son point d'ébullition (100 °C) sous haute pression dans une cuve autoclave fermée. Semblable aux méthodes hydrothermales, la synthèse solvothermale utilise la même technique mais avec un

solvant non aqueux. L'utilisation de températures et de pressions élevées augmente la solubilité et la réactivité des précurseurs, ce qui conduit à la production de nanoparticules très cristallines. En effet, cette méthode a été utilisée pour synthétiser différentes nanoparticules de ferrite, notamment la magnétite ($Fe_3O_4$) [108][109], ferrite de cobalt ($CoFe_2O_4$) [110], et le ferrite de nickel ($NiFe_2O_4$) [111].

- **La décomposition thermique**

Ce procédé implique le chauffage de précurseurs dans un solvant organique à haut point d'ébullition en présence des tensioactifs. Cette méthode a été utilisée pour synthétiser différentes nanoparticules et s'est révélée produire des nanoparticules monodisperses avec une distribution de taille très étroite et une bonne cristallinité. Le processus peut impliquer soit un chauffage progressif des réactifs dans un milieu approprié à la température désirée, soit un processus plus rapide appelé injection à chaud. Dans le premier cas, le milieu réactionnel contenant les précurseurs, les solvants et les tensioactifs est progressivement chauffé d'une température basse (souvent ambiante) à une température de réaction prédéfinie supérieure.

Ce dernier implique l'injection rapide de la solution des précurseurs dans un milieu chaud contenant des tensioactifs. Les deux procédés peuvent être utilisés pour produire des nanoparticules monodisperses car il existe une séparation entre la nucléation et la croissance. Par exemple, dans l'approche par injection à chaud, une solution hautement sursaturée est formée par l'injection rapide de la solution de précurseur qui conduit à une explosion de nucléation. Cela conduit à l'épuisement des monomères en solution et la chute soudaine de température, empêchant ainsi un processus de nucléation supplémentaire. Ainsi, la nucléation est séparée du processus de croissance conduisant à la croissance de nanoparticules monodisperses. Dans l'approche progressive, la réaction du précurseur se déroule lentement via la formation d'intermédiaires qui finissent par agir comme des monomères. Les monomères s'accumulent jusqu'à atteindre la limite de sursaturation où se produit une nucléation rapide, suivie d'une croissance [112].

La taille et la forme des nanoparticules sont influencées par la concentration de précurseurs, le temps de réaction, la température, la vitesse de chauffage et la quantité des tensioactifs.

Généralement, la taille des nanoparticules augmente avec la température de croissance, du fait que, cinétiquement, le taux d'addition des noyaux aux noyaux existants augmente. Cependant, plus souvent la thermolyse dans un solvant à point d'ébullition élevé donne un diamètre plus grand qu'un solvant à point d'ébullition inférieur. Cela peut s'expliquer par la réactivité plus

élevée des précurseurs dans les solvants à point d'ébullition élevé [113]. Plusieurs rapports ont également montré qu'une durée de réaction plus courte donne des particules plus petites par rapport à des temps de réaction plus longs [114], du fait de la focalisation ou de la défocalisation.

La forme des nanoparticules de ferrite peut être déterminée en contrôlant la vitesse et la température de chauffage. Des nanoparticules sphériques sont généralement obtenues lorsque la vitesse de chauffage est élevée, ce qui entraîne une nucléation rapide et un épuisement de la concentration en monomère. Il se produit donc une croissance cristalline non sélective et la formation des sphères favorisées thermodynamiquement. Cependant, avec une vitesse de chauffage plus lente, un nombre limité de noyaux se forment, laissant une concentration élevée de monomères en solution. Les monomères restants sont donc ajoutés lentement sur les quelques noyaux existants qui doivent ensuite croître dans une direction particulière, ce qui conduit à l'évolution de formes différentes telles que les cubes et les étoiles [115].

Des méthodes de décomposition thermique ont été utilisées pour synthétiser avec succès des nanoparticules de ferrite de différentes tailles et formes, notamment l'oxyde de fer [116], cobalt ferrite [117], nickel ferrite [118], ferrite de manganèse [119], et ferrite de zinc [120].

Dans le présent travail, nous avons utilisé une méthode basée sur la «décomposition thermique» pour la synthèse de nanoparticules de ferrite de cobalt. Cette méthode a été proposée par Song et al [121] pour élaborer des nanoparticules de ferrite de cobalt.

Notant que notre choix d'utiliser cette méthode est justifié par le fait que cette technique est simple et peu coûteuse. De plus, avec ce procédé, il est possible de générer des tailles de cristallites intéressantes pour des applications magnétiques, catalytiques et électroniques. En outre, il nécessite une seule réaction chimique et il n'est pas nécessaire de procéder à un recuit de cristallisation. En outre, le solvant utilisé est l'éther benzylique, connu pour sa faible toxicité et habituellement utilisé comme additif alimentaire et cosmétique.

## 5. Résumé du Chapitre 3

Dans ce chapitre, nous avons présenté les techniques d'analyse utilisées. Les échantillons sont caractérisés par diffraction des rayons X et par spectroscopie Raman pour confirmer la structure cristalline spinelle. La spectroscopie d'infra-rouge a été entreprise pour analyser la couche organique entourant les nanoparticules ; alors que l'analyse thermogravimétrique et le microscope électronique à balayage pour analyser la microstructure et identifier les éléments

chimiques présents dans les matériaux. En fin, le magnétomètre MPMS-XL7 a servi pour mesurer les propriétés magnétiques des échantillons sélectionnés.

Evidemment, la diffraction des rayons X est la technique de base pour la caractérisation des matériaux ; il permet de déterminer la phase et la pureté d'un matériau cristallin, en utilisant sa capacité à dévier le faisceau de rayons X. La diffraction des rayons X permet d'accéder à de nombreuses informations contenues dans un arrangement d'atomes dans un matériau cristallisé. Tel que le type de disposition géométrique, le paramètre de maille et la taille des nanoparticules.

Pour étudier la diffusion Raman au cours de cette thèse, un spectromètre Raman (Jobin Yvon T64000) équipé d'un monochromateur, de deux prémonchromeurs et d'une caméra CCD haute résolution refroidie à l'azote liquide. Pour l'excitation, nous avons utilisé un laser à gaz (Krypton) accordable.

Par ailleurs, l'analyse thermogravimétrique est l'une des méthodes d'analyse thermique mise au point pour étudier les modifications thermique du matériau. Il consiste à mesurer l'évolution de la masse d'un échantillon lorsqu'il est soumis à une variation de température sous atmosphère contrôlée. Cette variation peut être une perte de masse en cas d'émission de vapeur ou un gain de masse comme dans le cas d'oxydation. Cette méthode nous a permis d'évaluer la quantité de résidus d'hydroxyde ou de matières organiques encore présents dans les échantillons, ainsi que la température de leur évaporation. Par conséquent, définir la température de calcination optimale pour les échantillons devant être calcinés.

Quant à la spectroscopie infrarouge à transformée de Fourier qui est basée sur l'absorption du rayonnement infrarouge par le matériau analysé, il nous a permis la détection des vibrations caractéristiques des liaisons chimiques ainsi que d'effectuer l'analyse des fonctions chimiques présentes dans l'échantillon analysé.

En effet, lorsque la longueur d'onde (énergie) fournie par le faisceau lumineux est proche de l'énergie vibratoire de la molécule, celle-ci absorbera le rayonnement et l'intensité diminuera ou sera transmise. Par conséquent, un matériau ayant une composition chimique et une structure données correspondra à un ensemble de bandes d'absorption caractéristiques permettant l'identification du matériau [49].

L'analyse microstructurale  a été entreprise par le microscope électronique à balayage SEM, qui est un appareil capable de fournir rapidement des informations sur la morphologie et la composition chimique d'un matériau solide. Le SEM utilisé au cours de cette thèse est couplé à un système de microanalyse EDS (Spectrométrie Dispersive Energétique).

Les investigations des propriétés magnétiques des ferrites constituent une grande partie de cette thèse. Les mesures magnétiques ont été effectuées par Le magnétomètre MPMS-XL7 pour sonder les propriétés magnétiques des échantillons préparés.

Le dispositif d'interférence quantique supraconducteur est un système intégré permettant de mesurer et d'analyser les propriétés magnétiques de la matière. Le magnétomètre MPMS-XL7 est un appareil de mesure magnétique permettant de déterminer avec précision les propriétés magnétiques de matériaux naturels (roches, sédiments, terre cuite) et de matériaux artificiels (ferrofluides, nanoparticules, nanotubes de carbone, couches minces) sur une large plage de températures et de champs magnétiques externes. Les mesures obtenues par ce système renseignent sur la réaction magnétique du matériau sous champs magnétique et permettent de déterminer les propriétés magnétiques de ce matériau qui sont très dépendantes des conditions de mesure.

Dans ce chapitre, nous avons décrit différentes techniques et méthodes de caractérisation utilisées au cours ce travail de thèse, comme des analyses thermiques, structurelles, vibrationnelles, microstructurale et la mesure des propriétés magnétiques.

## 6. Résumé du Chapitre 4

Les nanoparticules magnétiques (NP) ont suscité un vif intérêt en raison de leurs propriétés physiques et magnétiques qui diffèrent considérablement de leurs homologues en raison de leur rapport surface/volume élevé et de leur taille comparable au domaine magnétique [50]. Ces nanostructures se sont avérées prometteuses pour des applications étendues dans plusieurs domaines, notamment les supports d'enregistrement magnétiques, la spintronique, l'imagerie par résonance magnétique (IRM), la catalyse, l'administration de médicaments à commande magnétique, les capteurs, etc [122][52][53]. Par ailleurs, les nanoparticules à base de fer et de cobalt, et en particulier le ferrite de cobalt ($CoFe_2O_4$), deviennent très attractives pour diverses applications dans les dispositifs électroniques, la catalyse, les ferrofluides, le stockage d'informations à haute densité, l'enregistrement magnétique (disques d'enregistrement numériques à haute densité) et les applications biomédicales, en raison de leur stabilité physique et chimique élevée, de leur anisotropie magnétocristalline élevée, de leur magnétisation à saturation modérée et de leur coefficient de magnétostriction élevé [54][55][123].

Afin de synthétiser des nanoparticules de ferrite de cobalt, plusieurs méthodes ont été développées, notamment la micro-émulsion, les méthodes sol-gel, la micro-onde et la co-précipitation [58], mais la décomposition thermique de complexes métalliques en présence de

ligand (comme agent de coiffage) semble être actuellement le plus prometteur pour assurer le contrôle de la taille, de la forme et de la composition des nanoparticules [60][61]. En outre, les nanoparticules synthétisées par cette méthode sont recouvertes d'une couche organique de ligands qui assurent leur bonne stabilité dans des solvants organiques.

Lors de mon arrivé à la Fondation MAScIR, ce processus n'était pas encore développé en laboratoire. Par conséquent, mon premier objectif était d'approprier cette méthode et de développer un protocole de synthèse approprié pour les nanoparticules de ferrite de cobalt.

Dans notre étude, l'objectif était d'obtenir des nanoparticules de petit diamètre (c'est-à-dire entre 5 et 20 nm) susceptibles d'être incorporées dans des membranes d'alumine poreuses. Parmi les différents travaux décrits dans la synthèse de ces nanoparticules [62][124][125], nous avons sélectionné celui rapporté par Song et al [62] qui conduit à des nanoparticules de $CoFe_2O_4$ de forme sphérique et de taille uniforme dans la gamme que nous souhaitons obtenir. Rappelons que le principe de synthèse par ce procédé repose sur la décomposition thermique d'acétylacétonates de fer et de cobalt dans un solvant organique (éther benzylique) à haut point d'ébullition (298 °C), en présence d'un agent réducteur (oléylamine et acide oléique). Au cours de ce travail, le rapport volumique oléylamine (acide oléique) / éther benzylique a été modifié pour étudier son influence sur la taille des nanoparticules.

Dans ce chapitre, nous donnons des détails sur le protocole de synthèse développé pour les nanoparticules de $CoFe_2O_4$. Ensuite, nous exposons les caractérisations chimiques et magnétiques effectuées sur diverses nanoparticules de $CoFe_2O_4$ synthétisées en faisant varier différents paramètres. Nous surlignons ici que la modification des paramètres de synthèse nous a permis de comprendre le rôle de chacun des paramètres sur la taille, la monodispersité et la morphologie des nanoparticules.

En conclusion, des nanoparticules de ferrite de cobalt de forme sphérique ont été synthétisées avec sucée en contrôlant la taille et une distribution de taille très étroite en ajustant les conditions expérimentales de décomposition thermique de complexes métalliques, la nature des précurseurs, des tensioactifs, des réducteurs et aussi des solvants. Nous avons également mis en évidence que l'utilisation d'acétylacétonate en tant que précurseurs en présence de l'acide oléique et l'oléylamine en tant que surfactants, conduit à des nanoparticules sphériques de type cœur-coquille avec $CoFe_2O_4$ au cœur et une couche organique en tant que coquille à la surface.

Nous avons montré également dans ce travail que l'obtention de telle structure cristalline est due à l'environnement réducteur gouverné par à la présence d'hydrocarbures, de groupes

carboxylates et de tensioactifs acide oléique. Le matériau obtenu a été étudiée par DRX, FT-IR et la spectrométrie Raman. En utilisant l'analyse STEM, nous avons confirmé que la taille et la forme des NP pouvaient être contrôlées par la variation de certains paramètres tels que la température de synthèse, la quantité et la nature des réactifs. De plus, les mesures par EDS, DRX et la spectroscopie Raman nous ont permis de confirmer la formation de nanoparticules de $CoFe_2O4$ à structure spinelle. De plus, l'analyse FT-IR nous a conduits à identifier la présence de groupes fonctionnels de molécules organiques entourant les nanoparticules ainsi que les modes de vibration des liaisons métal-oxygène pour la structure spinelle.

Enfin, nous avons mis en évidence le comportement superparamagnétique à la température ambiante de ces nanoparticules de $CoFe_2O_4$ avec un état bloqué à basse température (10 K). Nous avons constaté également que les propriétés magnétiques ($H_C$, $T_B$, $M_S$) dépendent de la taille et de la couche organique entourée les nanoparticules. En effet, l'augmentation de leur taille a une influence importante sur leurs aimantations de saturation ainsi que sur leur champ coercitif.

## 7. Résumé du Chapitre 5

L'effet magnétoélectrique ne se trouve intrinsèquement dans certains matériaux seulement à très basse température. L'utilisation de matériaux magnétostrictifs et piézoélectriques permet de surmonter ce problème en les couplant mécaniquement.

Une nouvelle voie consiste à concevoir des matériaux composites pouvant être qualifiés de multiferroïques «extrinsèques», associant des matériaux ferroélectriques et ferromagnétiques. Un couplage est ensuite effectué par les contraintes mécaniques entre les deux matériaux apparentés. En appliquant un champ magnétique, le ferromagnétique se déforme par effet magnétostrictif et transmet ainsi les contraintes au piézoélectrique qui modifient ses propriétés diélectriques, telles que la polarisation, et inversement. Les composites magnétoélectriques peuvent avoir divers schémas de connectivité, mais les schémas de connectivité courants sont des composites particulaires de type 0-3, constitués de grains d'oxyde magnétique piézoélectriques, de composites céramiques stratifiés de type 2-2 constitués de couches d'oxyde magnétique et piézoélectrique, et de type 1-3, composites nanorods constitués avec des nanorods d’une phase incorporés dans la matrice d’une autre phase.

Dans cette thèse, un composite de type 1-3 nanorods est choisi comme schéma de connectivité. Plusieurs méthodes et approches ont été discutées pour fabriquer ce type de nanocomposites.

Nous avons développé une nouvelle approche pour transférer des nanoparticules de $CoFe_2O_4$ à des nanorods en utilisant des membranes d'alumine poreuses.

La méthode consiste à incorporer et solidifier des particules magnétiques sphériques de $CoFe_2O_4$ d'une taille inférieure à 20 nm dans une membrane d'alumine poreuse préfabriquée. Dans cette configuration, toutes les particules magnétiques sont orientées selon un champ magnétique externe et restent dans cette orientation même sans champ magnétique après la solidification de la matrice. La procédure comprend trois étapes préliminaires. Tout d'abord, mélanger des nanoparticules de $CoFe_2O_4$ bien dispersées dans l'hexane comme solvant, permettant ainsi de passer de l'état liquide (nanoparticules de $CoFe_2O_4$ entourées d'une couche organique et dispersées dans l'hexane) à l'état solide (seulement nanoparticules de $CoFe_2O_4$). Deuxièmement, l'incorporation de nanoparticules de $CoFe_2O_4$ dans les pores de la membrane d'alumine. La Troisième étape consiste au traitement thermique nécessaire pour évaporer tous les composés organiques. Nous soulignons ici que l'insertion de nanoparticules a été réalisée à l'aide d'un champ magnétique externe.

Il convient de mentionner que les membranes d'alumine poreuses utilisées dans cette thèse ont été fabriquées à l'Institut des matériaux et des technologies de surface / IMST de l'Université des sciences appliquées de Kiel en Allemagne, au sein de l'équipe de Mohammed Es-Souni. La membrane d'alumine poreuse a été synthétisée avec un diamètre de 2 cm, une épaisseur de 650 nm et une porosité de 68%. Les pores de la membrane ont un diamètre moyen de l'ordre de 92 nm. Les nanoparticules de $CoFe_2O_4$ ont été synthétisées par la méthode de décomposition thermique. Le diamètre moyen des nanoparticules est entre 8 nm et 14 nm. Les nanoparticules sont bien dispersées dans l'hexane. Ces nanoparticules ont été préparées dans le laboratoire de Mascir.

## 8. Conclusion générale

De nos jours, pour les applications des nanoparticules, telles que l'enregistrement magnétique, les capteurs ou l'hyperthermie, les matériaux utilisés doivent posséder des propriétés magnétiques spécifiques. L'objectif principal de ma thèse était de synthétiser des nanoparticules magnétiques monodisperses de taille et de forme spécifiques. Ensuite, transformer ces nanoparticules en nanorods à l'aide d'une membrane d'alumine poreuse. Différentes nanoparticules de ferrite de cobalt ont été synthétisées par différentes méthodes. La décomposition thermique à haute température a permis d'obtenir des nanoparticules

monodisperses de taille et de morphologie contrôlées. Ces nanoparticules sont entourées d'une couche organique et stabilisées sous forme de ferrofluide dans un solvant organique (hexane). Cependant, en raison des ligands à la surface des nanoparticules, ils pourraient être insérés dans les pores des membranes d'alumine. En modifiant les paramètres de la synthèse tels que la quantité de tensioactifs, le volume de réaction, la durée du traitement thermique ou la température de l'étape finale, nous avons pu modifier la taille et la forme des nanoparticules obtenues. Les propriétés magnétiques des nanoparticules monodisperses en fonction de leur taille ont été comparées et des conclusions ont été tirées. Nous avons également étudié l'influence des conditions de synthèse, de solvant, de surfactant et de réducteur ainsi que l'influence de la couche organique entourant les nanoparticules sur les propriétés magnétiques des nanoparticules obtenues dans des conditions optimisées.

Les membranes d'alumines poreuses ouvrent de nouvelles voies pour le développement des nano-objets. Le principal avantage de l'alumine poreuse consiste en une structure géométrique (taille des pores, distance entre pores et profondeur des pores) facilement contrôlable en fonction des conditions d'anodisation. Dans le cas de l'utilisation de membranes comme moule, il est possible d'obtenir une structure complexe de nanorods en déposant les matériaux à l'intérieur des pores. Nous avons utilisé ces membranes pour transformer des nanoparticules de ferrite de cobalt en nanorods. Une nouvelle méthode pour insérer les nanoparticules dans les pores a été développée au cours de ce travail, en utilisant un champ magnétique externe. Ensuite, nous avons entrepris des analyses microstructurales au SEM avant et après le traitement thermique de ces nanocomposites élaborés. Nous notons que l'étape de traitement thermique est nécessaire pour rendre les nanoparticules plus denses et solides. De cette façon, lorsque la membrane sera retirée, les nanorods conservent leur géométrie. Les résultats obtenus par des analyses au SEM montrent que l'insertion de nanoparticules a bien réussi. En outre, avec le recuit, les nanoparticules deviennent des nanorods solides et denses.

Enfin, cette thèse propose une nouvelle technique d'organisation des nano-objets et apporte de nombreux avantages pour l'étude des nanostructures.

# References


[1] “Magnétisme - Tome I - Fondements - (EDP Sciences).” [Online]. Available: https://laboutique.edpsciences.fr/produit/9782868834638. [Accessed: 03-Apr-2019].

[2] V. Gavrilov-Isaac, “Synthèse de nanoparticules magnétiques à énergie d’anisotropie modulable,” phdthesis, Université Pierre et Marie Curie - Paris VI, 2015.

[3] N. A. Frey, S. Peng, K. Cheng, and S. Sun, “Magnetic nanoparticles: synthesis, functionalization, and applications in bioimaging and magnetic energy storage,” *Chem. Soc. Rev.*, vol. 38, no. 9, p. 2532, 2009.

[4] D. Fiorani, Ed., *Surface effects in magnetic nanoparticles*. New York: Springer, 2005.

[5] C. Cannas, D. Gatteschi, A. Musinu, G. Piccaluga, and C. Sangregorio, “Structural and Magnetic Properties of Fe $_2$ O $_3$ Nanoparticles Dispersed over a Silica Matrix,” *J. Phys. Chem. B*, vol. 102, no. 40, pp. 7721–7726, Oct. 1998.

[6] E. Tronc *et al.*, “Surface effects in noninteracting and interacting γ-Fe2O3 nanoparticles,” *J. Magn. Magn. Mater.*, vol. 262, no. 1, pp. 6–14, May 2003.

[7] V. Gavrilov-Isaac, “Synthèse de nanoparticules magnétiques à énergie d’anisotropie modulable,” p. 174.

[8] S. Bedanta and W. Kleemann, “Supermagnetism,” *J. Phys. Appl. Phys.*, vol. 42, no. 1, p. 013001, Jan. 2009.

[9] J. A. Osborn, “Demagnetizing Factors of the General Ellipsoid,” *Phys. Rev.*, vol. 67, no. 11–12, pp. 351–357, Jun. 1945.

[10] F. Bødker, S. Mørup, and S. Linderoth, “Surface effects in metallic iron nanoparticles,” *Phys. Rev. Lett.*, vol. 72, no. 2, pp. 282–285, Jan. 1994.

[11] E.-D. Ciuculescu, “Synthèse et étude des propriétés de nanoparticules magnétiques de type cœur-coquille.,” p. 207.

[12] J.-C. Bacri, R. Perzynski, D. Salin, V. Cabuil, and R. Massart, “Magnetic colloidal properties of ionic ferrofluids,” *J. Magn. Magn. Mater.*, vol. 62, no. 1, pp. 36–46, Nov. 1986.

[13] “theses.fr – Lénaïc Lartigue , Synthesis, Characterization, and Theranostic Application of Iron Based Magnetic Nanoparticles.” [Online]. Available: http://www.theses.fr/2010MON20092. [Accessed: 03-Apr-2019].

[14] E. C. Stoner, “A mechanism of magnetic hysteresis in heterogeneous alloys,” p. 44.

[15] E. Duguet, S. Vasseur, S. Mornet, and J.-M. Devoisselle, “Magnetic nanoparticles and their applications in medicine,” *Nanomed.*, vol. 1, no. 2, pp. 157–168, Aug. 2006.

[16] C. Sun, J. Lee, and M. Zhang, “Magnetic nanoparticles in MR imaging and drug delivery☆,” *Adv. Drug Deliv. Rev.*, vol. 60, no. 11, pp. 1252–1265, Aug. 2008.

[17] R. Massart, J.-C. Bacri, and R. Perzynski, “Liquides magnétiques ou ferrofluides,” p. 13, 1995.

[18] J.-P. Fortin, C. Wilhelm, J. Servais, C. Ménager, J.-C. Bacri, and F. Gazeau, “Size-Sorted Anionic Iron Oxide Nanomagnets as Colloidal Mediators for Magnetic Hyperthermia,” *J. Am. Chem. Soc.*, vol. 129, no. 9, pp. 2628–2635, Mar. 2007.

[19] Z. Mahhouti *et al.*, “Structural and magnetic properties of Co0.7Ni0.3Fe2O4 nanoparticles synthesized by sol–gel method,” *Appl. Phys. A*, vol. 122, no. 7, p. 651, Jul. 2016.

[20] F. A. Tourinho, R. Franck, and R. Massart, “Aqueous ferrofluids based on manganese and cobalt ferrites,” *J. Mater. Sci.*, vol. 25, no. 7, pp. 3249–3254, Jul. 1990.

[21] S. Neveu, A. Bee, M. Robineau, and D. Talbot, “Size-Selective Chemical Synthesis of Tartrate Stabilized Cobalt Ferrite Ionic Magnetic Fluid,” *J. Colloid Interface Sci.*, vol. 255, no. 2, pp. 293–298, Nov. 2002.

[22] T. J. Daou *et al.*, “Hydrothermal Synthesis of Monodisperse Magnetite Nanoparticles,” *Chem. Mater.*, vol. 18, no. 18, pp. 4399–4404, Sep. 2006.

[23] O. Horner, S. Neveu, S. de Montredon, J.-M. Siaugue, and V. Cabuil, “Hydrothermal synthesis of large maghemite nanoparticles: influence of the pH on the particle size,” *J. Nanoparticle Res.*, vol. 11, no. 5, pp. 1247–1250, Jul. 2009.

[24] A. Abou-Hassan, S. Neveu, V. Dupuis, and V. Cabuil, “Synthesis of cobalt ferrite nanoparticles in continuous-flow microreactors,” *RSC Adv.*, vol. 2, no. 30, p. 11263, 2012.

[25] L. Pérez-Mirabet *et al.*, “One-pot synthesis of stable colloidal solutions of MFe2O4 nanoparticles using oleylamine as solvent and stabilizer,” *Mater. Res. Bull.*, vol. 48, no. 3, pp. 966–972, Mar. 2013.

[26] Q. Song and Z. J. Zhang, “Shape Control and Associated Magnetic Properties of Spinel Cobalt Ferrite Nanocrystals,” *J. Am. Chem. Soc.*, vol. 126, no. 19, pp. 6164–6168, May 2004.

[27] C. N. Chinnasamy, B. Jeyadevan, K. Shinoda, and K. Tohji, “Polyol-process-derived CoPt nanoparticles: Structural and magnetic properties,” *J. Appl. Phys.*, vol. 93, no. 10, pp. 7583–7585, May 2003.

[28] R. Massart, “Preparation of aqueous magnetic liquids in alkaline and acidic media,” *IEEE Trans. Magn.*, vol. 17, no. 2, pp. 1247–1248, Mar. 1981.

[29] F. Tourinho, R. Franck, R. Massart, and R. Perzynski, “Synthesis and mangeitc properties of managanese and cobalt ferrite ferrite ferrofluids,” in *Trends in Colloid and Interface Science III*, vol. 79, P. Bothorel and E. J. Dufourc, Eds. Darmstadt: Steinkopff, 1989, pp. 128–134.

[30] E. Auzans, D. Zins, E. Blums, and R. Massart, “Synthesis and properties of Mn-Zn ferrite ferrofluids,” p. 8.

[31] H. El Moussaoui *et al.*, “Experimental studies of neodymium ferrites doped with three different transition metals,” *Mater. Lett.*, vol. 171, pp. 142–145, May 2016.

[32] P. H. Linh *et al.*, “Invitro toxicity test and searching the possibility of cancer cell line extermination by magnetic heating with using Fe $_3$ O $_4$ magnetic fluid,” *J. Phys. Conf. Ser.*, vol. 187, p. 012008, Sep. 2009.

[33] S. Lefebure, E. Dubois, V. Cabuil, S. Neveu, and R. Massart, “Monodisperse magnetic nanoparticles: Preparation and dispersion in water and oils,” *J. Mater. Res.*, vol. 13, no. 10, pp. 2975–2981, Oct. 1998.

[34] C. Pereira *et al.*, “Superparamagnetic MFe $_2$ O $_4$ (M = Fe, Co, Mn) Nanoparticles: Tuning the Particle Size and Magnetic Properties through a Novel One-Step Coprecipitation Route,” *Chem. Mater.*, vol. 24, no. 8, pp. 1496–1504, Apr. 2012.

[35] A. Bee, R. Massart, and S. Neveu, “Synthesis of very fine maghemite particles,” *J. Magn. Magn. Mater.*, vol. 149, no. 1–2, pp. 6–9, Aug. 1995.

[36] D. Biswal, B. N. Peeples, C. Peeples, and A. K. Pradhan, “Tuning of magnetic properties in cobalt ferrite by varying Fe +2 and Co +2 molar ratios,” *J. Magn. Magn. Mater.*, vol. 345, pp. 1–6, Nov. 2013.

[37] A. Repko, J. Vejpravová, T. Vacková, D. Zákutná, and D. Nižňanský, “Oleate-based hydrothermal preparation of CoFe2O4 nanoparticles, and their magnetic properties with respect to particle size and surface coating,” *J. Magn. Magn. Mater.*, vol. 390, pp. 142–151, Sep. 2015.

[38] I. Zalite, G. Heidemane, L. Kuznetsova, and M. Maiorov, “Hydrothermal Synthesis of Cobalt Ferrite Nanosized Powders,” *IOP Conf. Ser. Mater. Sci. Eng.*, vol. 77, p. 012011, Mar. 2015.

[39] V. Cabuil, V. Dupuis, D. Talbot, and S. Neveu, “Ionic magnetic fluid based on cobalt ferrite nanoparticles: Influence of hydrothermal treatment on the nanoparticle size,” *J. Magn. Magn. Mater.*, vol. 323, no. 10, pp. 1238–1241, May 2011.

[40] S. Sun and H. Zeng, “Size-Controlled Synthesis of Magnetite Nanoparticles,” *J. Am. Chem. Soc.*, vol. 124, no. 28, pp. 8204–8205, Jul. 2002.

[41] Z. Xu, C. Shen, Y. Hou, H. Gao, and S. Sun, “Oleylamine as Both Reducing Agent and Stabilizer in a Facile Synthesis of Magnetite Nanoparticles,” *Chem. Mater.*, vol. 21, no. 9, pp. 1778–1780, May 2009.

[42] W. Baaziz *et al.*, “Magnetic Iron Oxide Nanoparticles: Reproducible Tuning of the Size and Nanosized-Dependent Composition, Defects, and Spin Canting,” *J. Phys. Chem. C*, vol. 118, no. 7, pp. 3795–3810, Feb. 2014.

[43] L. I. Cabrera, Á. Somoza, J. F. Marco, C. J. Serna, and M. Puerto Morales, “Synthesis and surface modification of uniform MFe2O4 (M = Fe, Mn, and Co) nanoparticles with tunable sizes and functionalities,” *J. Nanoparticle Res.*, vol. 14, no. 6, Jun. 2012.

[44] V. K. LaMer and R. H. Dinegar, “Theory, Production and Mechanism of Formation of Monodispersed Hydrosols,” *J. Am. Chem. Soc.*, vol. 72, no. 11, pp. 4847–4854, Nov. 1950.

[45] G. Muscas *et al.*, “Tuning the Size and Shape of Oxide Nanoparticles by Controlling Oxygen Content in the Reaction Environment: Morphological Analysis by Aspect Maps,” *Chem. Mater.*, vol. 27, no. 6, pp. 1982–1990, Mar. 2015.

[46] S. Sun *et al.*, “Monodisperse MFe $_2$ O $_4$ (M = Fe, Co, Mn) Nanoparticles,” *J. Am. Chem. Soc.*, vol. 126, no. 1, pp. 273–279, Jan. 2004.

[47] L. T. Lu *et al.*, “Synthesis of magnetic cobalt ferrite nanoparticles with controlled morphology, monodispersity and composition: the influence of solvent, surfactant, reductant and synthetic conditions,” *Nanoscale*, vol. 7, no. 46, pp. 19596–19610, 2015.

[48] R. Guinebretière, *Diffraction des rayons X sur échantillons polycristallins: Instrumentation et étude de la microstructure*. Hermes Science Publications, 2006.

[49] F. Rouessac, A. Rouessac, and D. Cruché, *Analyse chimique - 6e éd.: Méthodes et techniques instrumentales modernes*. Dunod, 2004.

[50] L. LaConte, N. Nitin, and G. Bao, “Magnetic nanoparticle probes,” *Mater. Today*, vol. 8, no. 5, pp. 32–38, May 2005.

[51] N. A. Frey, S. Peng, K. Cheng, and S. Sun, “Magnetic nanoparticles: synthesis, functionalization, and applications in bioimaging and magnetic energy storage,” *Chem. Soc. Rev.*, vol. 38, no. 9, p. 2532, 2009.

[52] P. Tartaj, M. a del P. Morales, S. Veintemillas-Verdaguer, T. Gonz lez-Carre o, and C. J. Serna, “The preparation of magnetic nanoparticles for applications in biomedicine,” *J. Phys. Appl. Phys.*, vol. 36, no. 13, pp. R182–R197, Jul. 2003.

[53] B. Srinivasan *et al.*, “A Detection System Based on Giant Magnetoresistive Sensors and High-Moment Magnetic Nanoparticles Demonstrates Zeptomole Sensitivity: Potential for Personalized Medicine,” *Angew. Chem. Int. Ed.*, vol. 48, no. 15, pp. 2764–2767, Mar. 2009.

[54] V. Pillai and D. O. Shah, “Synthesis of high-coercivity cobalt ferrite particles using water-in-oil microemulsions,” *J. Magn. Magn. Mater.*, vol. 163, no. 1–2, pp. 243–248, Oct. 1996.

[55] K. K. Senapati, C. Borgohain, and P. Phukan, “Synthesis of highly stable CoFe2O4 nanoparticles and their use as magnetically separable catalyst for Knoevenagel reaction in aqueous medium,” *J. Mol. Catal. Chem.*, vol. 339, no. 1–2, pp. 24–31, Apr. 2011.

[56] Z.-G. Chen and D.-Y. Tang, “Antigen–antibody interaction from quartz crystal microbalance immunosensors based on magnetic CoFe2O4/SiO2 composite nanoparticle-functionalized biomimetic interface,” *Bioprocess Biosyst. Eng.*, vol. 30, no. 4, pp. 243–249, Jun. 2007.

[57] S. D. Bhame and P. A. Joy, “Enhanced magnetostrictive properties of CoFe2O4 synthesized by an autocombustion method,” *Sens. Actuators Phys.*, vol. 137, no. 2, pp. 256–261, Jul. 2007.

[58] W. Wu, Q. He, and C. Jiang, “Magnetic Iron Oxide Nanoparticles: Synthesis and Surface Functionalization Strategies,” *Nanoscale Res. Lett.*, vol. 3, no. 11, pp. 397–415, Nov. 2008.

[59] T. Hyeon, “Chemical synthesis of magnetic nanoparticles,” *Chem. Commun.*, no. 8, pp. 927–934, Apr. 2003.

[60] B. P. Pichon *et al.*, “Microstructural and Magnetic Investigations of Wüstite-Spinel Core-Shell Cubic-Shaped Nanoparticles,” *Chem. Mater.*, vol. 23, no. 11, pp. 2886–2900, Jun. 2011.

[61] A. Demortière *et al.*, “Size-dependent properties of magnetic iron oxidenanocrystals,” *Nanoscale*, vol. 3, no. 1, pp. 225–232, 2011.

[62] Q. Song and Z. J. Zhang, “Controlled Synthesis and Magnetic Properties of Bimagnetic Spinel Ferrite $CoFe_2O_4$ and $MnFe_2O_4$ Nanocrystals with Core–Shell Architecture,” *J. Am. Chem. Soc.*, vol. 134, no. 24, pp. 10182–10190, Jun. 2012.

[63] S. Sun *et al.*, “Monodisperse $MFe_2O_4$ (M = Fe, Co, Mn) Nanoparticles,” *J. Am. Chem. Soc.*, vol. 126, no. 1, pp. 273–279, Jan. 2004.

[64] A. K. Sekone, Y.-B. Chen, M.-C. Lu, W.-K. Chen, C.-A. Liu, and M.-T. Lee, “Silicon Nanowires for Solar Thermal Energy Harvesting: an Experimental Evaluation on the Trade-off Effects of the Spectral Optical Properties,” *Nanoscale Res. Lett.*, vol. 11, no. 1, p. 1, Dec. 2016.

[65] Z. Wang *et al.*, “High-pressure x-ray diffraction and Raman spectroscopic studies of the tetragonal spinel CoFe 2 O 4,” *Phys. Rev. B*, vol. 68, no. 9, p. 094101, Sep. 2003.

[66] J. Wang, Z. Li, J. Wang, H. He, and C. Nan, “Effect of thickness on the stress and magnetoelectric coupling in bilayered $Pb(Zr_{0.52}Ti_{0.48})O_3$ -$CoFe_2O_4$ films,” *J. Appl. Phys.*, vol. 117, no. 4, p. 044101, Jan. 2015.

[67] S. Hara *et al.*, “One-pot synthesis of monodisperse CoFe2O4@Ag core-shell nanoparticles and their characterization,” *Nanoscale Res. Lett.*, vol. 13, no. 1, p. 176, Dec. 2018.

[68] L. Pérez-Mirabet *et al.*, “One-pot synthesis of stable colloidal solutions of MFe2O4 nanoparticles using oleylamine as solvent and stabilizer,” *Mater. Res. Bull.*, vol. 48, no. 3, pp. 966–972, Mar. 2013.

[69] W. Baaziz *et al.*, “Magnetic Iron Oxide Nanoparticles: Reproducible Tuning of the Size and Nanosized-Dependent Composition, Defects, and Spin Canting,” *J. Phys. Chem. C*, vol. 118, no. 7, pp. 3795–3810, Feb. 2014.

[70] W. Baaziz *et al.*, “Magnetic Iron Oxide Nanoparticles: Reproducible Tuning of the Size and Nanosized-Dependent Composition, Defects, and Spin Canting,” *J. Phys. Chem. C*, vol. 118, no. 7, pp. 3795–3810, Feb. 2014.

[71] C. A. Crouse and A. R. Barron, “Reagent control over the size, uniformity, and composition of Co–Fe–O nanoparticles,” *J. Mater. Chem.*, vol. 18, no. 35, p. 4146, 2008.

[72] C. Moya, M. del P. Morales, X. Batlle, and A. Labarta, “Tuning the magnetic properties of Co-ferrite nanoparticles through the 1,2-hexadecanediol concentration in the reaction mixture,” *Phys. Chem. Chem. Phys.*, vol. 17, no. 19, pp. 13143–13149, 2015.

[73] Z. Zhang, A. J. Rondinone, J. X. Ma, J. Shen, and S. Dai, “Morphologically Templated Growth of Aligned Spinel CoFe2O4 Nanorods,” *Adv. Mater.*, vol. 17, no. 11, pp. 1415–1419, Jun. 2005.

[74] S. Verma and D. Pravarthana, “One-Pot Synthesis of Highly Monodispersed Ferrite Nanocrystals: Surface Characterization and Magnetic Properties,” *Langmuir*, vol. 27, no. 21, pp. 13189–13197, Nov. 2011.

[75] A.-H. Lu, E. L. Salabas, and F. Schüth, “Magnetic Nanoparticles: Synthesis, Protection, Functionalization, and Application,” *Angew. Chem. Int. Ed.*, vol. 46, no. 8, pp. 1222–1244, Feb. 2007.

[76] S. Verma and P. A. Joy, “Magnetic properties of superparamagnetic lithium ferrite nanoparticles,” *J. Appl. Phys.*, vol. 98, no. 12, p. 124312, Dec. 2005.

[77] A. J. Rondinone, A. C. S. Samia, and Z. J. Zhang, “Superparamagnetic Relaxation and Magnetic Anisotropy Energy Distribution in $CoFe_2O_4$ Spinel Ferrite Nanocrystallites,” *J. Phys. Chem. B*, vol. 103, no. 33, pp. 6876–6880, Aug. 1999.

[78] J. M. Byrne *et al.*, “Control of nanoparticle size, reactivity and magnetic properties during the bioproduction of magnetite by *Geobacter sulfurreducens*,” *Nanotechnology*, vol. 22, no. 45, p. 455709, Nov. 2011.

[79] P. H. Nam *et al.*, “Polymer-coated cobalt ferrite nanoparticles: synthesis, characterization, and toxicity for hyperthermia applications,” *New J. Chem.*, vol. 42, no. 17, pp. 14530–14541, Aug. 2018.

[80] J. Park *et al.*, “One-Nanometer-Scale Size-Controlled Synthesis of Monodisperse Magnetic Iron Oxide Nanoparticles,” *Angew. Chem. Int. Ed.*, vol. 44, no. 19, pp. 2872–2877, May 2005.

[81] J. Park *et al.*, “Ultra-large-scale syntheses of monodisperse nanocrystals,” *Nat. Mater.*, vol. 3, no. 12, pp. 891–895, Dec. 2004.

[82] Q. Song and Z. J. Zhang, “Correlation between Spin−Orbital Coupling and the Superparamagnetic Properties in Magnetite and Cobalt Ferrite Spinel Nanocrystals,” *J. Phys. Chem. B*, vol. 110, no. 23, pp. 11205–11209, Jun. 2006.

[83] A. K. Gupta and M. Gupta, “Synthesis and surface engineering of iron oxide nanoparticles for biomedical applications,” *Biomaterials*, vol. 26, no. 18, pp. 3995–4021, Jun. 2005.

[84] T. Hyeon, S. S. Lee, J. Park, Y. Chung, and H. B. Na, “Synthesis of Highly Crystalline and Monodisperse Maghemite Nanocrystallites without a Size-Selection Process,” *J. Am. Chem. Soc.*, vol. 123, no. 51, pp. 12798–12801, Dec. 2001.

[85] S. G. Kwon *et al.*, “Kinetics of Monodisperse Iron Oxide Nanocrystal Formation by ‘Heating-Up’ Process,” *J. Am. Chem. Soc.*, vol. 129, no. 41, pp. 12571–12584, Oct. 2007.

[86] H. Zeng, C. T. Black, R. L. Sandstrom, P. M. Rice, C. B. Murray, and S. Sun, "Magnetotransport of magnetite nanoparticle arrays," *Phys. Rev. B*, vol. 73, no. 2, p. 020402, Jan. 2006.

[87] V. K. LaMer and R. H. Dinegar, "Theory, Production and Mechanism of Formation of Monodispersed Hydrosols," *J. Am. Chem. Soc.*, vol. 72, no. 11, pp. 4847–4854, Nov. 1950.

[88] L. M. Bronstein *et al.*, "Nanoparticles by Decomposition of Long Chain Iron Carboxylates: From Spheres to Stars and Cubes," *Langmuir*, vol. 27, no. 6, pp. 3044–3050, Mar. 2011.

[89] J. P. O'Sullivan and G. C. Wood, "The Morphology and Mechanism of Formation of Porous Anodic Films on Aluminium," *Proc. R. Soc. Math. Phys. Eng. Sci.*, vol. 317, no. 1531, pp. 511–543, Jul. 1970.

[90] V. P. Parkhutik and V. I. Shershulsky, "Theoretical modelling of porous oxide growth on aluminium," *J. Phys. Appl. Phys.*, vol. 25, no. 8, pp. 1258–1263, Aug. 1992.

[91] O. Jessensky, F. Müller, and U. Gösele, "Self-organized formation of hexagonal pore arrays in anodic alumina," *Appl. Phys. Lett.*, vol. 72, no. 10, pp. 1173–1175, Mar. 1998.

[92] H. Masuda and K. Fukuda, "Ordered Metal Nanohole Arrays Made by a Two-Step Replication of Honeycomb Structures of Anodic Alumina," *Science*, vol. 268, no. 5216, pp. 1466–1468, Jun. 1995.

[93] M. Macé, "Membranes d'alumine nano-poreuses pour l'élaboration de nanostructures," thesis, Aix-Marseille 2, 2010.

[94] J. L. Murray, "The Au-Ti (Gold-Titanium) system," *Bull. Alloy Phase Diagr.*, vol. 4, no. 3, pp. 278–283, Nov. 1983.

[95] U. R. Kattner, J.-C. Lin, and Y. A. Chang, "Thermodynamic Assessment and Calculation of the Ti-Al System," *Metall. Trans. A*, vol. 23, no. 8, pp. 2081–2090, Aug. 1992.

[96] G. E. Thompson, "Porous anodic alumina: fabrication, characterization and applications," *Thin Solid Films*, vol. 297, no. 1–2, pp. 192–201, Apr. 1997.

[97] F. Li, L. Zhang, and R. M. Metzger, "On the Growth of Highly Ordered Pores in Anodized Aluminum Oxide," *Chem. Mater.*, vol. 10, no. 9, pp. 2470–2480, Sep. 1998.

[98] M. Es-Souni and S. Habouti, "Ordered Nanomaterial Thin Films via Supported Anodized Alumina Templates," *Front. Mater.*, vol. 1, Oct. 2014.

[99] A. P. Li, F. Müller, A. Birner, K. Nielsch, and U. Gösele, "Hexagonal pore arrays with a 50–420 nm interpore distance formed by self-organization in anodic alumina," *J. Appl. Phys.*, vol. 84, no. 11, pp. 6023–6026, Dec. 1998.

[100] "Gualino-Tamonino, Marion. Structuration et mise en forme de matériaux moléculaires poreux au sein de membranes d'alumine - thesesups." [Online]. Available: http://thesesups.ups-tlse.fr/2990/. [Accessed: 15-Aug-2019].

[101] A. Johansson, E. Widenkvist, J. Lu, M. Boman, and U. Jansson, “Fabrication of High-Aspect-Ratio Prussian Blue Nanotubes Using a Porous Alumina Template,” *Nano Lett.*, vol. 5, no. 8, pp. 1603–1606, Aug. 2005.

[102] W. Zhu, W. Wang, H. Xu, and J. Shi, “Fabrication of ordered SnO2 nanotube arrays via a template route,” *Mater. Chem. Phys.*, vol. 99, no. 1, pp. 127–130, Sep. 2006.

[103] “TEL - Thèses en ligne - Structuration et mise en forme de matériaux moléculaires poreux au sein de membranes d’alumine.” [Online]. Available: https://tel.archives-ouvertes.fr/tel-01407251. [Accessed: 15-Aug-2019].

[104] A.-H. Lu *et al.*, “Fabrication of Magnetically Separable Mesostructured Silica with an Open Pore System,” *J. Am. Chem. Soc.*, vol. 126, no. 28, pp. 8616–8617, Jul. 2004.

[105] J. Jang, H. Nah, J.-H. Lee, S. H. Moon, M. G. Kim, and J. Cheon, “Critical Enhancements of MRI Contrast and Hyperthermic Effects by Dopant-Controlled Magnetic Nanoparticles,” *Angew. Chem. Int. Ed.*, vol. 48, no. 7, pp. 1234–1238, Feb. 2009.

[106] P. Sivakumar, R. Ramesh, A. Ramanand, S. Ponnusamy, and C. Muthamizhchelvan, “Synthesis and characterization of NiFe2O4 nanosheet via polymer assisted co-precipitation method,” *Mater. Lett.*, vol. 65, no. 3, pp. 483–485, Feb. 2011.

[107] Z. Zhang, A. J. Rondinone, J. X. Ma, J. Shen, and S. Dai, “Morphologically Templated Growth of Aligned Spinel CoFe2O4 Nanorods,” *Adv. Mater.*, vol. 17, no. 11, pp. 1415–1419, Jun. 2005.

[108] A. Bharde *et al.*, “Extracellular Biosynthesis of Magnetite using Fungi,” *Small*, vol. 2, no. 1, pp. 135–141, Jan. 2006.

[109] A. P. Philipse and D. Maas, “Magnetic Colloids from Magnetotactic Bacteria: Chain Formation and Colloidal Stability,” *Langmuir*, vol. 18, no. 25, pp. 9977–9984, Dec. 2002.

[110] V. S. Coker *et al.*, “Microbial Engineering of Nanoheterostructures: Biological Synthesis of a Magnetically Recoverable Palladium Nanocatalyst,” *ACS Nano*, vol. 4, no. 5, pp. 2577–2584, May 2010.

[111] V. S. Coker *et al.*, “Harnessing the Extracellular Bacterial Production of Nanoscale Cobalt Ferrite with Exploitable Magnetic Properties,” *ACS Nano*, vol. 3, no. 7, pp. 1922–1928, Jul. 2009.

[112] M. Goodarz and E. B., “Crystalization in Spinel Ferrite Nanoparticles,” in *Advances in Crystallization Processes*, Y. Mastai, Ed. InTech, 2012.

[113] M. Goodarz Naseri, E. B. Saion, and A. Kamali, “An Overview on Nanocrystalline ZnFe $_2$ O $_4$ , MnFe $_2$ O $_4$ , and CoFe $_2$ O $_4$ Synthesized by a Thermal Treatment Method,” *ISRN Nanotechnol.*, vol. 2012, pp. 1–11, 2012.

[114] Y.-G. Li, H.-S. Gao, W.-L. Li, J.-M. Xing, and H.-Z. Liu, “In situ magnetic separation and immobilization of dibenzothiophene-desulfurizing bacteria,” *Bioresour. Technol.*, vol. 100, no. 21, pp. 5092–5096, Nov. 2009.

[115] M. G. Naseri, E. B. Saion, H. A. Ahangar, M. Hashim, and A. H. Shaari, “Simple preparation and characterization of nickel ferrite nanocrystals by a thermal treatment method,” *Powder Technol.*, vol. 212, no. 1, pp. 80–88, Sep. 2011.

[116] Y. Li, M. Afzaal, and P. O’Brien, “The synthesis of amine-capped magnetic (Fe, Mn, Co, Ni) oxide nanocrystals and their surface modification for aqueous dispersibility,” *J. Mater. Chem.*, vol. 16, no. 22, p. 2175, 2006.

[117] Q. Song and Z. J. Zhang, “Shape Control and Associated Magnetic Properties of Spinel Cobalt Ferrite Nanocrystals,” *J. Am. Chem. Soc.*, vol. 126, no. 19, pp. 6164–6168, May 2004.

[118] N. Bao, L. Shen, Y. Wang, P. Padhan, and A. Gupta, “A Facile Thermolysis Route to Monodisperse Ferrite Nanocrystals,” *J. Am. Chem. Soc.*, vol. 129, no. 41, pp. 12374–12375, Oct. 2007.

[119] S. Sun *et al.*, “Monodisperse $MFe_2O_4$ (M = Fe, Co, Mn) Nanoparticles,” *J. Am. Chem. Soc.*, vol. 126, no. 1, pp. 273–279, Jan. 2004.

[120] J. Wan, X. Jiang, H. Li, and K. Chen, “Facile synthesis of zinc ferrite nanoparticles as non-lanthanide T1 MRI contrast agents,” *J. Mater. Chem.*, vol. 22, no. 27, p. 13500, 2012.

[121] Q. Song and Z. J. Zhang, “Shape Control and Associated Magnetic Properties of Spinel Cobalt Ferrite Nanocrystals,” *J. Am. Chem. Soc.*, vol. 126, no. 19, pp. 6164–6168, May 2004.

[122] N. A. Frey and S. Sun, “Magnetic nanoparticle for information storage applications,” *Inorg. Nanoparticles Synth. Appl. Perspect. CRC Press Boca Raton USA*, pp. 33–67, 2010.

[123] S. D. Bhame and P. A. Joy, “Enhanced magnetostrictive properties of CoFe2O4 synthesized by an autocombustion method,” *Sens. Actuators Phys.*, vol. 137, no. 2, pp. 256–261, Jul. 2007.

[124] S. Sun *et al.*, “Monodisperse $MFe_2O_4$ (M = Fe, Co, Mn) Nanoparticles,” *J. Am. Chem. Soc.*, vol. 126, no. 1, pp. 273–279, Jan. 2004.

[125] L. T. Lu *et al.*, “Synthesis of magnetic cobalt ferrite nanoparticles with controlled morphology, monodispersity and composition: the influence of solvent, surfactant, reductant and synthetic conditions,” *Nanoscale*, vol. 7, no. 46, pp. 19596–19610, 2015.

# Résumé en Français

Dans le présent travail, les nanoparticules monodisperses à base de ferrite de cobalt ont été explorées pour leurs propriétés magnétiques et leur effet magnétostrictif, ainsi que pour une utilisation en tant que ferrofluide. Les nanoparticules ont été dispersées avec succès dans un solvant organique. La chimie de surface de la nanoparticule magnétique s'avère cruciale pour obtenir une dispersion haute densité homogène et bien séparée dans l'hexane. De plus, l'acide oléique a été utilisé pour modifier la surface des nanoparticules de ferrite de cobalt et permettre d'obtenir une bonne dispersion.

Les nanoparticules obtenues sont caractérisées par XRD, spectroscopie Raman, TGA, FT-IR, DLS, SEM et la caractérisation magnétique. En utilisant l'analyse STEM, nous avons constaté que la taille et la forme des nanoparticules pouvaient être contrôlées en faisant varier certains paramètres tels que la température de synthèse, la quantité et la nature des réactifs.

En outre, des membranes anodiques poreuses à pores très ordonnés ont été fabriquées avec succès avec une anodisation en plusieurs étapes. Des nanorods de ferrite de cobalt ont été produites par la transformation des nanoparticules de $CoFe_2O_4$ à l'aide d'une membrane d'alumine poreuses. L'insertion des nanoparticules de $CoF_2O_4$ dans les pores des membranes a été étudiée par le microscope électronique à balayage, et il a été possible de suivre le comportement des nanoparticules de $CoFe_2O_4$ dans les pores lors de l'insertion ainsi que lors de la transformation.

**Mot-clés** : Ferrite de cobalt, nanoparticules monodisperseés, décomposition thermique, membranes d'alumine, nanorods, propriétés magnétiques.

# Résumé en Anglais (Abstract)

In the present work, monodisperse cobalt ferrite nanoparticle systems have been explored in regard to their magnetic properties and magnetostrictive effect, as well as for use as a ferrofluid. Nanoparticles have been successfully dispersed in an organic solvent. The surface chemistry of the magnetic nanoparticle proves critical to obtaining a homogeneous and well separated high density dispersion in Hexane. In addition, Oleic acid was used to alter the surface of cobalt ferrite nanoparticles and successfully achieve good dispersion.

The obtained nanoparticles are characterized using XRD, Raman spectroscopy, TGA, FT-IR, DLS, SEM, and magnetic investigations. Using STEM analysis, we found that the size and shape of nanoparticles could be controlled by varying certain parameters such as the synthesis temperature, the quantity, and nature of reagents. Furthermore, porous anodic membranes with highly ordered pores were successfully fabricated with multi-steps anodizing. Cobalt ferrite nanorods were produced by a transformation of $CoFe_2O_4$ nanoparticles using anodic alumina membrane. The insertion of $CoF_2O_4$ nanoparticles into the pores of the AAO membranes was studied with a scanning electron microscope, and it was possible to follow the behavior of $CoFe_2O_4$ nanoparticles in the pores during the insertion step as well as the transformation step.

**Keywords** : Cobalt ferrite, Monodispersed Nanoparticles, thermal decomposition, alumina membranes, nanorods.